EFFECT OF ALLOYING ELEMENTS AND HEATING RATES ON FERITTE RECRYSTALLIZATION IN DUAL PHASE STEEL

MASTER THESIS

VITESH SHAH
MSc Materials Science and Engineering

AUGUST 28, 2017
DEPARTMENT OF MATERIALS SCIENCE AND ENGINEERING
Faculty of Mechanical, Maritime and Materials Engineering
DELFT UNIVERSITY OF TECHNOLOGY

Supervisors:
Assoc. Prof. Dr. S. Erik Offerman (TU Delft)
Monika Krugla (TATA Steel, TU Delft)

Committee Members:
Assoc. Prof. Dr. S. Erik Offerman (TU Delft)
Monika Krugla (TATA Steel, TU Delft)
Prof. Dr. Jilt Sietsma (TU Delft)
Asst. Prof. Dr. Vera Popovich (TU Delft)

ACKNOWLEDGEMENTS

Firstly, I would like to thank my supervisors – Erik Offerman and Monika Krugla, for giving me opportunity to work with annealing of steels and related processes such as recrystallization, recovery and phase transformations. The project allowed me to investigate many basic processes, that are common in metallurgy, and therefore, this master thesis project helped me shape into a competent materials scientist with a specialization in steels.

The regular meetings with Erik and Monika, have really helped in development of many of the ideas and concepts in this thesis. I think without their contribution it would have been very difficult to give specific direction to this research. The critical attitude of Erik has turned me into a person, who reviews the experimental data and scientific findings critically. The long discussions with Erik and Monika about the various analytical models for recrystallization and the mechanisms of recrystallization have really provided me with clear understanding of this complex process. Writing the meeting summaries helped me come up with new ideas, directions and also helped me with the writing of this manuscript.

Special thanks to Monika, for helping me with planning of the experiments and data processing techniques. Her explanations with regards to SEM imaging really helped me improve my understanding and taking better microstructure images. Her critical attitude towards my every result, helped me enhance my results and also improved my approach towards experimentation. She also helped me with the planning, and carrying out of in-situ XRD experiments as well. Moreover, she also helped me with the grain size analysis software. I think without her help, a major part of this thesis would have had been impossible.

I would also like to thank Stefan Melzer, who guided me with High Temperature XRD experiments. He trained me in using XRD and also showed me the procedure to do further data processing of XRD data and getting data for recrystallization from XRD results. Without his help, the XRD part of this work would have been difficult. Because of his contribution, I have got interested in use of XRD in various investigations.

Next, I would like to thank Kees Kwakernak, for helping me and training me for using the SEM at the university. His inputs for getting better microstructure images was invaluable. Moreover, I would also like to thank Sander van Asperen, for providing me with the facilities and tips for sample preparation, which was quite a difficult task.

I should also thank Netherlands, which I think is one of the most welcoming countries with wonderful people. I have made some really great friends during my stay here and I think they really made my stay enjoyable and also made me into a better person.

Finally, I would like to thank my parents, Naren and Bhavana, who have always supported me and believed in me. They have stood by me as a steady rock giving me support even in the times when things have not gone well.

ABSTRACT

The Dual Phase Steels (DP Steels) have attracted interest of steel manufacturers, especially automotive industry, because of a good combination of high strength and ductility. The final DP steel microstructures are formed during continuous heating to intercritical temperatures, then isothermal holding and quenching to form a mix of ferrite and martensite. Final martensite content, morphology and spatial distribution depends on the austenite formed during the isothermal holding. The austenite formation is affected by the progress of ferrite recrystallization during continuous heating. Therefore, it is important to understand the process of ferrite recrystallization.

This thesis aims to study the effect of Si and Mn, which are common alloying elements in steels, on the ferrite recrystallization. The present study extensively uses in-situ 2D X-ray Diffraction (XRD) to investigate the ferrite recrystallization kinetics. This technique is faster and records more data than the other conventional methods used to study the kinetics of recrystallization until now. This study introduces a method to quantify the recrystallized grains using Scanning Electron Microscope (SEM) and Backscattered Electron Detector (BED). This method results in faster analysis of microstructure. The microstructure analysis helped in quantifying the grain growth, its dimensions and type of nucleation. Afterwards, those have been used as input parameters for modified non-isothermal JMAK model. This model is used to obtain the kinetic parameters from the experimental in-situ 2D XRD results by model fitting. The parameters obtained are: rate constant, activation energy and Avrami exponent. In all the cases, the microstructure analysis show site-saturated nucleation and predominantly 2D grain growth. The model fitting reveals that most nucleation cases show site-saturation. The density of nucleation sites is dependent on the pearlite content of the alloys. The boundaries between deformed pearlite and ferrite being the preferred nucleation sites. In some cases, the recrystallization nuclei are also seen at the boundaries between the ferrite grains which correspond to areas with micro-segregation of Mn.

Presence of Mn is leading to an increase recrystallization start temperatures. The solute drag effect of Mn is quite high. Similarly, Si is also retarding the recrystallization. The retardation effect of Si is not as significant as Mn. The solute drag effect seems to be dependent on the velocity of the grain boundaries and consequently, on progress of recrystallization. In presence of Mn, the Si is able to interact with the moving grain boundaries. This points to co-segregation effect between Mn and Si. This effect was found to be strongest for 1:1 Si to Mn atomic fractions, where the lowest growth rates were observed.

KEYWORDS: DP steels, ferrite recrystallization, solute drag effect, in-situ 2D XRD, recrystallization kinetics, SEM, JMAK model, activation energy, co-segregation.

CONTENTS

LIST OF ABBREVIATIONS

DP Steels:	Dual Phase Steels
XRD:	X-ray Diffraction
SEM:	Scanning Electron Microscope
BED:	Backscattered Electron Detector
JMAK:	Johnson-Mehl-Avrami-Kolmogrov Model
BIW:	Body in White
TRIP:	Transformation Induced Plasticity
RX_Start:	Recrystallization Start Temperature
RX_finish:	Recrystallization Finish Temperature
RX:	Recrystallization
HAGBs:	High Angle Grain Boundaries
LOM:	Light Optical Microscopy
EBSD:	Electron Backscatter Diffraction
HT-SEM:	High Temperature Scanning Electron Microscope
HT-EBSD:	High Temperature Electron Backscatter Diffraction
HT-XRD:	High Temperature X-Ray Diffraction
TEM:	Transmission Electron Microscope
PSD:	Position Sensitive Detector
ND:	Normal Direction
RD:	Rolling Direction
TD:	Transverse Direction
RX_vol_frac:	Recrystallization volume fraction
BSE:	Backscattered Electrons
EDS:	Energy Dispersive X-ray Spectroscopy

1. INTRODUCTION

1.1 IMPORTANCE AND DEVELOPMENT OF STEELS

Being one of the most commonly used materials in the world, steel is found in nearly every conceivable application. It is also commonly used in automotive industry. Even though many other materials have emerged since to compete with steel, it is still the most widely used material in cars. The most material intensive part in an automobile is Body In White (BIW), i.e. the outer body of the car [1]. In the first half of the last century, the type of steels used in automotive industry didn't undergo any major changes. The oil crisis in 1975 as well as the increase in environmental awareness, changed the outlook of the automotive industry. This led to an increase in demand for fuel-efficient cars [2]. One of the ways to achieve a higher fuel-efficiency is to build lighter cars. Stronger steels that allow for thinner outer panels help in weight reduction of the cars. Along with high strength, ductility is also an important property. Higher ductility leads to better formability, making complex outer designs possible. Thus, development of steels with even higher strengths and ductility began.

The major requirements for sheets to be used in automotive industry are – costs, formability, surface quality, environmental impact, strength, stiffness, ductility, dimensional accuracy. To get good combination of strength and ductility, steels with multiple phases – such as Dual Phase (DP steels), Transformation Induced Plasticity (TRIP Steels) were developed [2].

1.2 RELEVANCE OF RECRYSTALLIZATION IN MULTI-PHASE STEELS

During the production process of these multi-phase steels, heating to intercritical temperatures, soaking in intercritical temperature range and different types of cooling cycles are employed to get the multi-phase microstructures. During heating, recrystallization is a major microstructural change that can occur in a cold-rolled material [3]. Ferrite recrystallization is important in development of dual phase steels, because it can affect the formation, distribution and amount of austenite [4,5]. This affects the final microstructure and mechanical properties to a great extent. Therefore, more understanding about the recrystallization process with an aim of controlling it to get desired microstructures is important. Most of the ferrite recrystallization studies are done with temperatures and heating rates, where the austenite formation takes place in conjunction with recrystallization [3–5]. These conditions fail to give a clear picture about the recrystallization itself. Also, the ferrite recrystallization is affected by the process parameters as well [6]. A more detailed insight on effect of processing parameters on ferrite recrystallization can be useful in microstructure control. Even though the basics of the process are widely known, the detailed information about the role of alloying elements in this process is missing. Also, a correlation between the amount of alloying elements and parameters of recrystallization such as – activation energy, number of nucleation sites, effects on growth rate are not known. The recrystallization temperatures are not accurately known for different heating rates. These temperatures can be important for designing a heat treatment cycle for cold-rolled materials. The qualitative description of the effect of alloying elements on ferrite recrystallization needs quantitative characterization for developing better models to predict recrystallization. Grain growth is an important influencing factor in recrystallization. Therefore, better understanding of influence of alloying elements on recrystallization can also shed light on the role of alloying elements during ferrite grain growth.

1.3 OBJECTIVE AND SCOPE OF THESIS

The effect of alloying elements on the kinetics of ferrite recrystallization requires detailed investigation. Thus, the research question being answered in present thesis is – what is the effect of alloying elements (Si and Mn) on ferrite recrystallization together with different heating rates?

To answer this question, following techniques and analyses methods have been used –

- In-situ 2D XRD to investigate the kinetics of ferrite recrystallization experimentally,
- Fitting experimental data to a modified JMAK model to calculate the kinetic parameters,
- Microstructure characterization techniques are used for determining nucleation sites, number of nuclei per unit area, recrystallized grain shapes, recrystallized grain growth, phase distribution.
- Correlating the data from microstructure characterization with the kinetic parameters

2. BACKGROUND

2.1 PRODUCTION PROCESS OF SHEET STEELS

Most of the high strength steels with an aim of light weighting in automobiles are in the form of thin sheets. The sheet steels are produced from the billets or slabs produced by continuous casting. These slabs/ billets are then hot rolled to reduce their thickness [7]. During this step, the billet is large in size and thus, hot deformation is imperative. But, hot deformation causes oxidation on the surface. These oxides are removed by pickling. The oxide layer is not uniform and therefore, the surface finish is not very good. When better surface finish and thinner sheets are required, cold rolling is employed. Cold rolling is preferred for further reduction because it doesn't involve oxide formation. Moreover, cold rolling leads to very thin sheets with very high strength, due to large amount of dislocations introduced due to cold deformation. Cold rolling is one of the final steps in sheet manufacturing because it can lead to sheets with very high surface finish and strength [7]. Once the sheets are produced, the sheets might be heat treated to produce the desired microstructure.

To produce the multiphase steels, annealing in intercritical temperature range (A1-A3 temperatures) is an important process. This process generates a microstructure of ferrite (α) and austenite (γ). The amount of each phase depends on the combination of soaking time, temperature and heating rate [3]. After this, the steels are quenched completely or in stages to get the desired microstructures. Such an annealing cycle converts the austenite into pearlite, bainite or martensite depending on the type of cooling cycle employed. Dual phase steels consist of hard martensite phase embedded in a soft, ductile ferrite matrix [8]. To get the martensite structure, the steel is quenched completely after the intercritical annealing stage. This converts austenite to martensite [9]. The annealing process of DP Steels is shown in Figure 1.

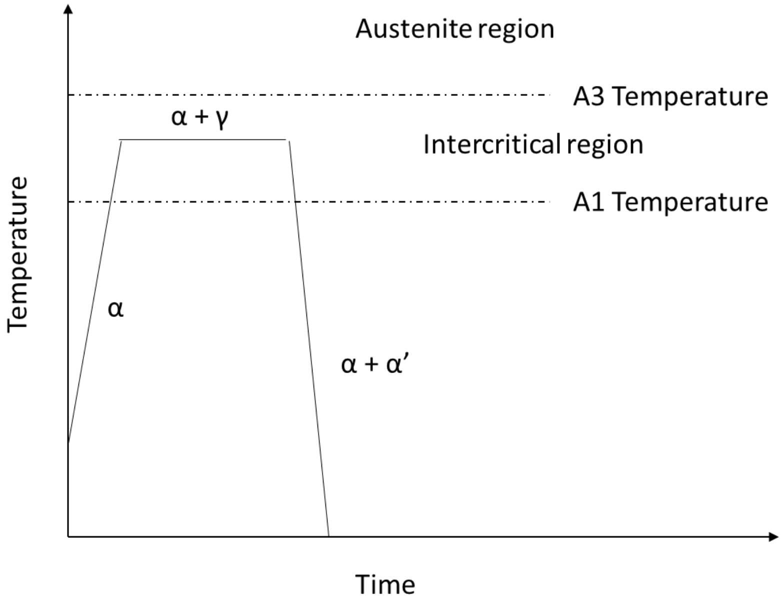

Figure 1 The annealing cycle for producing dual phase steels

2.2 RELATION OF FERRITE RECRYSTALLIZATION WITH MICROSTRUCTURE DEVELOPMENT

The relevance of investigating the ferrite recrystallization lies in the fact that it affects the further microstructure development. The major influence of ferrite recrystallization is on the austenite formation. The austenite formation is a critical step in the production of multi-phase steels because it is a pre-cursor to formation of martensite, bainite or pearlite. The amount and distribution of these phases determines the strength and ductility of the steel produced. This is dependent on the austenite formation kinetics and thus, controlling the factors that influence austenite formation is so important [4]. Ogawa [10] reported that ferrite recrystallization affects the nucleation of austenite during intercritical annealing. It was observed that, when the ferrite recrystallization and austenite formation overlap, then the kinetics of austenite formation are affected quite a lot. It was seen in the work of Chbihi [3], that such an overlap between ferrite recrystallization and austenite formation increases with the heating rate and with the addition of austenite stabilizing elements. Nowadays, due to the desire for faster production lines, the heating rates are increasing. In such a scenario, the possibility of overlap of ferrite recrystallization and austenite formation becomes quite significant. When these two processes overlap, the nucleation sites of austenite can be quite different from the case with no overlap. Liu et al. [11] compared the two cases. In the first case, the steel was recrystallized before austenite formation (slow heating rate). This led to austenite nucleating first at the spheroidised pearlite and later at the recrystallized ferrite grain boundaries. But in the case of overlap (partly recrystallized steel), the austenite nucleated first at the spheroidised pearlite and later only at the boundaries between deformed pearlite and ferrite. The austenite didn’t nucleate at the recrystallizing ferrite boundaries, because they were migrating. Even though there have been studies, which tend to give empirical ideas about ferrite recrystallization, the knowledge is not enough for better microstructure control. For better microstructure control, better quantification of the kinetics of the process is required. Thus, it can be seen that control of ferrite recrystallization is important to control austenite nucleation which will affect further microstructure development.

2.3 MECHANISMS OF RECRYSTALLIZATION

Cold working (or rolling) introduces dislocations, which store the energy of deformation in the material. This is a meta-stable state and the material would always tend to go to a lower energy state. The way to decrease the stored energy for a material is to reduce the number of dislocations in the system. This is possible, when the dislocations interact with each other. Such an interaction occurs during annealing, because the higher temperature allows the dislocations to move and interact with each other. So, the dislocations might interact with each other to annihilate themselves or they might rearrange into stable configurations. These processes can be termed as recovery. Recovery can be described in detail by the following processes: (i) reaction of point defects leading to their decrease (ii) dislocation annihilation (iii) rearrangement of dislocations into lower energy configurations (eg. Sub-grain boundaries) (iv) Formation of high angle boundaries [12]. The growth of these high angle boundaries to absorb all the defects and dislocations is termed as recrystallization [12]. As the processes of sub-grain boundary and high angled grain boundary migration are diffusion dependent, they occur at higher temperatures. Thus, recovery and recrystallization become important microstructural changes during annealing of cold rolled materials.

To understand a particular process, understanding the start of the process is important. In case of phase transformations and recrystallization, this start of the process is termed as nucleation. The nucleation is important in recrystallization because it determines the recrystallized grain sizes and also the orientations of the recrystallizing grains [13].

The nucleation in recrystallization is quite different than the nucleation described by the classical nucleation theory [14]. The classical theory for nucleation doesn't work for recrystallization because of low driving force when compared to driving forces for phase transformations [14]. Moreover, the interface energy between the recrystallized and the non-recrystallized regions is quite high [14]. These two conditions together mean that the critical radius of the nuclei according to the classical nucleation theory would be very large [14]. This is certainly not observed and therefore, recrystallization nucleation is described in a different way.

It is now widely accepted that the recrystallization nuclei are not nuclei according to classical nucleation theory, but are small volumes which already exist in the deformed microstructure [14]. The mechanisms of dislocation rearrangements to form a low dislocation density region which is surrounded by high angle grain boundary are together defined as recrystallization nucleation [12].

There are two widely known and accepted recrystallization models described in the following –

2.3.1 MIGRATION OF PRE-EXISTING HIGH ANGLE GRAIN BOUNDARY

This model assumes that there is already some small region in the microstructure, which is having a lower dislocation density than surrounding region and moreover, it is also surrounded by high angle grain boundary. Therefore, the high angle grain boundary starts migrating, signifying the onset of recrystallization. The mechanism is shown in Figure 2.

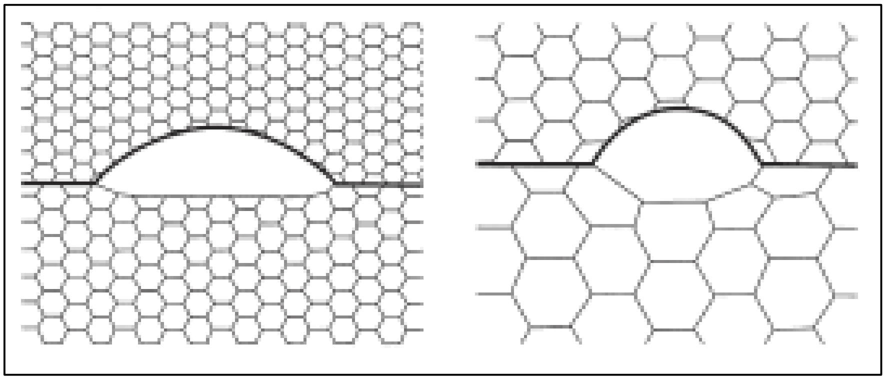

Figure 2 Showing the migration of pre-existing high angle grain boundary [14]

2.3.2 THE PRE-FORMED NUCLEUS MODEL

In some cases, the high angle grain boundaries shown in Figure 2 do not exist. In such cases, the high angle grain boundary is formed as a consequence of sub-grain boundary migration. Humphreys et al. [14] say that it has been established beyond doubt that in such cases the recrystallization originates from dislocation cells or sub-grains present after deformation. Moreover, the orientation of the nucleus is already present in the deformed structure [14]. In such a scenario, the nucleation occurs by the growth of sub-grains. As the sub-grains boundaries grow and absorb the dislocations, they eventually get converted to high angle boundary. Thus, a region with lower dislocation density surrounded by high angle grain boundary is formed. This formation of high angle grain boundary is possible only when the orientation gradient among the sub-grains is very large [14]. The regions with such high orientation gradient will also have higher stored energy, thus more driving force for recrystallization. This mechanism can be seen in Figure 3.

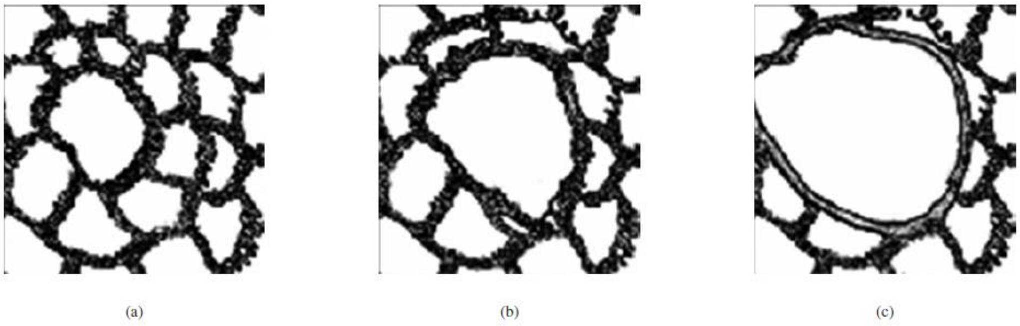

Figure 3 Nucleation of recrystallized grain from a sub-grain a) initial sub-grain structure b) sub-grain growth c) area free of defects surrounded by high angle grain boundary [12].

As can be seen from the two mechanisms described above, there is no new nucleus being formed through random fluctuations of atoms. Also, the embryos or nuclei would not 're-dissolve' if they are not capable of growing. They will just remain in the matrix. This means that the probability of nucleus 're-dissolving' into the matrix is zero. Moreover, there cannot be any activation energy for nucleation if there is already a region surrounded by high angle grain boundaries. In the case, where there is no region surrounded by high angle grain boundary (pre-formed nucleus model), then the activation energy for the sub-grain growth could be considered as the activation energy. But, even this activation energy is equivalent to activation energy for the grain growth. Even in such a scenario, there wouldn't be any term that would account for probability of re-dissolving of embryos. So, depending on the type of nucleation existing, the activation energy for nucleation would be zero or would be equal to activation energy of sub-grain growth.

In case of cold-deformed materials, there is a higher amount of high angle grain boundaries with very small sub-grain sizes [14]. This presents higher probability for having a very small region surrounded completely by high angle grain boundaries. Moreover, the continuous cooling would not give enough time for sufficient recovery and growth of the sub-grains to have nucleation described in Section 2.3.1. In such cases, the migration of pre-existing grain boundaries seems to be the most effective nucleation mechanism. The nucleation sites are generally the regions where there is highest amount of dislocations, orientation gradients and stored energy [14]. In case of low carbon steels, these sites are the boundaries between deformed pearlite and deformed ferrite [15], [16]. These phase boundaries are preferred nucleation sites because the phase (grain) boundaries lead to different combinations of slip systems leading to higher local misorientations [14]. In presence of pearlite, due to the differences in strength of pearlite and ferrite, the misorientations at ferrite-pearlite boundaries are higher, which makes these boundaries as preferable sites for nucleation.

The RX_{start} temperatures are related to the event of nucleation. Therefore, the changes in RX_{start} temperature might point to the changes in the nucleation parameters with alloying. The nucleation parameters that can affect the RX_{start} are the density of the nucleation sites and mobility of the high angle grain boundaries. If their mobility is low, then the HAGBs will start to migrate at higher temperatures and thus, delay the start of recrystallization. If the density of nucleation sites is high, then more number of nuclei would be present in shorter amount of time.

After this ‘nucleation’ stage, the recrystallized nuclei grow. This movement of high-angle grain boundaries during recrystallization is different from what occurs during grain growth [12]. This is mainly due to the difference in the driving force for the grain boundary migration. In addition to the curvature effects, the stored energy of deformation acts as the main driving force. As seen earlier, the nucleation event has no activation energy, because the nucleus pre-exists in case of recrystallization. Therefore, the activation energy for recrystallization depends on the grain boundary migration. The activation energy for high-angle grain boundary migration is considered to be equal to the activation energy of Fe self-diffusion [6], [14]. Therefore, the activation energy of recrystallization can be equated to the activation energy of self-diffusion.

The grain growth also gets affected by the solute drag due to the solute atoms in the materials. In case of solute drag, the solute accumulation at the grain boundaries changes the energy of the grain boundary [17] and also reduces the driving force for migration [14], [18]. This effect is seen in the form of reduction of the grain boundary migration rate. As shown in Appendix C, the effect of reduction in driving force can also be interpreted as a change in the activation energy for grain boundary migration. Therefore, in case of solute drag, the activation energy seems to increase with the alloying content, as shown in Appendix C. Therefore, if the activation energy of recrystallization appears to be greater than the activation energy of self-diffusion, then this increase can point to the solute drag effect.

2.4 THEORETICAL MODELS

2.4.1 RECRYSTALLIZATION KINETICS FROM XRD DATA

The thesis aims to investigate the effect of alloying elements on ferrite recrystallization. For a more accurate description of recrystallization, the information about kinetics of the process is required. The knowledge about temperatures and times where the recrystallization starts and finishes is inadequate to provide a clear picture. To have more information describing the kinetics of recrystallization, a kinetic model can be fitted to the experimental data. The parameters derived from such model fitting can be later used to predict the ferrite recrystallization in these alloys.

JMAK MODEL AND ITS MODIFICATION

Recrystallization is a thermally activated process. One of the most widely used models to describe various thermally activated processes is Johnson-Mehl-Avrami-Kolmogrov model (JMAK) [19–23]. This model is described by a simple equation:

$$\alpha = 1 - \exp[(-kt)^{m+1}] \tag{1}$$

where: α is the overall transformed phase fraction, k is the overall rate constant that incorporates the nucleation and growth constants which ultimately depend on temperature, $m+1$ is the Avrami exponent and t is the time. The equation (1) describes the kinetics for isothermal cases.

The JMAK model is very simplistic. The most basic form assumes constant nucleation and growth rates. The cases of site-saturation and decreasing nucleation rates have been dealt with theoretically leading to the different values of Avrami exponent as seen in Table 1 [19]. Moreover, the nucleation sites are assumed as random in this model. The model also assumes the growth to be isotropic which is again a very idealized case. Due to these assumptions, many times, the experimental data deviates from the predictions of the JMAK equation. Even so, this model is still widely used for prediction of recrystallization progress due to its simplicity and thus, it is considered as a standard model for isothermal recrystallization kinetics [24].

Table 1 Values of Avrami exponent for various conditions[1]

Growth Dimensionality	Site-saturated nucleation	Continuous nucleation
3-D	3	4
2-D	2	3
1-D	1	2

There have been some attempts to improve the JMAK model such as a model incorporating heterogeneous nucleation by Cahn [25], model incorporating variation in growth rates due to strain gradients by Furu et al. [26], Microstructure Path Model [27] and model by Doherty et al. [28]. All of these models allow for variable nucleation and non-constant growth rates. Still, these models assume random nucleation and isotropic growth.

When considering the variations in nucleation rates, inhomogeneous nucleation sites distribution , effect of texture on stored energy and many other such effects, the analytical approaches seem to be inadequate [29]. Several microstructural models based on Cellular models [15,16], Computer Avrami models [26], Monte-Carlo models [29], and cellular automata models [16] have been developed. These models are able to describe the microstructure evolution more accurately. The drawback of these models is that they require quite a lot of computing knowledge and computing time. The time required to develop such models for specific cases is quite long as well. Moreover, these models require more input data. For example, for these models, some initial microstructure or distribution of stored energy is given as input.

Analytical models are easier to use because of their simplicity and they don't require long computing times. These models require much lesser input parameters. In most of the cases, the predictions of these analytical models are reasonably accurate, especially when concerned with the progress of recrystallization. Moreover, the parameters of these models are simple and relate to fundamental phenomena. For example, the Avrami exponent relates to the type of nucleation and growth, which can be easily verified experimentally.

Even though JMAK and its assumptions are omitting influence of certain parameters, in some cases the model can predict the actual behaviour. Based on considerations of all available models, it seems that modified JMAK might yield satisfactory predictions in a reasonable amount of time.

JMAK FOR NON-ISOTHERMAL CONDITIONS

As mentioned earlier, due to the lower requirements for computing time and its simplistic description, JMAK model is being used for analysis of experimental recrystallization data. There are many variations of JMAK models developed for non-isothermal conditions. The question is then; which version would be

---

[1] When the Avrami exponent is between these integers for the specific cases, then it is a case of decreasing nucleation rate.

perfect in this particular case. Cahn [25] has modified the JMAK equation to fit the case of heterogeneous nucleation, with focus on grain boundary or corner nucleation scenarios. Here, the isotropic grain growth and constant grain growth rate assumptions are kept. Earlier it was mentioned that nucleation would be preferable at the boundary between deformed pearlite and ferrite, pointing to heterogeneity. But, when the materials are cold-deformed to high reductions, the pearlite bands would be very close to each other. Therefore, the distribution of potential nucleation sites would seem to approach homogeneous scenario. This has been observed for heavily deformed materials [29]. Hence, if the assumption of the homogeneous nucleation is applied, the Cahn's model doesn't offer any reasonable improvement.

The model by Vandermeer and Rath [27] incorporates decreasing grain growth rates, while grains still grow isotropically. It keeps other assumptions of JMAK as they are. Decrease in growth rate with time is quite relevant for case of isothermal annealing. In case of continuous heating, the decrease in growth rate caused by reduction of stored energy will be compensated by an increase in temperature due to heating. This compensation would be possible only if heating rate is high enough. Therefore, the assumption of constant growth rate might be applicable for continuous heating.

The modified model by Doherty et al. [28] incorporates variable nucleation and growth rates. Experimentally it is seen that most of the nucleation during recrystallization approximates to site-saturation [13] and therefore, having variable nucleation rates is not very relevant. These scenarios, justify that for the case of continuous heating of heavily cold-deformed material, the basic JMAK model with modifications for continuous heating can be used with possible satisfactory results. The modified JMAK model for non-isothermal conditions by Farjas et al. [32] presents more accurate results than other models. The detailed derivation of the equations has been provided in the Appendix A. For the case of continuous heating, the JMAK equation becomes as follow:

$$\alpha = 1 - exp\left\{-\left[k_o C \frac{E}{\beta K_B} p\left(\frac{E}{K_B T}\right)\right]^{m+1}\right\} \tag{2}$$

where: α is the transformed fraction, k_o is the pre-exponential factor (rate constant) which includes the nucleation and the growth rates, E is the activation energy, β is the heating rate, K_B is the Boltzmann constant, m+1 is the Avrami exponent, T is the temperature and C is a constant as described below:

$$C = \left[\frac{(m+1)!\,E^{m+1}}{\prod_{i=0}^{m}(E_N + iE_G)}\right]^{\frac{1}{m+1}} \tag{3}$$

where, E_N and E_G are the activation energies for nucleation and growth respectively.

It has been mentioned by Farjas et al. [32] that the isokinetic case is applicable in the cases where the transformation rate is dependent only on temperature and not on the thermal history (heating rate). This is seen when, E_N=E_G or in the case of site-saturation nucleation. For cases, where $E_N \neq E_G$, then the general case is applicable. But, it was found that, in the cases of E_N>>E_G and E_G>>E_N, the isokinetic description is more accurate. Based on these considerations and along with the assumption that the nucleation in recrystallization is of site-saturation type for most cases, equation (4) would be used for predictions for kinetics in our case.

$$\alpha = 1 - exp\left\{-\left[k_o \frac{E}{\beta K_B} p\left(\frac{E}{K_B T}\right)\right]^{m+1}\right\} \tag{4}$$

EXPECTED OUTCOMES FROM JMAK MODEL

The fitting of data using modified JMAK equation (4) should result in derivation of following parameters: activation energy (E), rate constant (k_o), and Avrami exponent (m+1). Using these parameters, predictions for the studied alloys can be made with other conditions. Rate constant can give qualitative idea about the amount of nucleation sites, ease of nucleation and grain growth. It consists of growth and nucleation constants, which are G_o and N_o respectively. Activation energy would account for activation energy of grain boundary migration in the alloy. Avrami exponent would give idea about the type of nucleation and growth. It will help in determining whether the nucleation is site saturated, continuous or decreasing with time and moreover, it will help in determining the dimensionality of the growth. The Avrami exponent would be derived experimentally. Also, as activation energy for recrystallization is equal to activation energy of self-diffusion, the values for activation energy of self-diffusion of Fe in these alloys would be used as an input parameter.

POSSIBLE PITFALLS OF JMAK

Because of the simplicity of the JMAK model, there is a possibility of deviations from experimental data. Thus, while analysing the results from the fitting of this model to the experimental data, some possible pitfalls must be kept in mind. The assumption about homogeneous and random nucleation is one of the first that could be wrong. Especially in the case of dual phase steels, the nucleation is generally observed at the boundaries of deformed ferrite and pearlite [15]. Even though it is mentioned that the decrease in growth rate would not be an important factor for continuous heating, deviation might be expected at lower heating rates [27]. At low heating rates, the rise in temperature might not be fast enough to compensate for reduction in growth rate. As the microstructure contains two phases, the growth of recrystallized ferrite nuclei might not always be isotropic. Presence of pearlite bands might prevent the growth in some directions.

2.4.2 GRAIN GROWTH MODEL

The correlation of the parameters from the JMAK model with the microstructure observations is very important. Those can be: pre-exponential factor (k_0) and the Avrami exponent (m+1). As mentioned in section 2.4.1, the Avrami exponent is one of the JMAK parameters which can be deduced from microstructure characterization. Therefore, Avrami exponent could be used as an input in the JMAK model. From JMAK model other fitting parameters could be deduced. The pre-exponential factor consists of nucleation and growth rates. If the nucleation and growth rates are determined experimentally, then pre-exponential factor (k_o) could also be verified experimentally. One of the models to determine growth rates for recrystallized grains is being described below.

The theory for the grain growth in non-isothermal conditions is based on the grain coarsening model, which is dependent on the curvature driven growth. This model can be also used to model the grain growth during recrystallization by adjusting it (as described in Appendix B). The major changes relate to the expression for the driving force, which, in our case includes the contribution from the stored energy of deformation.

The equation describing the growth of the grains for non-isothermal conditions is as follows:

$$D^2 - D_o^2 = \frac{KR}{\beta E}\left\{\left[T_f^2 \exp\left(-\frac{E}{RT_f}\right)\right] - \left[T_i^2 \exp\left(-\frac{E}{RT_i}\right)\right]\right\} \tag{5}$$

$$K = 4\alpha\gamma_{app}M_o \tag{6}$$

where: D is the average diameter of the growing grains at 50% RX condition, D_o is the average diameter of the grains at the temperature T_i (which would correspond to 10% RX condition), R is the universal gas constant, β is the heating rate, T_f is the final temperature (corresponding to 50% RX condition), E is the activation energy, γ_{app} is the apparent surface energy of the grain boundary (explained in the Appendix B), M_o is the pre-exponential factor of mobility of the grain boundary.

The pre-exponential factor in JMAK model is described as –

$$k_o = \left(\frac{\sigma N_o {G_o}^m}{m+1}\right)^{\frac{1}{m+1}} \tag{7}$$

where: N_o and G_o are the pre-exponential factors of nucleation rate and growth rate equation respectively. Therefore, G_o is expressed as,

$$G_o = M_o F \tag{8}$$

where F is the driving force for the grain boundary migration.

From equations (6), (7) and (8) it can be seen that the pre-exponential factor of the JMAK and the parameter K from the grain growth model can be related and they can be used to derive the mobility of the grain boundaries.

$$k_o = \left[\frac{\sigma N_o}{(m+1)}\left(\frac{KF}{4\alpha\gamma}\right)^m\right]^{\frac{1}{m+1}} \tag{9}$$

Moreover, using the expression for driving force F (as described in Appendix B, equation (18)) the k_o can also be described as,

$$k_0 = \left[\frac{\sigma N_0}{m+1}\left(\frac{K}{2\alpha D}\right)^m\right]^{\frac{1}{m+1}} \tag{10}$$

where: D is assumed as D_o (D at 10%), because the theory works well when the grains are un-impinged.

Thus, it can be seen that the grain growth analysis and amount of nuclei from microstructure analysis can directly lead to the pre-exponential factor.

2.4.3 CHANGE IN ACTIVATION ENERGY BY ALLOYING

As mentioned in section 2.3.2, the solute drag is manifested in the form of reduction of grain boundary migration rate (mobility). This can be verified experimentally by looking at the growth rates. But, to describe the effect of solute drag by using theoretical models, the reduction of grain boundary mobility is represented by an increase in the activation energy of grain boundary migration. Therefore, a theory describing the changes in activation energy based on solute drag effect is used here. The equation describing the changes in activation energy is:

$$E = E_D + E_i + (\beta - 1)z\varepsilon(1 - c_b)^2 \tag{11}$$

where, E is the activation energy for grain boundary migration, E_D is the activation energy for self-diffusion of the solute atom in the matrix, E_i is the interaction energy between the solute atoms and the boundary, z is the co-ordination number, ε is the heat of mixing of the solutes in the grain boundary, c_b is the concentration of the solute at the boundary and β represents the ratio of the partial areas of the elements in the boundary. The detailed derivation of equation (11) is given in Appendix C. It has been explained in Appendix C, that β > 0 and even ε would be negative if the solute elements favour interactions.

The theory assumes binary solutions in the grain boundaries. In our case, at the grain boundaries, there would be a binary solution of Mn-Si.

In the low Mn alloys, it is being assumed that the influence of Mn is so low that it would not interact with the Si atoms at the grain boundaries. Thus, for these alloys conventional solute drag theory described by equation for mobility [18], can be used:

$$m = \frac{D_o \exp\left[\frac{-(H_D + H_i)}{kT}\right]}{zB_o kTc_o} \tag{12}$$

Similar is the case for alloy 2A (0Si2Mn), where the influence of Si is very low and thus, neglected.

For the alloys with comparable Si and Mn contents, the equation (11) should be used. The ε is given by the interaction parameter for Mn-Si as given in [33], $\varepsilon_{Mn\text{-}Si}$ = -12 kJ/mol. The parameter β would be a deciding factor for the interaction between the solute atoms in the grain boundary.

2.5 CURRENT STATE OF RESEARCH ON FERRITE RECRYSTALLIZATION

As mentioned earlier, the ferrite recrystallization affects the austenite formation. Therefore, most of the research in ferrite recrystallization focuses on understanding the link between ferrite recrystallization and austenite formation. For example, Li et al. [6] have studied the effect of heating rate on ferrite recrystallization and austenite formation. The major part of the work concentrates on finding out whether the ferrite recrystallization has completed before the austenite starts to nucleate. If it is not yet completed, then how does it affect austenite formation? The stages of nucleation and growth of recrystallized grains have not been studied in detail. Similar research for studying the influence of ferrite recrystallization on austenite formation has been carried out [3],[34]. Most of these studies are carried out in conditions which bring about the overlap between austenite nucleation and ferrite recrystallization. Even though it is known that ferrite recrystallization affects austenite formation, the reverse is also true. This point has been illustrated by Chbihi et al. [3], where it was seen that as the austenite nucleation starts, the ferrite recrystallization slows down considerably.

Some research on the effect of heating rate on progress of recrystallization has been carried out, as seen in work of [4,6,33-34]. Most of these studies, focus on the effect of heating rate on the connection between ferrite recrystallization and austenite formation. Muljono et al. [35] have observed that higher heating rates lead to finer recrystallized grain structure. This was reasoned by the fact that at higher heating rates, the recrystallization started at higher temperatures which led to higher nucleation rates. Even though it is hypothesised, the authors do not present quantified proof. It does point to a fact that heating rate would result in changes in the nucleation kinetics for recrystallization. Sahay et al. [36] say that lower heating rate results in pancaking of microstructure but no quantification is available as well. Therefore, it can be agreed that the variation in heating rates would lead to changes in the nucleation kinetics, growth of the recrystallized grains and also the shape of the grains. The quantified results to prove these statements are missing.

It was found by Huang et al. [4] that the kinetics of recrystallization were different for materials with different pearlite band spacing. Therefore, the effect of initial microstructure and consequently, the effect of alloying is important in ferrite recrystallization kinetics. Such an effect was also seen in work of Peranio et al. [34], where the ferrite recrystallization was different at different depths of the rolled material due to a difference in the initial microstructure at these positions. The alloying elements affecting the initial microstructure is seen in [36–38]. The observations made by Huang et al. [4] convey that the kinetics of recrystallization are dependent on pearlite band spacing, which were explained in more detail by the work of Peranio et al. [34]. They concluded that, when the pearlite band spacing is comparable to the distances of recrystallization nuclei, it might lead to restriction of growth of recrystallized nuclei in two dimensions. Moreover, it was also suggested that the growth of these nuclei can be reduced since the number of curved surfaces are reduced.

Effect of alloying elements on the progress of ferrite recrystallization is not very clear. In general it has been agreed that Mn retards ferrite recrystallization [4]. But the effect of Silicon is not very clear. Drumond et al. [37] have claimed that Si tends to accelerate recrystallization. The reason for Si affecting the recrystallization has been reasoned as related to changes in initial microstructure with Si [37]. The work of Drumond et al. [37] does point to role of Silicon in recrystallization kinetics, but the work considers only two relatively small amounts of Si, which might give inconclusive results. The research gives no indication about the effect of Si at higher concentrations. Also, the effect of Silicon in presence of Manganese on ferrite recrystallization is not yet investigated.

The work by Calcagnatto et al. [40] says that the amount of Mn affects the cementite distribution. Also, Drumond et al. [37] have suggested that the changes in the recrystallization behaviour have been because of Si affecting the distribution of the pearlite. Therefore, the quantity of alloying elements will affect the amount and the distribution of the pearlite, which in turn should affect the recrystallization behaviour.

In the work of Huang et al. [4], it was seen that the apparent activation energy for recrystallization was different for different alloys. Moreover, the increase in the activation energy was reasoned to be because of the solute drag effect of Mn and Mo. This suggests that the ferrite recrystallization can be affected by the alloying elements due to solute drag effect during the growth stage. There have been some theoretical models on the role of alloying elements on the grain boundary motion during recrystallization [41]. These studies have been done mainly for alloys with very low contents of alloying elements. There have been theoretical models by Sundman [42] where the solute drag in case of higher alloying contents have been considered. The solute drag is considered quite significant during grain growth and thus, it is expected to be significant even for recrystallization. When the grain growth data for alloys is compared with pure alloys, the difference in mobility is quite high [43]. This change in mobility is also expressed as an increase in activation energy for the grain boundary migration [44]. Till now, most of the studies of solute drag have considered only one type of alloying element. The solute drag in presence of multiple different solutes is not well understood. Multiple solutes can also lead to co-segregation effects as seen in [45]. Guo et al. [45] have seen that such co-segregation can enhance the effects of solute drag by orders of magnitude. In the other work of Guo et al. [33], the interaction parameter values for various alloying elements pairs are reported and Mn-Si pair has one of the strongest interactions in austenite as well as ferrite grain boundaries. Even though the co-segregation of Mn and Si has been observed experimentally, it is not yet well known how the ratio of Mn and Si in the alloy will affect the 'coupled solute drag effect'. The effect of such co-segregation might also have a significant impact on recrystallization.

2.6 MISSING GAPS IN RESEARCH

As mentioned earlier, most of the work on ferrite recrystallization has been carried out with the aim to understand its influence on austenite formation. The austenite formation in itself slows down the ferrite recrystallization [3]. Therefore, for studying the ferrite recrystallization independently, the heating rates should be selected such that the possibility of overlap with austenite formation would be very small.

Also, the kinetics of recrystallization have been studied mostly using hardness tests, property measurements, microscopy [14] and sometimes by using synchrotron radiation [46]. The microscopy based and the property based experimental techniques require many samples and are time-consuming. Therefore, the number of points recorded for the recrystallization curve are usually limited. Synchrotron can record the points at very small intervals, but it is not readily available. Therefore, an experimental technique that can record large number of points with few samples would be ideal. This would also help in avoiding the differences between the samples. Moreover, a recrystallization curve which has many recorded points would help in getting better fit with the recrystallization models. More accurate kinetic parameters would certainly help in better understanding of recrystallization.

Many researchers Muljono et al. [35] and Sahay et al. [36] have observed that the heating rates affect the nucleation and also the growth of the recrystallized grains. These observations have been qualitative in nature. There is a need to quantify the effect of heating rate on number of nuclei, growth rates and grain shapes. This information can also be obtained from the model fitting of recrystallization data at higher heating rates.

It has been described by Huang et al. [4] and Peranio et al. [34] that pearlite band spacing in rolled steels can cause restriction in growth. Along with restrictions to the growth, the boundaries between deformed pearlite and ferrite serve as nucleation sites for recrystallized grains. Therefore, the influence of change in pearlite band spacing for similar amount of pearlite might lead to change in nucleation behaviour as well. This aspect has not been studied much in detail. The combined effect of pearlite band spacing and amount of pearlite on the nucleation and growth needs to be studied.

The effect of alloying elements on the amount and distribution of pearlite is known qualitatively [37], [40]. The amount and distribution of pearlite affects nucleation and growth as seen earlier, therefore, the effect of alloying elements with this aspect in mind is to be studied. Again it has been observed by researchers that the alloying elements will cause reduction in mobility, as explained earlier. How does the mobility (also interpreted as a change in activation energy) change with alloying content? This knowledge would be important to be able to control the recrystallization behaviour with alloying. As seen in work of Drumond et al. [37] and many others, the alloys used have many different alloying elements and therefore, it is quite difficult to separate the effect of individual elements. Therefore, the conclusions regarding the role of alloying elements are not very clear and in many cases contradictory.

The activation energy for grain boundary migration and therefore, recrystallization, increases due to solute drag effect [44]. It is expected that the solute drag effect increases with the addition of alloying elements. The co-segregation effect of multiple solute elements is a relatively new concept [45]. It is not clear, how does the co-segregation effect changes when the ratio of these alloying elements with each other changes. Also, the effect of Mn is known that it retards recrystallization [47], but the effect of Si is studied only for low concentrations [37]. Guo et al. [45] have investigated the growth of pro-eutectoid ferrite by incorporating the 'co-segregation' of Si and Mn. During the investigation, there is also austenite (γ) present in the microstructure. This can affect the distribution of Si and Mn in ferrite and austenite, eventually affecting the growth of ferrite. During the ferrite recrystallization, there is no austenite present in the microstructure and therefore, the situation would be a little bit different. Therefore, the behaviour of Si in presence of Mn during recrystallization is not very clear. This needs to be quantified and investigated, given that Si and Mn are important alloying elements in Dual Phase Steels.

2.7 ADDRESSING THE MISSING GAPS

To avoid the interference from the austenite formation during the study, the heating rates used were not very high. This is because high heating rates can lead to overlap between ferrite recrystallization and austenite formation [6]. More details about the choice of heating rates are discussed in Section 3.

An experimental technique that would allow for recording of more number of points on the recrystallization curve is required. Currently, the experimental techniques to follow the recrystallization kinetics are separated in two categories – ex-situ and in-situ. Most common ex-situ methods include Light optical microscopy (LOM), Scanning Electron Microscopy (SEM), Electron Backscattered Diffraction (EBSD), property measurements (eg. Resistivity measurements, Hardness measurements) [24]. All experimental methods have some drawbacks. In case of ex-situ microscopy methods, even though they give quite an accurate description of the microstructure evolution during recrystallization, these methods require samples to be prepared for many temperatures to identify the recrystallization start and finish. This is very time-consuming and labour intensive. The problem of many samples exists for all ex-situ methods. Moreover, the microscopy methods focus only on specific area of sample surface and there is no information about the bulk microstructure evolution [48]. For the case of property measurements, the correlation with microstructure evolution is not straightforward [14]. The in-situ methods tend to solve the problem of time and too many samples. The most common in-situ methods are High Temperature Scanning Electron Microscopy (HT-SEM), High Temperature Electron Back Scatter Diffraction (HT-EBSD), High Temperature X-Ray Diffraction (HT-XRD) [14]. Even though the whole recrystallization curve can be traced with these methods there are some limitations. There have been some studies detailing SEM-EBSD analysis at temperatures in the range of 1000°C [49]. These experiments have been carried out at a high isothermal temperature, not at different temperatures with some heating rate. Moreover, performance of detectors might not be optimal at high temperatures. Recently, in-situ TEM has been used to capture images at different temperatures during heating [50]. The study doesn't mention the heating rates used. Even though the high heating rates might be possible for SEM/TEM, the surface quality might get affected due to decarburization. Performing in-situ EBSD at higher heating rates seems difficult due to the times required to record the EBSD patterns for numerous points for the selected area. Also, at higher temperatures, the recording times for EBSD are longer. Based on consideration of all these factors, it was concluded that in-situ HT-XRD might be the most fitting technique for the present study. Even this method can have some pitfalls, which would be discussed later in section of experimental techniques.

The thesis would aim to fit the experimental recrystallization curve to an analytical model that describes recrystallization (see Section 2.4.1 and Appendix A). This would give some parameters related to the kinetics of recrystallization, such as activation energy, nucleation and growth rates and others. These parameters could be correlated to the observations done by the microscopy analysis. Thus, this approach would provide meaning to the parameters from the recrystallization models. A detailed microscopy analysis for the microstructures would be carried out, so that the quantification for the effects such as changes in the number of nuclei, grain shapes and grain growth with the changes in alloying could be explained.

Also, to separate the individual effects of the alloying elements, model alloys have been used in this thesis. These model alloys make sure that the effects due to Si and Mn, are the sole effects that are being observed. Therefore, it would make the results and inferences more reliable, as there would not be other influences. This would shed more light on the contradictory results. Such model alloys would help in correlating the effect of Si and Mn on activation energy for the recrystallization, number of nucleation sites, and growth rates. There are also some alloys, where the Si content changes in presence of a constant Mn content. These alloys should help in explaining the effect of Si on recrystallization in presence of Mn.

With this plan for research, the thesis would aim to be able to point out the changes in the recrystallization temperatures more accurately, generate accurate parameters from model fitting of experimental results, and better quantification of microstructural observations. These results together would be used to generate a simple analytical model to describe the recrystallization for other conditions.

3. EXPERIMENTAL TECHNIQUES AND PROCEDURES

3.1 INVESTIGATED MATERIALS

Since the main question to be answered in the present thesis is the influence of Si and Mn on recrystallization, model alloys are used. Therefore, steels with varying compositions of Si and Mn, as shown in Table 2 are used. It has been attempted to keep the other alloying elements to a bare minimum. This would ensure that the observed effects would be only due to these alloying elements. Si and Mn are important alloying elements in steels. In case of Dual phase steels, Si is important as an element which prevents the precipitation of carbides. Mn is an austenite stabilizer. Mn in combination with appropriate heat treatment promotes austenite formation. Therefore, Mn plays a role in determining amount of martensite in dual phase steels. This is a very basic description of role of Si and Mn. In reality, the effects of Si and Mn are quite complex and require more in-depth investigations. The chemical compositions of the steels are given in Table 2. All these alloys are coded as mentioned in the Table 2.

Table 2 Chemical compositions of the alloys used

Alloy code	C	Si	Mn
2A	0,19	0,06	1,95
2B	0,20	0,39	1,96
4A	0,20	0,98	2,03
5A	0,20	1,56	2,01
6A	0,20	0,38	0,08
7A	0,20	0,94	0,09
7B	0,20	1,51	0,09

The alloys were prepared using laboratory vacuum caster. The ingots of each alloy were 23 kg with a rectangular cross-section of 100 X 100 mm^2. These ingots were first rough rolled at 1250 °C to 40mm thickness. There was no homogenization treatment performed. Afterwards, the plates were hot-rolled at 1230°C in 7 passes to a thickness of 4mm making it 96% reduction. Finally, the sheets were cold-rolled to thickness of 1mm in one pass. Therefore, the cold-rolling reduction was 75%.

3.2 EMPLOYED HEATING RATES

The selection of heating rate for the continuous heating experiments is important to be able to get an idea about effect of heating rate on recrystallization kinetics. Higher heating rates lead to an overlap of austenite formation and ferrite recrystallization [3]. Therefore, they were avoided. This allowed study of recrystallization without interference from phase transformation. The heating rates selected were 0.1 K/s, 1 K/s and 5 K/s. The upper limit of heating rate is also due to the limit of the instrument used. The heating stage and in-situ XRD used has maximum heating rate of 8.33 K/s (500K/min). In addition, the required amount of counts to be registered by the detector would require bigger temperature intervals. Thus, to have results with smaller errors, the 5 K/s (300K/min) was maximum heating rate possible. Additionally, the heating rates above this particular one, cause the overlap between austenite formation and ferrite recrystallization for some of those alloys.

3.3 HEAT TREATMENTS

During the X-ray Diffraction analysis, the samples were subject to heat treatments with heating rates as described in the previous section. The samples were heated, using the heating stage of the XRD, from room temperature to a temperature of 1050°C at various heating rates. As the temperature of 1050°C was reached, the sample was quenched to room temperature with a cooling rate of 8.33 K/s. These heat treatment cycles were used to obtain the complete recrystallization curve. From the recrystallization curves for each alloy, the temperatures for 10%, 50% and 100% RX were determined. Additional samples for microscopy analysis were heat treated. The samples were heated from room temperature to the 10%, 50% and 100% RX temperatures, with a heating rate of 1 K/s. Once these temperatures were reached, the samples were quenched to room temperature with cooling rates of 8.33 K/s.

3.4 SAMPLE PREPARATION X-RAY DIFFRACTION

The samples for X-ray Diffraction (XRD) analysis, were cut from the cold rolled sheets. The size of these samples is 20 X 10 mm^2. The surface parallel to ND (normal direction) was prepared by mechanical grinding and polishing. The samples were grinded with SiC papers till 4000 grit size and then, polished with cloth and 1µm diamond solution.

3.5 XRD SETUP

The continuous heating experiments are done using Bruker D8 X-ray diffraction (XRD) machine. The setup of the machine is shown in Figure 4. The samples of size 20 X 10 mm^2 were mounted on the heating stage. The heating stage is provided by Anton Paar, with Eurotherm temperature controller. It is using MODBUS communication platform.

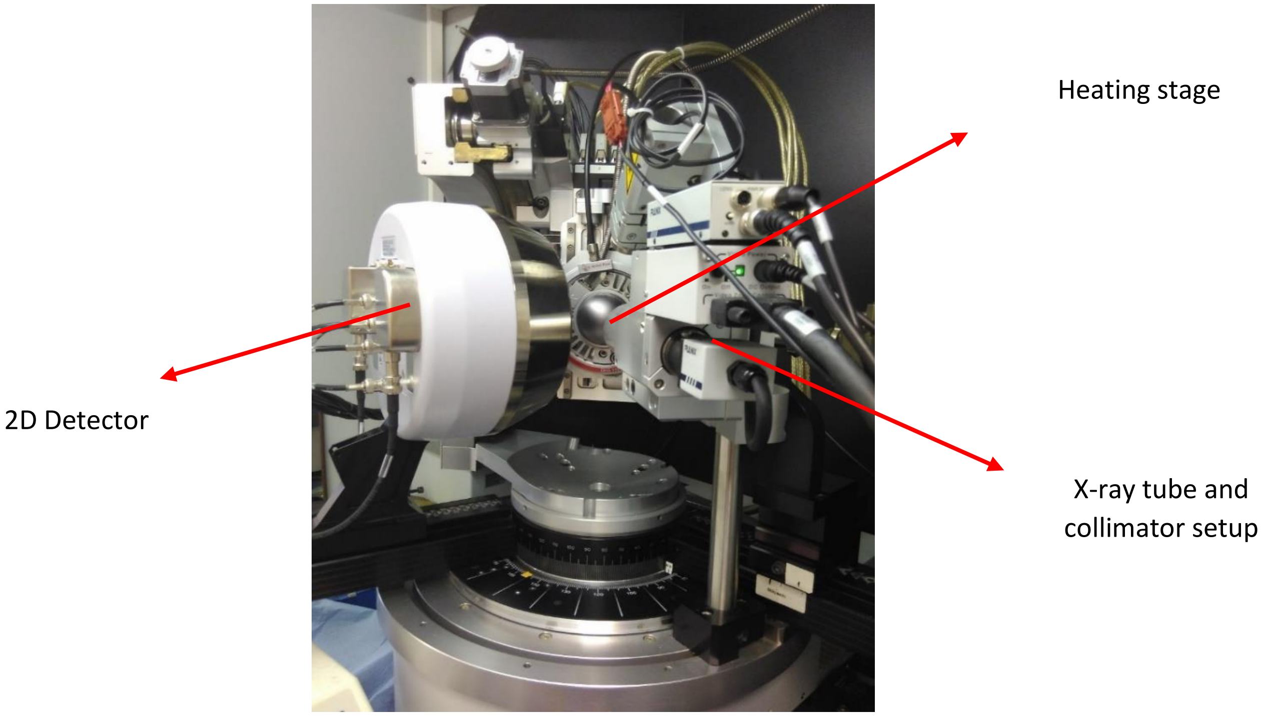

Figure 4 Panalytical D8 XRD setup

The heating stage is designed by Anton Paar, which has Si_3N_4 plate as the base that separates the thermocouple and heating elements from the sample. Heating is resistive heating. The important consideration here is that the thermocouple is measuring the temperature of the heating element, which is not in direct contact with the sample. Therefore, there might be a difference between the temperature of the sample and the heating element. To solve this problem, calibration of the temperature controller is done by using a standard transformation with known phase transformation temperature. In our case, it was low carbon steel with ferrite-to-austenite transformation start temperature of 993 K. Nevertheless, at higher heating rates this can be a major problem. Therefore, to check the accuracy of measurements at 5K/s heating rate, the austenite formation temperature obtained from XRD was compared with the one observed by dilatometry study. The deviation was mostly ±10 K.

To prevent oxidation of the sample surface at high temperatures, a graphite dome as shown in the Figure 4 is mounted on top of the stage. Inside the graphite dome, Helium gas is injected to provide an inert atmosphere. The inert atmosphere also helps in preventing the decarburization of the surface.

Diffraction patterns consist of Debye-Scherrer rings as shown in Figure 5. Different types of detectors capture different parts of these rings. Greater the part captured, more information can be gained from such experiments [51]. The one dimensional Position Sensitive Detectors (PSD) are widely used for detection of X-rays. In the case of materials with strong textures, point detectors might lose information. There have been attempts to use PSD detectors to capture greater parts of Debye rings by vertical movements, but these methods are very time-consuming. 2D detectors capture full or part of Debye Scherrer rings directly due to their construction. As the 2D detectors capture the part of Debye ring at one time, they are much faster than PSD detectors in data collection [51]. This allows for more convenient data collection for nucleation and recrystallization kinetics.

For detecting the X-rays, Bruker-AXS General Area Detection Diffraction System (GADDS) has been used. The detector was placed at 9 cm from the sample. This is closer than the distance of 17 cm used for texture measurements. One of the reasons, is that the system is stationery, which allows for closer position. It also helps in recording higher intensity, which is important for more accurate detection of intensity changes.

Even with the advantages of faster and more accurate data recording with in-situ 2D XRD, there are some disadvantages. The major pitfall is that, only a part of the Debye-Scherrer rings are being recorded in our case. Therefore, in case of textured materials, important parts can be missed. It is quite possible that the recrystallization starts in grains with some particular orientation and their XRD reflections are not recorded. In such a case, the recrystallization start temperature would be perceived wrongly. Also, for higher heating rates faster recording should be used. Unfortunately, due to restrictions of the setup, it is not possible. Higher energy source would help in reduction of signal to noise ratio, which can make the temperature estimation more accurate.

The detector and the sample stage are kept at angle of $2\theta = 75°$ (see Figure 4) and $2\omega = 37.5°$, so that all the important peaks of ferrite and austenite are recorded. The ferrite peaks captured are {110} at 52°, {200} at 76° and {211} at 98°. The austenite peaks captured are {111} at 50°, {200} at 59° and {220} at 87°.

The X-ray source used in the experiments is CoKα with the voltage of 30kV and current of 40mA. The X-ray collimator has 3mm diameter.

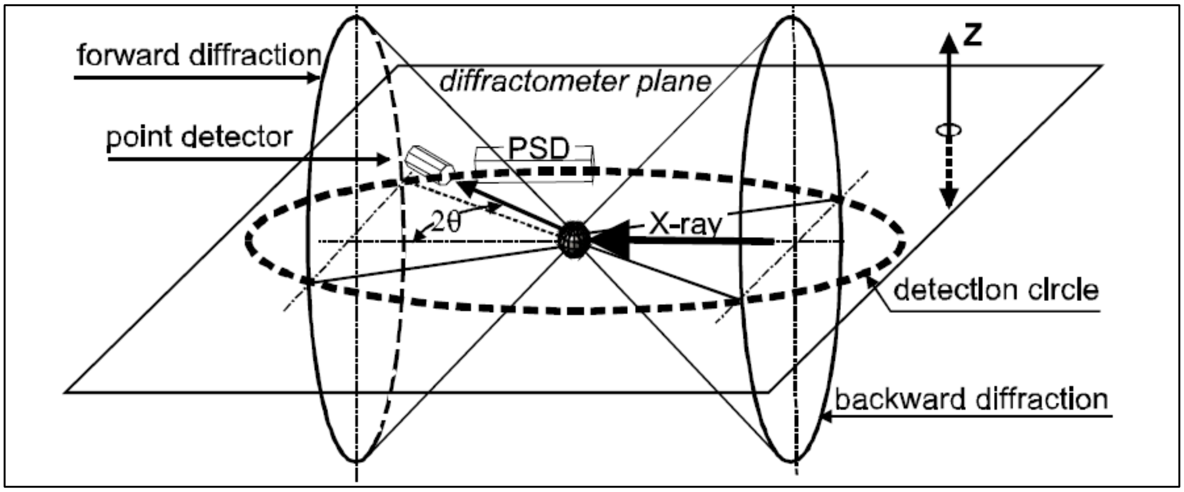

Figure 5 Diffraction patterns in 3D space from a powder sample and the diffractometer plane in a conventional diffractometer [52].

While carrying out the experiments, the time interval during which the 2D-detector records the X-rays is a very important parameter. This time is related to the time for which the shutter of the detector is open. The longer the integration time, the higher is the intensity and accuracy of the X-ray spectrum recorded. In case of continuous heating rates, very long integration times can lead to higher inaccuracies in estimating recrystallization start and finish temperatures. Thus, a fine balance between the need for enough signal intensity and temperature accuracy is necessary. For very slow heating rate, i.e. 0.1 K/s, the integration time of 3 seconds would mean temperature interval of 0.3 K for each frame. It was decided that for the sake of higher signal-to-noise ratio, the integration time would be 30s. This would mean a temperature range of 3K, which is judged to be small enough to distinguish the recrystallization start and finish accurately. Matching temperature interval was chosen for 1 K/s heating rate. This resulted in 3 seconds recording time. For the heating rate of 5 K/s, the 3 K interval would mean integration time of 0.6 seconds. This is too small for collecting meaningful amount of X-rays. Moreover, the time for processing the data (time for saving the data) is approximately 1 second. Thus, to have meaningful counts of X-rays, time of 3 seconds was chosen as the integration time even for 5 K/s.

The temperature interval is defined as,

$$Interval_{temp} = Total\ processing\ time\ (s)\ X\ heating\ rate\ (s) \tag{13}$$

The integration times (processing times) and the temperature intervals during the measurements are mentioned in the Table 3.

Table 3 Temperature interval and processing times

Heating rate	Total processing time (s)	Temperature interval (K)
0.1 K/s	30	3
1K/s	3	3
5K/s	3	15

3.6 X-RAY DIFFRACTION DATA PROCESSING

The 2D detector records the images as shown in Figure 6. After the experiment is completed, the unwarping of the data is done. Unwarping is a process to account for the curved shape of the 2D detector. Thus, it applies some correction to intensity and position of the peaks. Afterwards, the recorded fragments of the Debye-Scherrer rings are integrated into peaks, to get the XRD spectrum for each frame. The integration is done over a width of 45°. The example of the spectra can be seen in Figure 7. After this step, the intensity and the width of the peaks has to be calculated. Therefore, Rietveld refinement [53] is carried out, to enable theoretical spectrum to be fitted to the experimental one. It is used to calculate the intensity and the peak widths. In this way, the intensity of various peaks is recorded, which results in a plot of intensity vs temperature, as shown in Figure 8.

The recrystallization can be detected in two ways in the XRD data – texture changes leading to a change in peak intensity [54], or dislocation density changes leading to changes in the peak widths[2][55]. Peak width changes are very small and are affected by the scatter, thus for calculation purposes, the changes in intensity of (211) ferrite peaks was considered, as the signal to noise ratio is quite high. Since often in cold-rolled sheet steels, the predominant texture element is α fibre the highest intensity of (211) peak is understandable[3] [54]. The texture during recrystallization changes to γ which will lead to a decrease of this fibre's intensity and increase in others as seen in Figure 7. Thus, start of recrystallization is considered as point at which, there is a sharp decrease in the intensity of (211) peaks.

The temperature effects are visible in the XRD spectra as well. As the temperature changes, the lattice expands leading to changes in the position of the peaks. The temperature changes also lead to changes in the intensity. This can be seen in form of continuous decrease in the intensity, as seen in Figure 8. Some signal from the graphite dome is also captured in the X-ray diffraction signal.

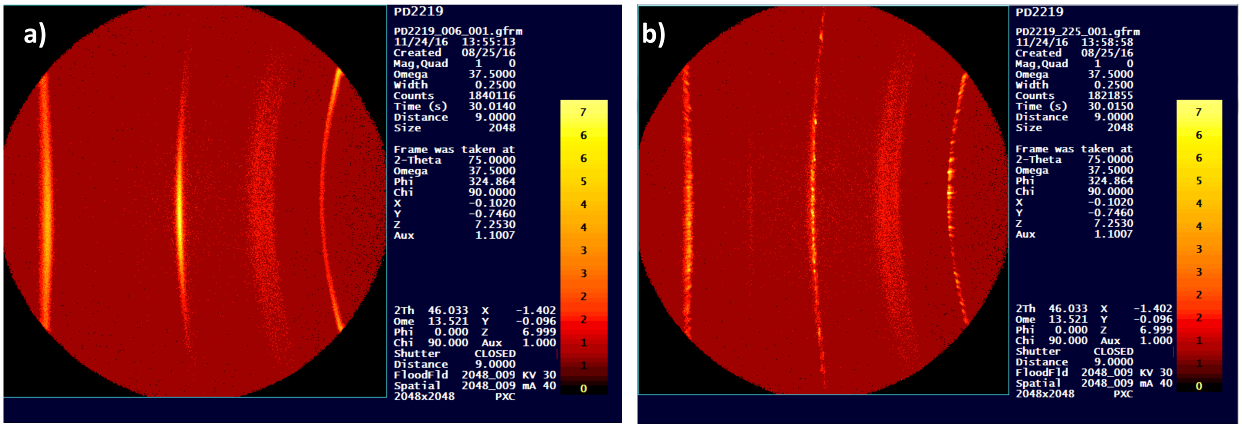

```
PD2219

PD2219_006_001.gfrm
11/24/16  13:55:13
Created   08/25/16
Mag,Quad     1    0
Omega      37.5000
Width       0.2500
Counts     1840116
Time (s)   30.0140
Distance    9.0000
Size          2048

Frame was taken at
2-Theta    75.0000
Omega      37.5000
Phi        324.864
Chi        90.0000
X          -0.1020
Y          -0.7460
Z           7.2530
Aux         1.1007

2Th  46.033  X     -1.402
Ome  13.521  Y     -0.096
Phi   0.000  Z      6.999
Chi  90.000  Aux    1.000
Shutter     CLOSED
Distance    9.0000
FloodFld  2048_009 KV 30
Spatial   2048_009 mA 40
2048x2048       PXC
```

```
PD2219

PD2219_225_001.gfrm
11/24/16  13:58:58
Created   08/25/16
Mag,Quad     1    0
Omega      37.5000
Width       0.2500
Counts     1821855
Time (s)   30.0150
Distance    9.0000
Size          2048

Frame was taken at
2-Theta    75.0000
Omega      37.5000
Phi        324.864
Chi        90.0000
X          -0.1020
Y          -0.7460
Z           7.2530
Aux         1.1007

2Th  46.033  X     -1.402
Ome  13.521  Y     -0.096
Phi   0.000  Z      6.999
Chi  90.000  Aux    1.000
Shutter     CLOSED
Distance    9.0000
FloodFld  2048_009 KV 30
Spatial   2048_009 mA 40
2048x2048       PXC
```

Figure 6 2D Detector scan for alloy 2A (0Si2Mn) at heating rates of 0.1 K/s a) before RX at room temperature b) after RX at 720°C

The recrystallization could also be detected as the point when the Debye-Scherrer rings start becoming spotty as seen in Figure 6a, due to nucleation and growth of individual grains. This method is suitable if a higher energy source is used for X-rays. In current XRD setup, such clear distinction is not possible.

---

[2] The dislocation density changes are also used to detect recovery. The differences in these changes during recovery and recrystallization is that, the dislocation density changes during recrystallization will be much faster.

[3] After cold rolling, texture is {223}<110>. The orientation of these planes is closer to {211} leading to high intensity

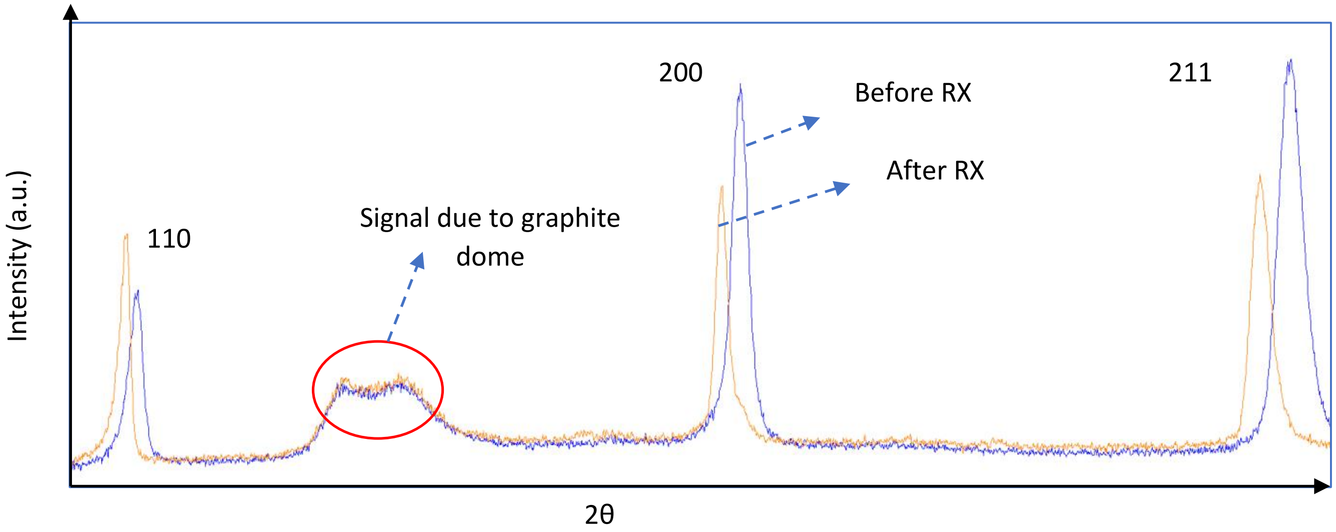

Figure 7 The XRD spectrum showing ferrite peaks of alloy 2A (0Si2Mn) after integration for the cases of before RX (at room temperature) and after RX (at 726°C) for alloy 2A heated at 0.1 K/s.

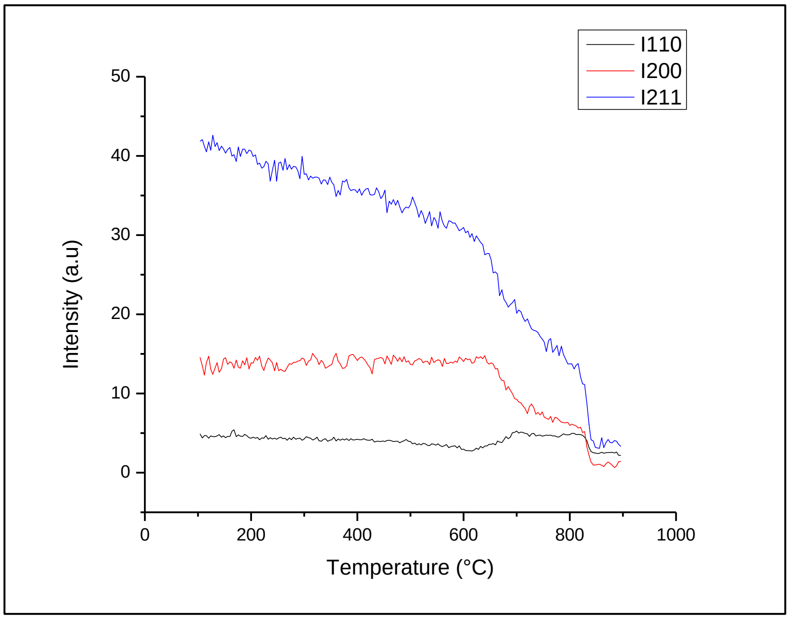

Figure 8 Intensity vs Temperature for ferrite peaks for alloy 2A (0Si2Mn) at 1 K/s.

To detect the recrystallization start and finish temperatures from the intensity plots in Figure 8, the derivative of these intensity plots has been used. The derivative plot along with an intensity plot is shown in Figure 9. The points at which derivative changes rapidly are considered as start and finish points (Figure 9), which are used for calculations of recrystallization volume fraction (RX_vol_frac). During the detection of these points, noise in the XRD data was also considered. When the value of the derivative dips significantly below the noise (fluctuation) level, then the corresponding point is considered as the recrystallization start point (see Figure 9). Similar procedure has been used for recrystallization finish point.

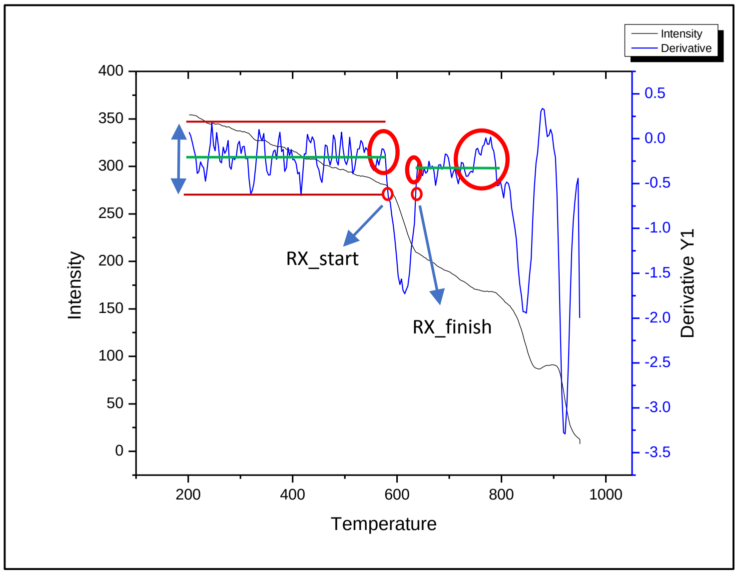

Figure 9 Intensity vs Temperature for 211 peaks of ferrite along with derivatives. Green line: average derivative values, Brown lines: depicting maximum and minimum fluctuations.

There is a change in the peak intensity due to temperature increase. This was corrected by linear fitting the data before the RX_{start} and after RX_{finish}. The slopes of these two linear fits were separately adjusted. The intensity points from recrystallization region were not changed. The corrected intensity is seen in Figure 10. After this step, the lever's rule was applied to calculate the recrystallized volume fraction between the RX_{start} and RX_{finish} points identified by the earlier analysis. The plot of RX_vol_frac vs Temperature is shown in Figure 11.

$$RX_{frac} = \frac{I_{TS} - I_T}{I_{TS} - I_{TF}} \times 100 \tag{14}$$

I_{TS} is the intensity at RX_start, I_T is the intensity at that particular temperature, I_{TF} is intensity at RX_finish.

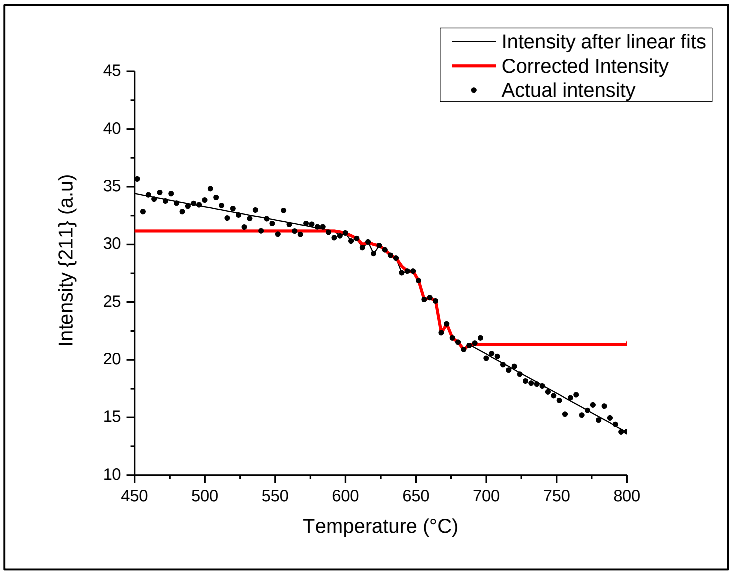

Figure 10 Temperature corrected intensity for Fe-211 peak of alloy 2A (0Si2Mn) at 0.1 K/s.

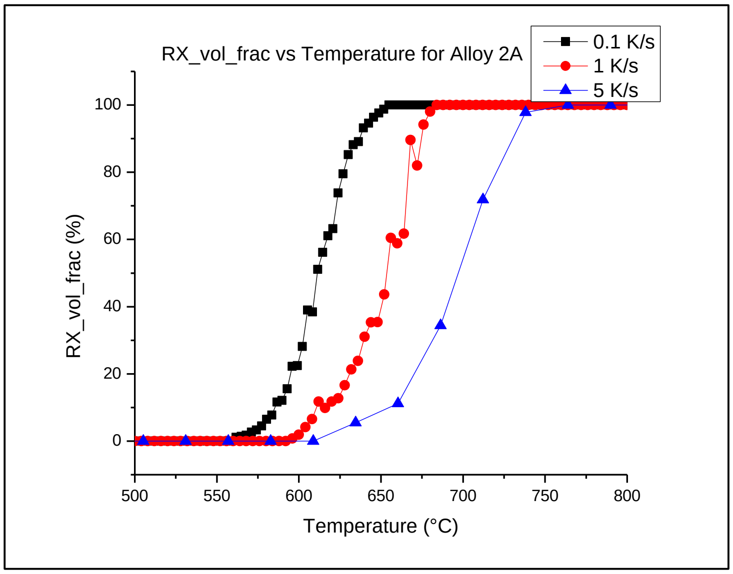

Figure 11 Recrystallized volume fraction vs Temperature for alloy 2A [0Si2Mn]

3.7 ERROR ANALYSIS OF THE X-RAY DIFFRACTION DATA

In the analysis of XRD data, there are multiple sources of errors. These affect both parameters that are being measured – the peak intensities and the measured temperatures.

Temperature error arises due to two factors – a) error due to thermocouple measurements b) difference in temperature between the thermocouple and the sample. The thermocouple used is of S-type. This thermocouple had a temperature accuracy of ±1.5°C. These errors were neglected. To reduce or eliminate the error due to temperature difference between the sample and the thermocouple, calibration was done as described in Section 3.5. Even then, the temperature measurement at the sample surface is not possible due to sealing of the sample area by graphite dome. Thus, it can be seen that determination of temperature error is a difficult task, and therefore, temperature interval for measurement is used as a parameter to describe the accuracy of the data. The larger the temperature interval, bigger the error will be. As the X-ray spectrum is continuously recorded over the whole temperature interval, there is an uncertainty about which temperature is leading to changes in the signal.

Most of the intensity data was smoothed using 'Savitzky Golay Smoothing' with polynomial 2nd order consisting of 10 points. In some cases, even after smoothing the data was quite noisy. This led to the temperature errors being higher than the ones calculated from temperature intervals. This is because, noisy data would lead to uncertainties in the values of the derivative, which increases the uncertainty in identifying the recrystallization temperatures. This is described in Figure 12. To make sure that both the errors are included, the errors are added up.

The errors in the intensity can be due to the efficiency of the detector, which is not possible to determine. The other source of errors in the peak intensity estimation is the Rietveld refinement. The Rietveld refinement gave errors in the intensity of less than 1% and were therefore neglected.

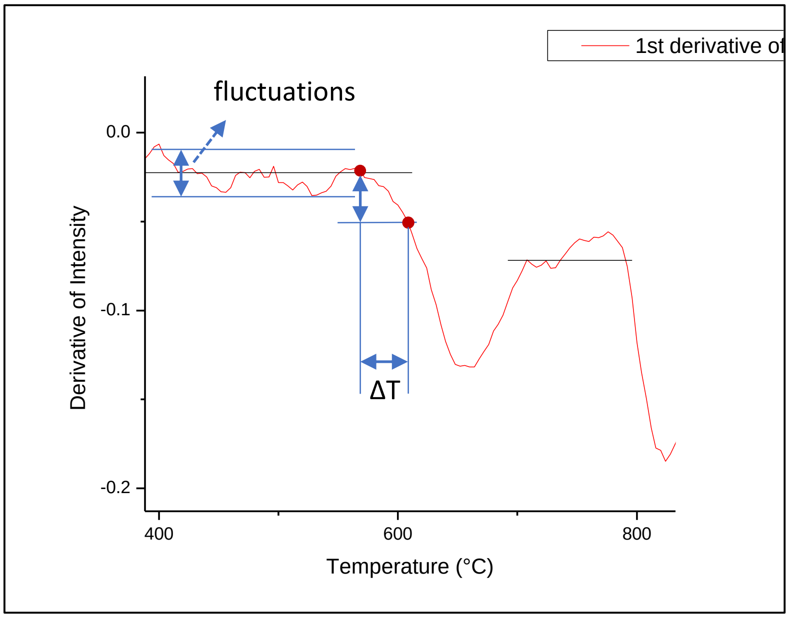

Figure 12 Showing the errors in temperature at a particular point due to noisiness in data for alloy 4A (1Si2Mn) at 5 K/s.

The linear fit is used during calculations for temperature corrections of intensities. This has some error associated with it. This error further propagates when the RX_vol_frac is calculated. This error can be calculated using the concept of propagation of errors.

If function is defined as f (x_1, x_2,… , x_n), then error in the function due to the errors in the variables x_1,x_2, …, is given by following equation:

$$s_f = \sqrt{\left(\frac{\partial f}{\partial x_1}\right)^2 s_{x_1}^2 + \left(\frac{\partial f}{\partial x_2}\right)^2 s_{x_2}^2 + \ldots + \left(\frac{\partial f}{\partial x_n}\right)^2 s_{x_n}^2} \tag{15}$$

where, s_f, s_{x1}, s_{x2}, s_{xn} are the standard deviations of the respective variables

RX_{frac} is calculated based on peak intensities according to equation (14).

So the error becomes,

$$s = \sqrt{\left[\frac{I_T - I_{TF}}{(I_{TS} - I_{TF})^2}\right]^2 s_{TS}^2 + \left[\frac{I_{TS} - I_T}{(I_{TS} - I_{TF})^2}\right]^2 s_{TF}^2} \tag{16}$$

3.7 MICROSTRUCTURE ANALYSIS

Microstructure analysis is very important as it can be alternative source for the parameters in the model fitting of the XRD data. The models used for curve fitting are described in Chapter 2. Therefore, during the microstructure analysis, focus is on the identification of recrystallized grains, determining the number of nuclei, determining the parameters of grain growth and the shape of the growing recrystallized grains.

3.7.1 SAMPLE PREPARATION

The samples for microstructure analysis were cut in the rolling direction (RD) – normal direction (ND) plane and transverse direction (TD) – normal direction (ND) plane. The cut surfaces near the centre of the specimen are considered for the microstructure analysis. The central part of the specimen was in direct contact with the heating element of the in-situ XRD and thus, it is closest to the actual temperature of the thermocouple. The surfaces used for microscopy analysis are described in Figure 13. The samples were mounted in conductive resin and then grinded with SiC papers from 800 grit size to 2000 grit size. Next, the samples were polished with cloth and 1µm diamond solution. As the microstructure analysis is being carried out using Backscattered Detector, the surface has to be free from any surface relief or scratches which can hamper the microstructure analysis of fine microstructures encountered in the cold rolled materials. Therefore, as a final step the samples were polished using colloidal silica (OPS) for approximately 5 minutes.

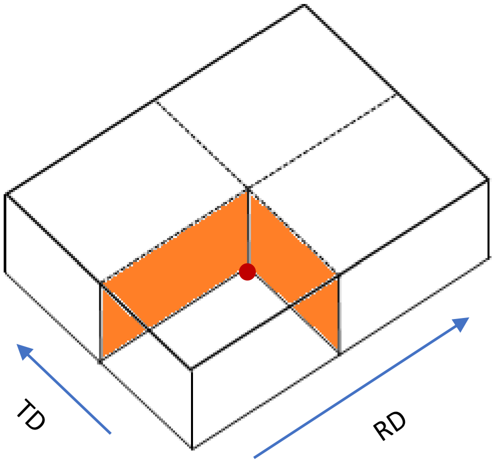

Figure 13 Showing the surfaces being used for microscopy analysis. Brown dot signifying the centre of the specimen which was in direct contact with the heating element

3.7.2 SETTINGS FOR SCANNING ELECTRON MICROSCOPY

As the cold rolled microstructure is fine grained, high resolution is required. Therefore, a JEOL JSM 6500F Scanning Electron Microscope (SEM) is used to capture the high resolution microstructure images. This microscope has a field emission gun, which has a very small electron beam size. The images were taken with Backscattered Electron detector (BED) which allows electron channelling contrast [56], which would help identify the different grains. As the material is cold rolled and then recrystallizing, there is orientation difference between adjacent grains. This orientation difference results in different crystallographic planes facing the electron beam for different grains. Different crystallographic planes would result in difference in the yield of backscattered electrons giving different grey levels for different grains, as can be seen in Figure 14. The images are being observed at the accelerating voltage of 20kV and probe current of 65pA. Since the microstructure images are used for quantitative analysis, it is very important that the area is representative of the whole material and not just some local phenomena. From the study of Davut et al. [57] it was seen that for EBSD scans minimum of 30000 points and minimum scan area of 0.275 mm^2 is a good representative area. The amount of grains covered in this area are approximately 2500 grains. To estimate the required area to be scanned, the fully recrystallized microstructure is used, as the microstructure is more homogeneous. The average grain size in fully recrystallized microstructure is quite large in comparison to non-recrystallized samples. Thus, corresponding area in the part-recrystallized microstructure would amount to much higher number of grains. Therefore, an area that would give 1000 grains in fully recrystallized microstructure is assumed to be a good representative area. For the case of 100% recrystallized microstructures, each image is covering an area of 120 X 100 μm^2, which contains approximately 200 ferrite grains. Therefore, to be able to get an area that would cover 1000 grains, 5 SEM images would be required. Thus, 5 images for each type of sample have been used together to do quantitative analysis.

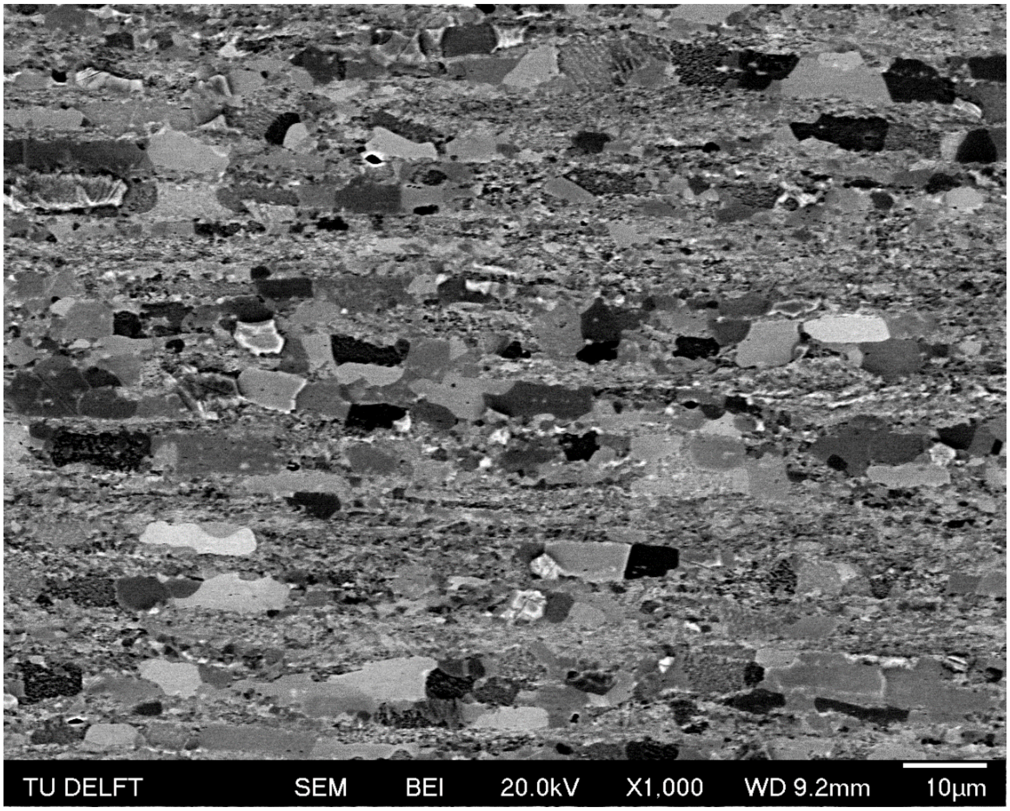

Figure 14 The Backscatter electron image for 50% recrystallized microstructure for alloy 2B, showing different grains with different grey levels due to electron channelling contrast.

3.7.3 IDENTIFICATION OF RECRYSTALLIZED GRAINS IN MICROSTRUCTURE

The standard technique to identify the recrystallized grains in the microstructures is (EBSD). This technique is quite time consuming and thus, not very convenient for analysing multiple samples from 7 alloys. Therefore, a method using electron channelling contrast effect to detect recrystallized grains has been developed. The uniformity of the grey level for the grains is used as a criterion to identify the recrystallized grains. The recrystallized grains, owing to a crystal structure with no defects, have a quite uniform backscatter electron yield across the whole grain. The recovering and deformed grains have defects in their crystal structure, leading to non-uniformity in the backscattered electron yield across the grain. This criterion of grey level has been explained in Figure 15. To validate this method, some EBSD scans were also performed to check whether detected recrystallized grains are really the recrystallized grains or not. The EBSD scans confirmed that the identified recrystallized grains are correct. The quantification from EBSD and SEM analysis have been compared in Appendix D. The grains smaller than 1-2 µm diameter were difficult to classify and thus, they were left out of SEM analysis.

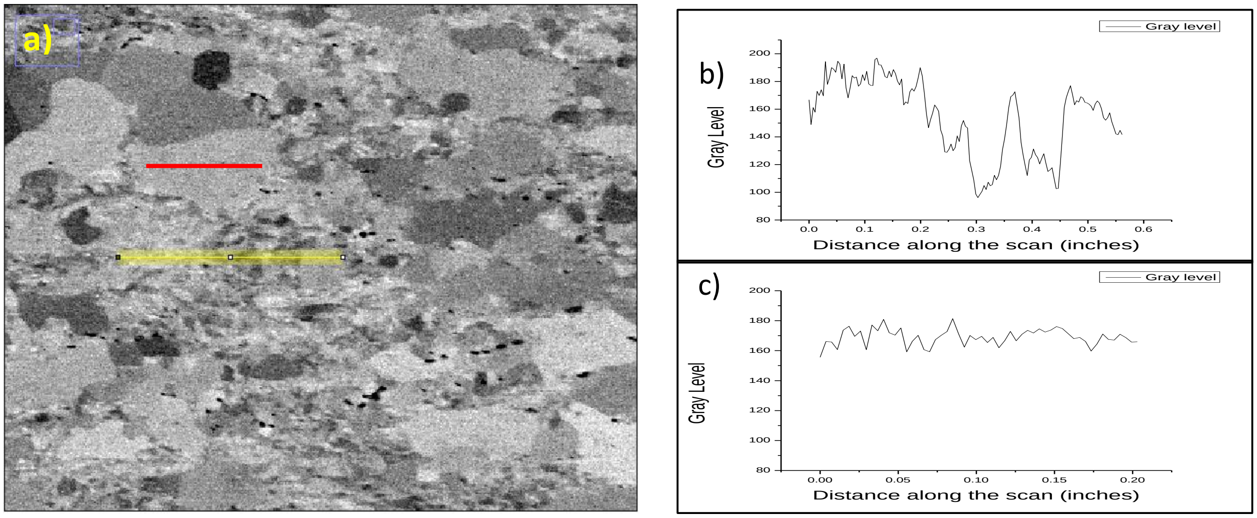

Figure 15 Showing the grey level variations in deformed and recrystallized regions a) showing the scan positions in microstructure b) grey level variation in the deformed region (yellow line) c) grey level scan in recrystallized region (red line). The red line represents recrystallized grain and the yellow line represents deformed region.

3.7.4 GRAIN SIZE ANALYSIS AND QUANTIFICATION

The values such as the aspect ratio of the grains, grain sizes and number of grains can be obtained from grain size analysis software. In this work, the grain analysis is performed using Leica Grain Expert v4.9. The software is able to detect grains based on changes in the grey levels. Although the software employs automated algorithms for detection some manual corrections are required. The software used ASTM E112 Intercept procedure to get the grain sizes of the detected grains.

From the grain size data obtained from the software, the recrystallized grains were filtered based on criteria of grain sizes and positions. First criterion is the grain size. In the cold deformed microstructure, the deformed grains (or sub-grains) are very small and difficult to detect even with the high resolution images. The ferrite grains in deformed parts of the microstructure are of the size 1-2 µm, corresponding to grain area of 3-4 µm^2. The grains equal to or smaller than this size are not considered. The other filtering criteria was based on the grey level analysis mentioned in the previous section. This step removed some of the misrepresented grains in the deformed regions.

The results of microscopy analysis are used to confirm whether the values of the parameters derived from the model fitting are meaningful and to correlate these kinetic parameters to the microstructure evolution.

The number of nuclei and growth rate of recrystallized grains can approximately correlate to the rate constant (or pre-exponential factor), as described in Section 2.4.1 and Section 2.4.2. Therefore, the number of nuclei is counted from the results of the grain analysis, after applying the two filtering criteria mentioned. The samples of 50% recrystallization have been used to calculate the number of nuclei. The samples of 10% recrystallization were not used to count the recrystallized grains, because some very small nuclei remained undetected. The other aspect to be confirmed is to see whether the nucleation is site-saturation or continuous nucleation. This can be confirmed by comparing the number of recrystallized grains in 10 and 50% recrystallized samples, through grain size distribution plots. If the fraction of recrystallized grains below the size of 5 μm^2 in 50% recrystallized material is lesser than the fraction of recrystallized grains below 5 μm^2 in 10% recrystallized material, then it can be considered as site-saturation. Increase in fraction of grains below 5μm^2, can point to continuous or decreasing nucleation rate. Information about occurrence of site-saturation or continuous nucleation can be used to deduce the Avrami exponent.

Growth rate is determined by considering the change in average grain sizes over a given temperature range during recrystallization. The average grain size is fitted to the non-isothermal growth equation which would give the value of the growth rate. The non-isothermal grain growth equation has been explained in detail in Section 2.4.2 and Appendix B.

The aspect ratio of the grains would give idea about the dimensions of the growth. The number of dimensions into which the recrystallized grains are growing along with the information of site-saturated or continuous nucleation can help in deciding what can be the Avrami exponent, which can be used as an input parameter. The change in the Avrami exponent with the dimensionality of growth and type of nucleation is given in Table 4. When the aspect ratio is greater than 1 and is increasing with progress in recrystallization in the rolling as well as the transverse direction, then it has been concluded that the growth is 2-dimensional.

Table 4 Values of Avrami exponent (m+1) for various cases

Growth Dimensionality	Site-saturated nucleation	Continuous nucleation
3-D	3	4
2-D	2	3
1-D	1	2

3.8 ELEMENTAL DISTRIBUTION USING EDS

As the thesis aims to study the effect of alloying elements, it is important to know the distribution of alloying elements in the microstructure. This distribution can affect the nucleation and growth of recrystallized grains. Moreover, as seen in Figure 16, there is banding in the microstructure. It indicates presence of elemental segregation as well. This elemental segregation might lead to restriction of nucleation and growth of recrystallized grains. Elemental segregation can also lead to inhomogeneous nucleation and growth. Thus, the relation between occurrence of recrystallized nuclei and presence of alloying elements at these sites is important. Also, in some regions the grain growth is faster than other regions, this is also related to the distribution of the alloying elements and must be investigated. The 10% recrystallized samples were studied using Energy Dispersive Spectroscopy with SEM (SEM-EDS), to understand the effect of distribution of alloying elements on nucleation. To relate the effect of distribution of alloying elements on the growth, the 50% recrystallized samples were also studied by EDS. To limit the amount of EDS analysis and to get the clear picture of effect of alloying elements for whole range of alloys following sets of alloys were investigated – High Mn Low Si, High Mn High Si and Low Mn High Si alloys were chosen. These alloys are 2A (0Si2Mn), 5A (1.5Si2Mn) and (1.5Si0Mn) respectively.

The grey scale image was acquired in the backscattered electron mode with accelerating voltage of 15kV at a magnification of 1200X. The EDS maps were acquired with a resolution of 512 X 384 pixels, with a pixel size of 0.20 µm. The microscope used for the analyses is Jeol7001 equipped with two Silicon Drift EDS Detectors (SDD). Afterwards the spectra are analysed with Thermo Scientific software NSS Noran v4.1.

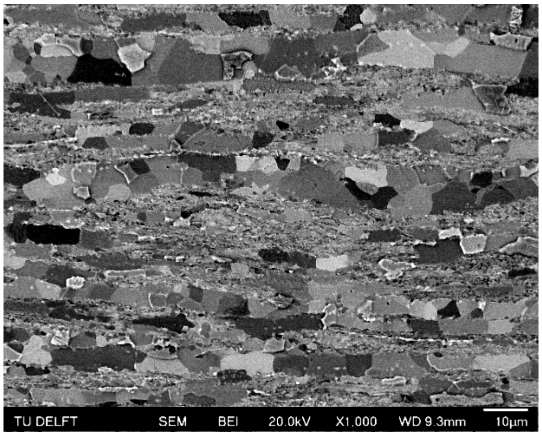

Figure 16 Microstructure showing the banding of components in Alloy 2A at 50% recrystallization

4. RESULTS AND DISCUSSIONS

4.1 RESULTS FROM XRD ANALYSIS

The earlier mentioned analysis of the XRD data gives the following experimental recrystallization kinetics curve, as shown in Figure 17. This curve has similar shape for all alloys, with difference being visible in form of changes in recrystallization start (RX_{start}) and recrystallization finish (RX_{finish}) temperatures. The rate of recrystallization is also changing for the alloys as seen in Figure 18.

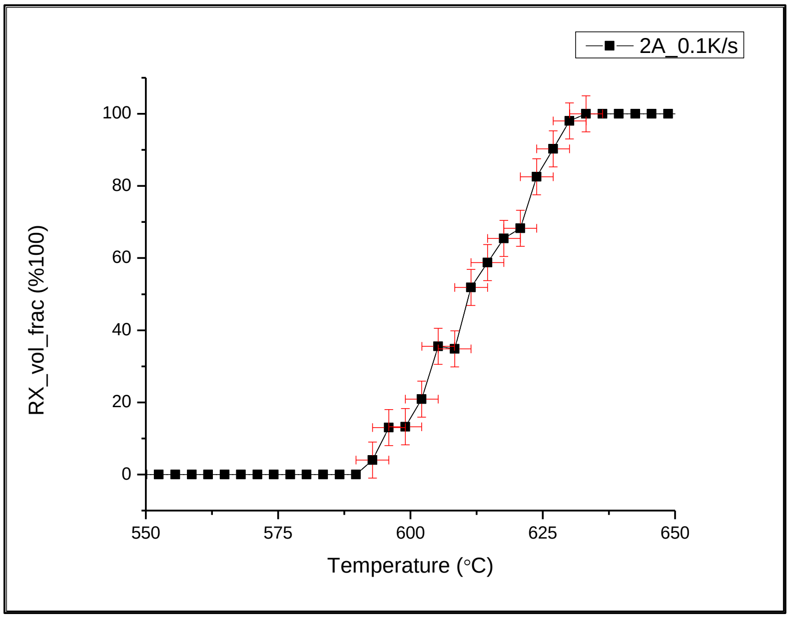

Figure 17 Graph showing the progress of recrystallization for alloy 2A (0Si2Mn) at 0.1K/s heating rate based on XRD data.

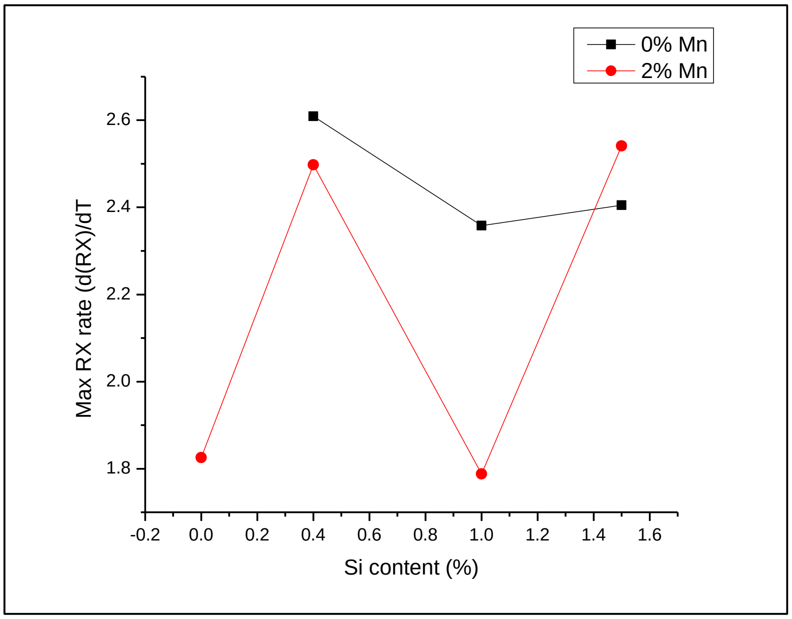

Figure 18 Showing the variation in maximum recrystallization rate with alloying at 1 K/s.

The shape of all the recrystallization curves being the same, means that the basic mechanisms of the process are the same. The variation in the rate of the recrystallization, means that the alloying is changing the progress of the whole process. In case of recrystallization, these mechanisms are nucleation and growth. Addition of Mn is leading to a reduction in the rate of recrystallization. In the low Mn alloys, the recrystallization rate is decreasing with addition of Si content. Whereas, in the high Mn alloys, there is no distinct correlation between addition of Si and the recrystallization rate. This indicates that the nucleation and growth processes are being affected by the variations in alloying. As seen in section 2.4.1, this recrystallization rate is represented by the parameter, rate constant k_o, in the Avrami model. Thus, model fitting should also give idea about the rate of recrystallization.

These experimental recrystallization curves also change when the heating rates are changing. Higher heating rates increase the RX_{start} and RX_{finish} temperatures. This can be seen in Figure 19.

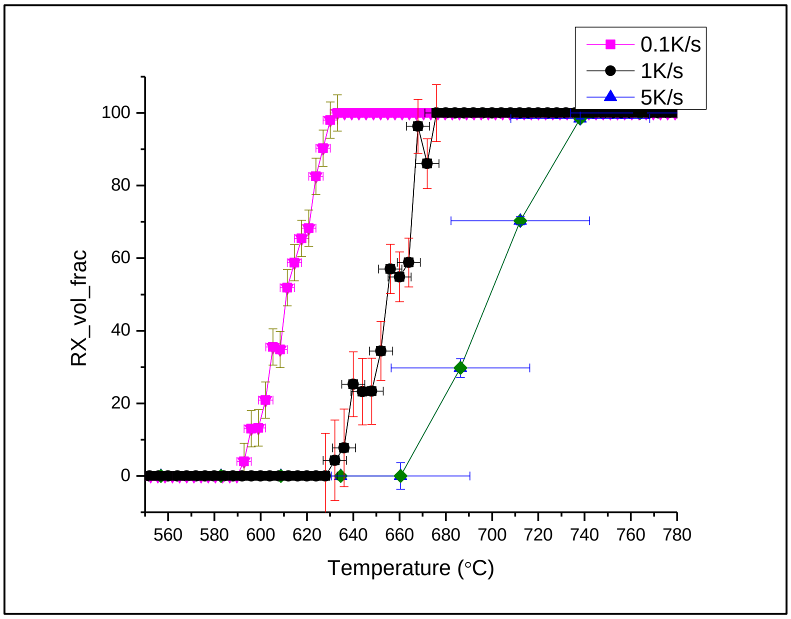

Figure 19 Effect of heating rate on recrystallization kinetics for alloy 2A (0Si2Mn)

CHANGES IN RECRYSTALLIZATION TEMPERATURES

The recrystallization start temperatures are increasing with heating rates, which is expected. This increase in the recrystallization start temperatures is seen in Figure 20 for alloys 5A (1.5Si2Mn) and 7B (1.5Si0Mn). Such an increase in recrystallization start temperature is seen for steels with High Mn as well as Low Mn content. This behaviour was seen for all the alloys. Thus, this effect can be attributed to the kinetic effects of the process, because recrystallization is a thermally activated process. For higher heating rates, the underlying processes would finish in similar times, but they take place at higher temperatures. As the RX_{start} temperatures have increased with heating rates, the RX_{finish} temperatures have also increased.

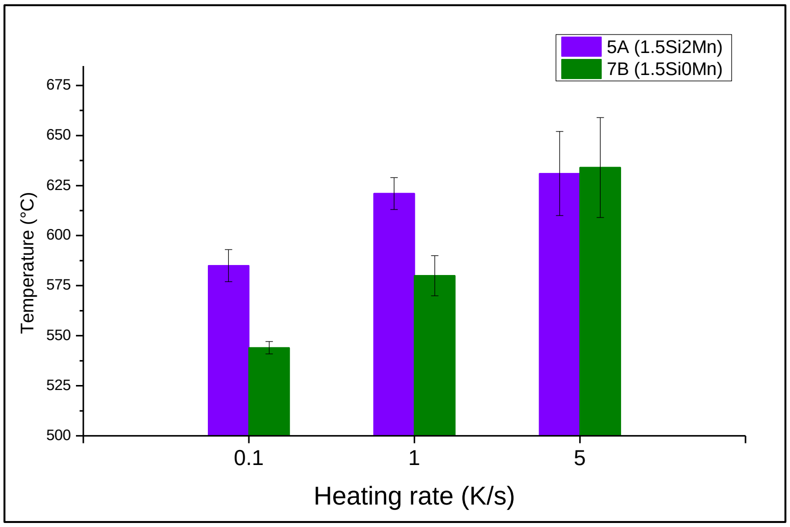

Figure 20 Change in recrystallization start temperatures with heating rates.

Along with heating rates, the other factor that is affecting the $RX_{start\ and}$ RX_{finish} temperatures is the alloying. This can be seen in Figure 21, Figure 22 and Figure 23. RX_{start} temperatures are related to the event of nucleation and RX_{finish} also incorporates the effects due to grain growth. Therefore, changes in these temperatures with alloying, suggest that, alloying elements are having effects on these processes.

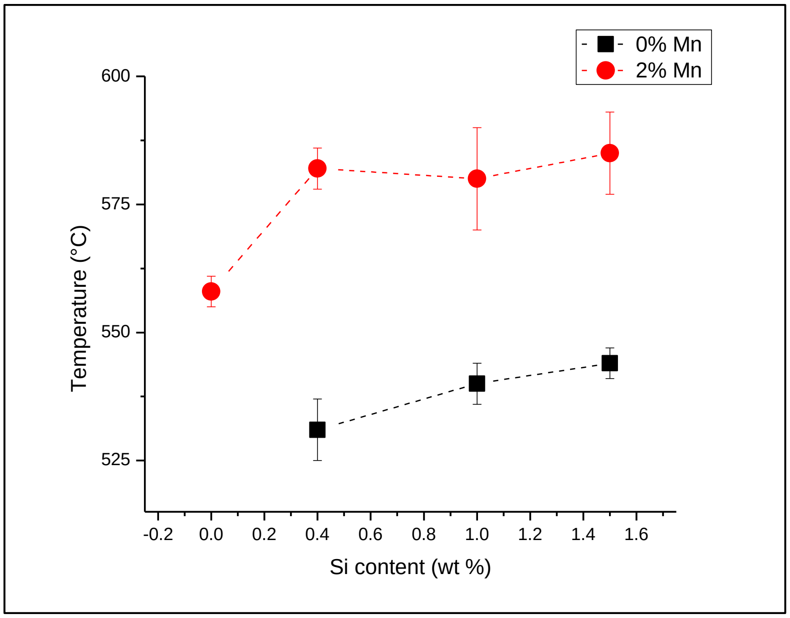

Figure 21 Change of recrystallization start temperatures for various alloys at 0.1 K/s

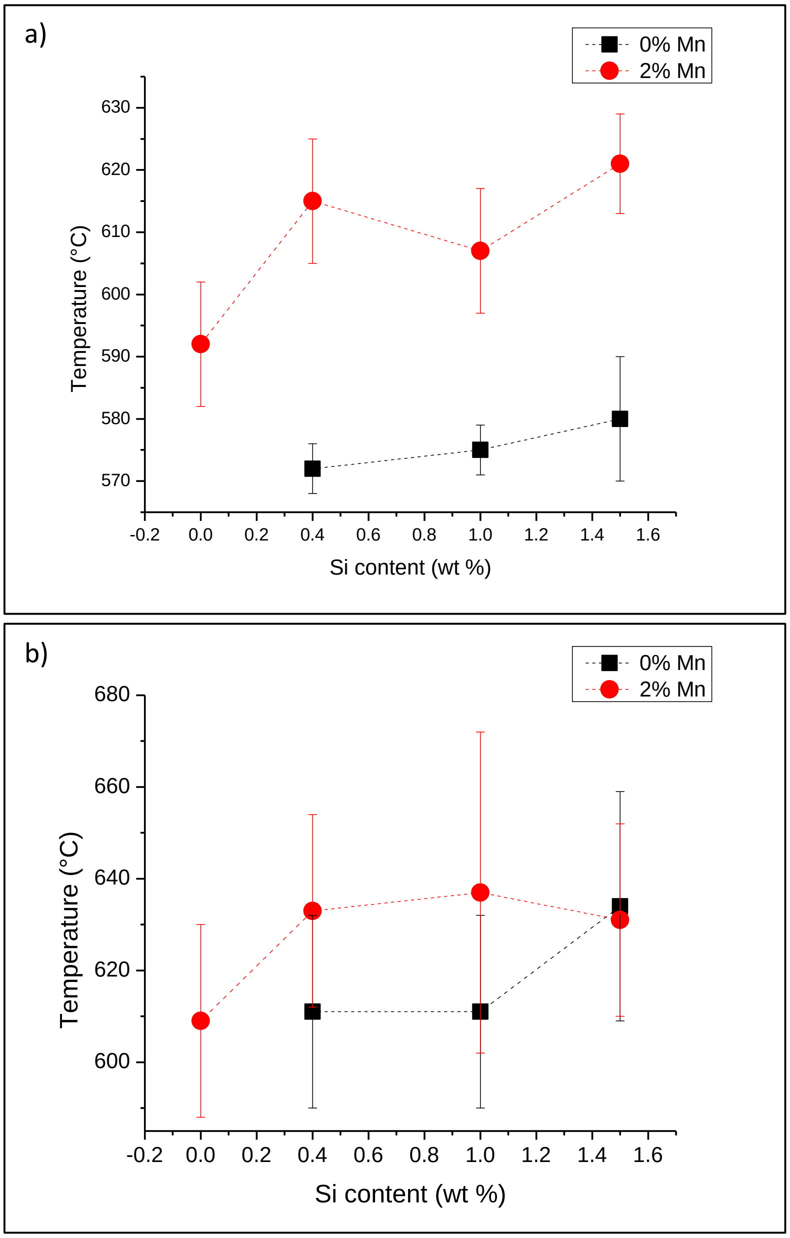

Figure 22 Change in recrystallization start temperatures with alloying for a) 1K/s b) 5K/s

From the Figure 21 and Figure 22, it is clearly seen that addition of Mn raises the RX_{start} temperature significantly. In the low Mn alloys, the addition of Si has slowly increased the RX_{start} temperatures. This increase is much lower than the increase caused by Mn addition. This supports the hypothesis that Mn creates intense solute drag effect in ferrite [4]. This has been observed in the result of rates of recrystallization. From the results, it can be said that Si in low Mn alloys is creating a small solute drag effect. In presence of Mn, a small addition of Si leads to an increase in RX_{start} temperatures. This is seen when Si increases from 0 wt. % to 0.4 wt. %. This can be expected from the solute drag theory, as described by equation (11). But, subsequent addition of Si in high Mn alloys doesn't lead to a consistent rise in RX_{start} temperatures. This is especially evident for Si content between 0.4 wt. % to 1.5 wt. %. This is contrary to the solute drag theory described. This behaviour is also evident, when the maximum recrystallization rates are considered, as seen in Figure 18. Such a behaviour points to multiple causes. According to the solute drag theory, there would be an increase in solute drag effect. Some other effects due to nucleation might lead to changes in the RX_{start} temperatures. Moreover, some special interaction between Si and Mn might be leading to a different solute drag behaviour during grain growth at these concentrations. The other possibility could be, that there are changes in the microstructure of high Mn alloys due to addition of higher amount of Si. At even higher heating rates, the differences in the RX_{start} temperatures are not very significant. This could be possible, because of the increased uncertainty of the measurements at high heating rates. To understand the behaviour at higher heating rates better, very fast X-ray recording and very powerful X-ray source would be required.

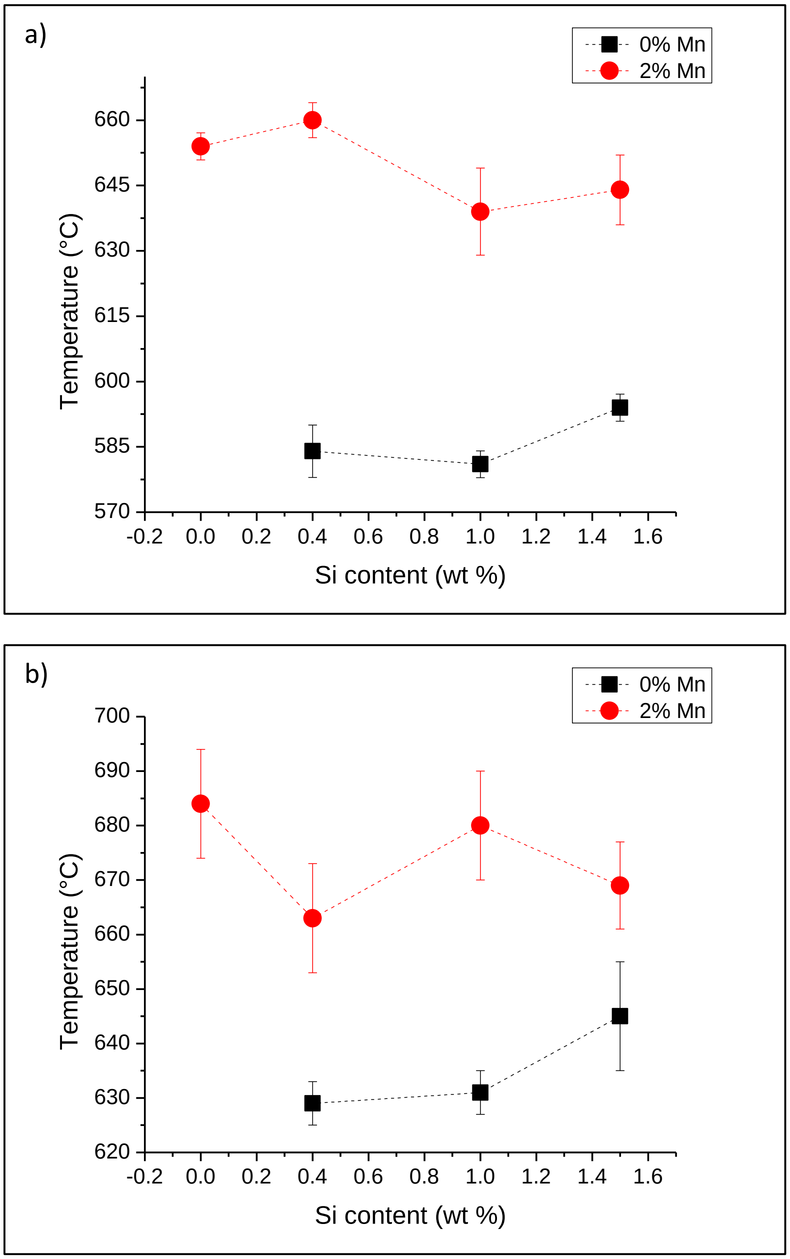

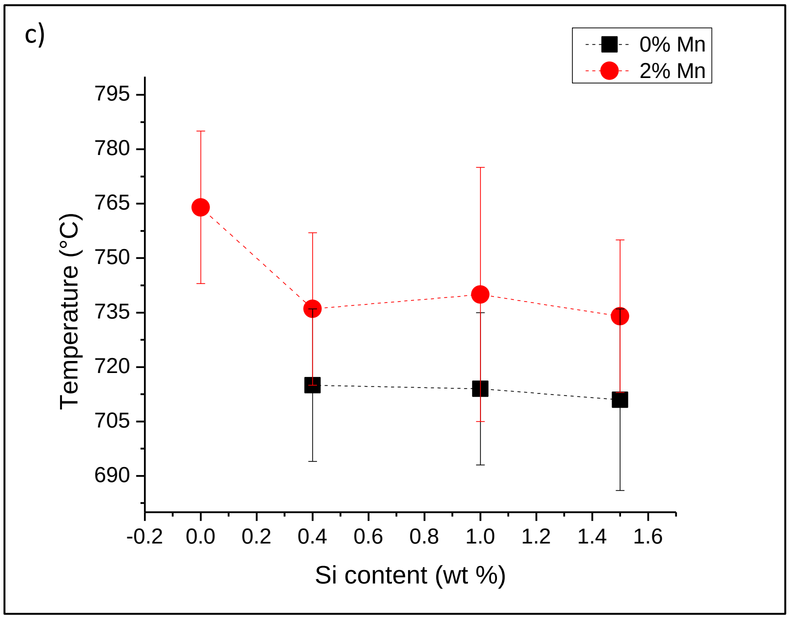

Figure 23 Change in recrystallization finish temperatures with alloying a) 0.1 K/s b) 1 K/s c) 5 K/s

The trends of RX_{finish} temperatures (seen in Figure 23) do not mimic the trends of the RX_{start} temperatures. This might be due to an additional influence of growth of recrystallized grains. Therefore, the changes in RX_{finish} temperatures could be correlated to changes in number of nuclei, as well as the parameters of growth such as growth rates and directions available for the growth. The effect of Mn on the growth stage is very clear from Figure 23. Addition of Si in low Mn alloys is also increasing the RX-finish temperature slowly. Thus, a small solute drag effect can be expected from Si. Again, as seen earlier, in the region of Si content from 0.4 wt. % to 1.5 wt. % in presence of 2 wt. % Mn, the effect of alloying elements is not very clear.

To get a clear picture of the effect of relative amounts of Si, Mn on the recrystallization temperatures, the recrystallization temperatures with respect to the Si/Mn ratios are plotted in Figure 24 and Figure 25.

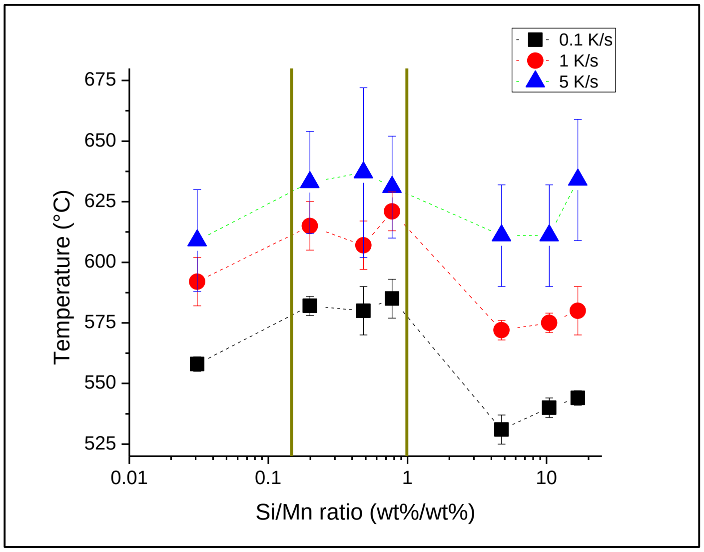

Figure 24 Variation of recrystallization start temperature with Si/Mn ratio

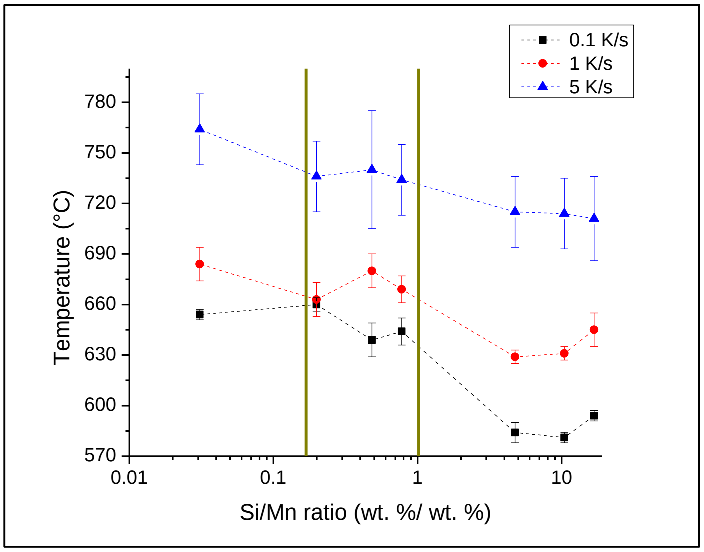

Figure 25 Variation in recrystallization finish temperatures with Si/Mn ratio

Again, as seen earlier, the higher Mn content leads to rise in the recrystallization temperatures. Also, at very high Si contents, there is a rise in recrystallization temperatures. These trends change between the Si/Mn ratios of 0.15 – 1.0. In high Si or high Mn regions, the Si and Mn are unaffected by each other and therefore, imparting their individual characteristics. But in the regions with Si/Mn ratios of 0.15 – 1.0, the relative concentrations of Si and Mn are such that, they start interacting with each other and lead to a different behaviour. This behaviour is quite unpredictable.

4.2 MICROSCOPY ANALYSIS

The parameters obtained from quantitative microstructure analysis are: number of nuclei, grains aspect ratios, grain sizes distribution and average grain sizes of recrystallized grains. Some qualitative observations are made regarding such parameters as: nucleation sites and distribution of nuclei. All the microscopy work has been carried out on materials which have undergone continuous heating at the heating rate of 1 K/s.

TYPICAL MICROSTRUCTURES

The microstructure evolution for Low Si High Mn, High Si High Mn and High Si Low Mn is seen in Figure 26, Figure 27 and Figure 28.

From the microstructure images, it can be seen that for alloys with high Mn the banding of pearlite is much more significant leading to more elongated grains in the final recrystallized microstructure. For alloys with high Si and low Mn, the banding is of lesser extent. Thus, the elongation of grains is also lesser. The amount of pearlite banding could be correlated to the amount of pearlite in the microstructure. The amount of pearlite is given in Table 6. It can be seen that Alloy 5A (1.5Si2Mn) has highest pearlite and therefore, highest amount of pearlite banding is seen. High Si alloys, such as Alloy 7B (1.5Si0Mn) have the least pearlite content. This leads to lesser pearlite banding. This lesser pearlite banding is also visible in the microstructure in Figure 28 as the recrystallized grains are more equiaxed.

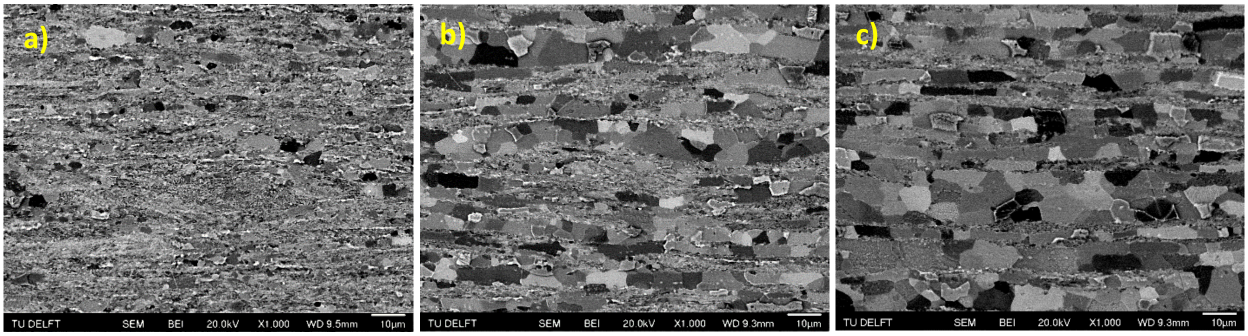

Figure 26 The microstructure evolution of Alloy 2A [0Si2Mn] a)10% RX b) 50%RX c) 100% RX

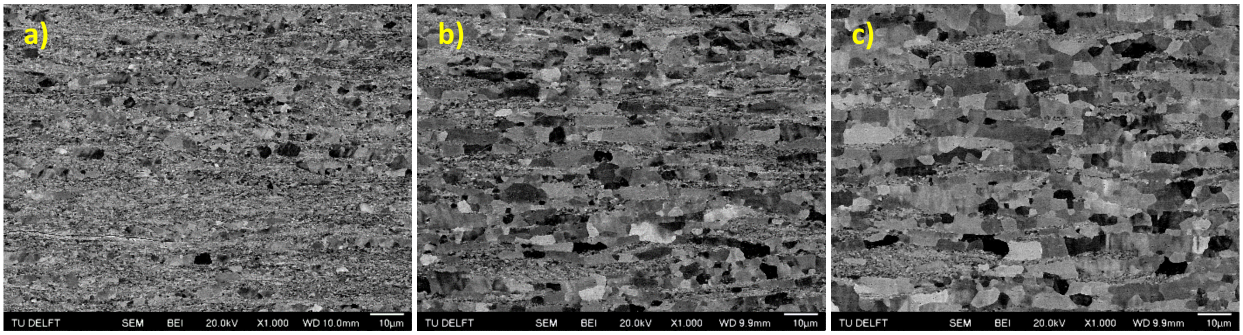

Figure 27 The microstructure evolution of Alloy 5A [1.5Si2Mn] a)10% RX b) 50%RX c) 100% RX

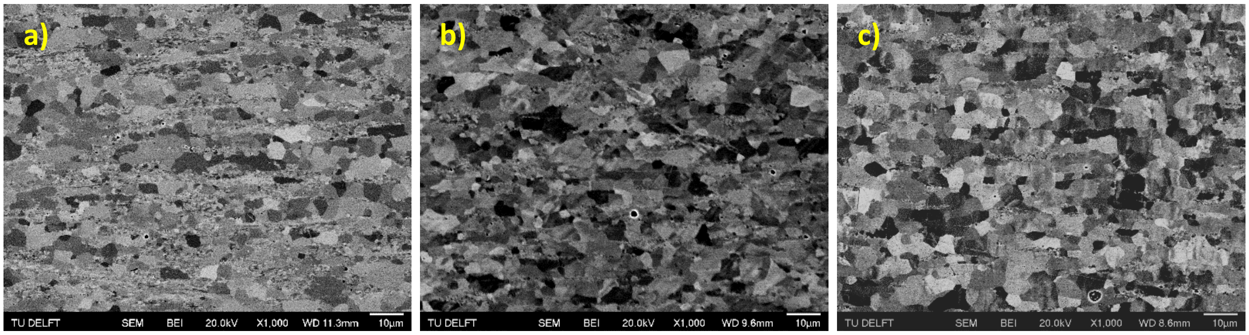

Figure 28 The microstructure evolution of Alloy 7B [1.5Si0Mn] a)35% RX b) 80%RX c) 100% RX

GRAIN SIZE DISTRIBUTION

Grain size distribution plots help in characterizing the grain size distribution of recrystallized grains. It can help in determining whether the nucleation is site-saturation or not. The typical grain size distribution for the case of site-saturation is of the form shown in Figure 29. The grain size distribution shows that the amount of very small grains is decreasing with progress of recrystallization. The amount of larger grains is increasing. Then it could be assumed that, no new grains have nucleated, thus, resulting in decrease of amount of small grains. Most of the alloys have grain size distribution of this form (Appendix E). Thus, it can be concluded that in case of recrystallization the nucleation is mostly site-saturation.

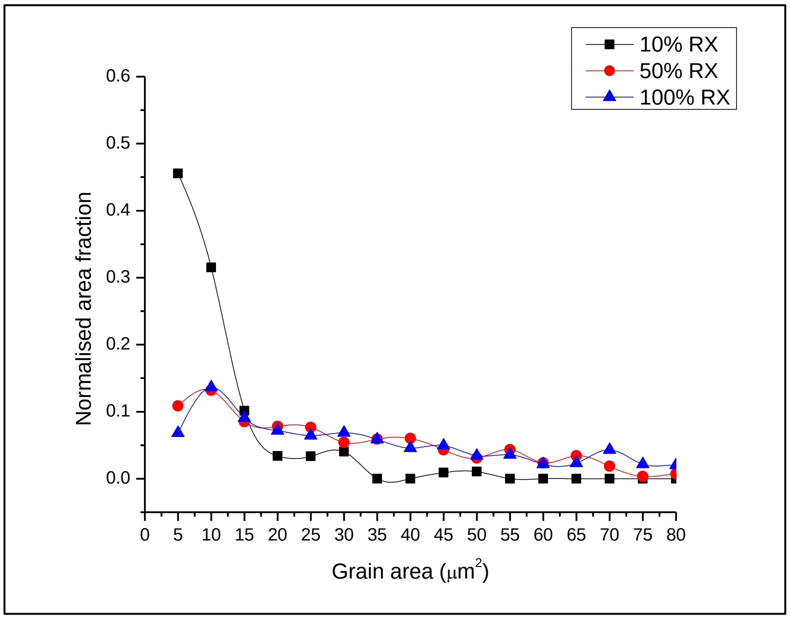

Figure 29 Grain size distribution for alloy 2A annealed at 1 K/s

The grain size distribution might give an impression, that the nucleation case is of site-saturation. Due to the inaccuracies of the experimental techniques it is also possible that there are some new grains nucleating. As these new grains nucleate, a larger number of 'older' grains might grow. Such a situation would again show the grain size distribution as shown above. Therefore, during the model fitting operation, the Avrami exponent was allowed to change between these two conditions. In most of the cases, the curve fitting was best achieved with the conditions for site-saturation. The correlation between Avrami exponent and the nucleation case is highlighted in Table 5.

Table 5 Values of possible Avrami exponents for different cases of nucleation

Growth dimensionality	Site saturation	Constant nucleation rate
3D	3	4
2D	2	3
1D	1	2

NUMBER OF NUCLEI

As shown earlier, due to site-saturation, the number of nuclei will remain constant or decrease with time. Nucleation can be best observed at the earlier stages of recrystallization. But, due to the resolution of the techniques being used, it is quite possible that very small nuclei might remain undetected. Therefore, the number of recrystallized grains were counted in the 50% RX samples. This number can quantify the amount of nucleation. The variation with alloying is shown in Figure 30.

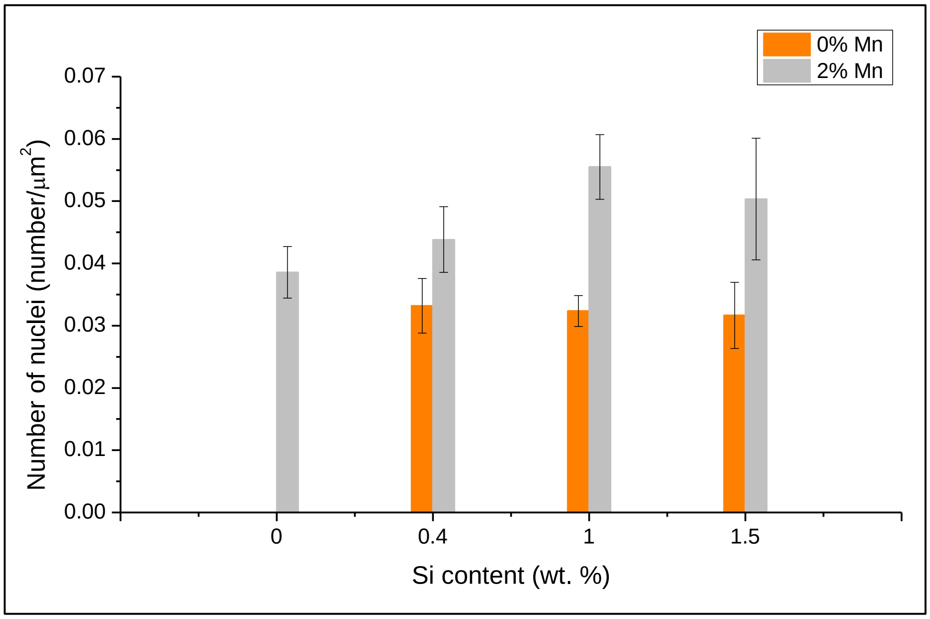

Figure 30 Variation in number of nuclei with alloying for 50% RX samples annealed at 1 K/s

The addition of Mn is increasing the amount of nucleation sites. This might be related to the amount of pearlite content. The alloys with higher Mn content have higher pearlite content. Higher pearlite content would mean that the interface area between the deformed pearlite and ferrite is higher, leading to more possible nucleation sites. Some alloys with similar pearlite content are also having some difference in nucleation rates. This can be because of the difference in the distribution of pearlite. Addition of Si has not shown any major effect on the nucleation in the low Mn alloys. This is because these alloys have the same pearlite content as seen in Table 6. Addition of Si to high Mn steels has led to a slight increase in the nucleation rates.

Table 6 Pearlite content for the alloys

Alloy	Pearlite (%)	Standard error (%)
2A (0Si2Mn)	34	2
2B (0.4Si2Mn)	32	4
4A (1Si2Mn)	40	2
5A (1.5Si2Mn)	41	3
6A (0.4Si0Mn)	20	2
7A (1Si0Mn)	20	3
7B (1.5Si0Mn)	18	2

ASPECT RATIOS

The change in aspect ratios with alloying is shown in Figure 31 and Figure 32. In Figure 31, the difference is seen in the high Mn and low Mn alloys with respect to aspect ratios. The high Mn alloys have a higher aspect ratio. This is because of higher amount of pearlite banding present in high Mn alloys. Thus, higher pearlite content has led to higher pearlite banding resulting in more elongated grains. In the TD direction, the difference between the aspect ratios for various alloys is not as big. But, in both the directions, the aspect ratio is either increasing or remaining constant with the progress of recrystallization. This proves that the growth of recrystallized grains is 2-dimensional.

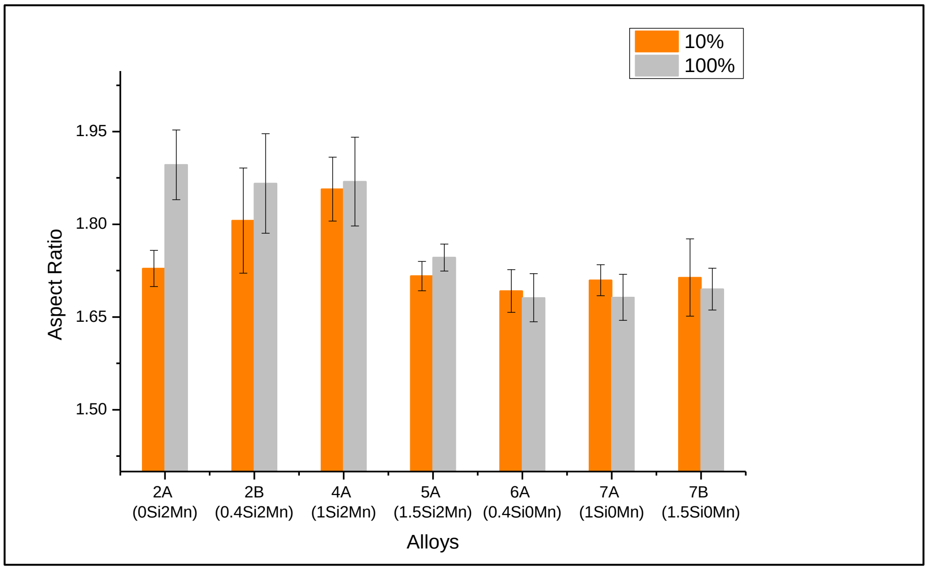

Figure 31 Aspect ratios for RD direction compared for 10% RX and 100% RX conditions.

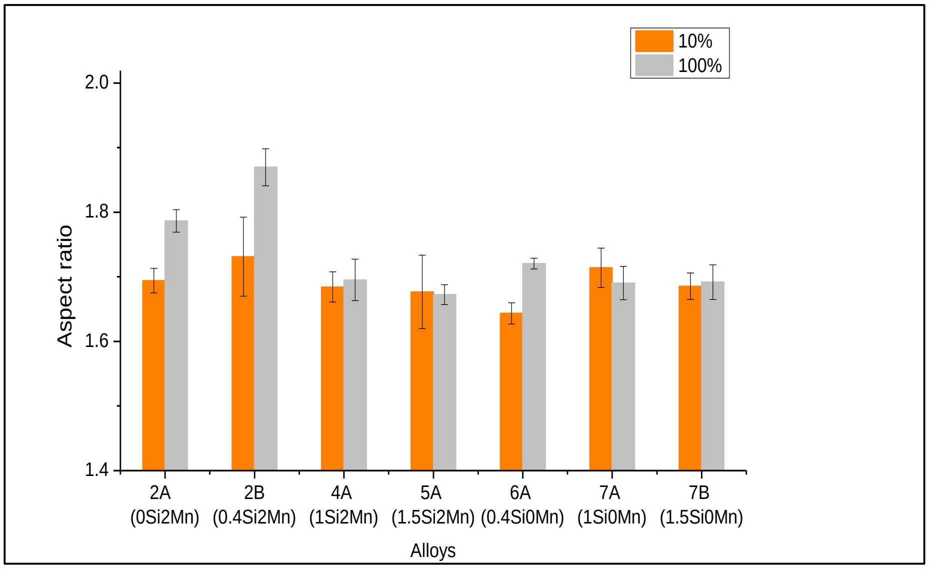

Figure 32 Aspect ratios for TD direction compared for 10% RX and 100% RX conditions.

4.3 NUCLEATION SITES AND ELEMENTAL DISTRIBUTION

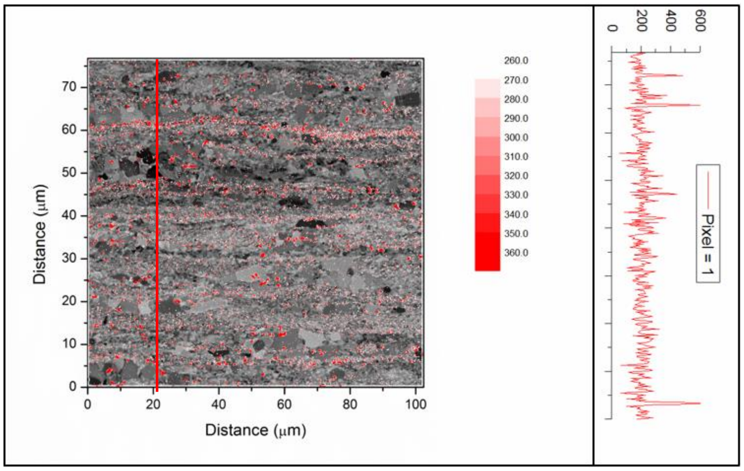

Figure 33 EDS map of Mn and the BSE Image for Alloy 2A (0Si2Mn) for 10% RX samples

In Figure 33, most of the nuclei are concentrated in the regions with low Mn content. It is seen that the nuclei originate at the boundary between high and low Mn regions. Higher Mn is generally found in pearlite areas, therefore, this shows recrystallization nuclei are nucleating at boundary between deformed pearlite and ferrite. Moreover, the nuclei have grown into low Mn regions. This can be because of pearlite obstructing the growth. The other possibility is that the Mn segregated in ferrite could also prevent the growth of these grains. The figure also shows a plot of Mn across the y-axis. It is seen that Mn is micro-segregated. The variation in Mn content is also seen inside the ferrite grains. There are some recrystallized grains which have not nucleated at the deformed pearlite-ferrite interface. It might be possible that local low Mn concentration might have led to nucleation of these new nuclei. Therefore, it can be said that pearlite affects the number of nucleation sites, but number of nucleation sites is also affected by local changes in Mn concentrations. To see the effect of Mn on growth, see Figure 34

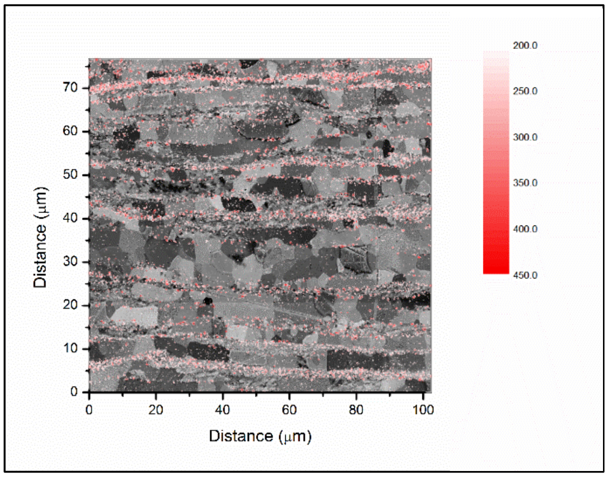

Figure 34 EDS map of Mn and corresponding BSE Image for Alloy 2A (0Si2Mn) for 50% RX sample

It is evident, that the recrystallizing grains tend to stop growing when they encounter the region with higher Mn content. Thus, it can be seen that Mn is affecting the growth of the recrystallizing grains to a great extent. The ability of Mn to stop the growth, comes from solute drag effect. The EDS results tend to support the observation of increase in recrystallization temperature due to Mn (Figure 21 and Figure 22).

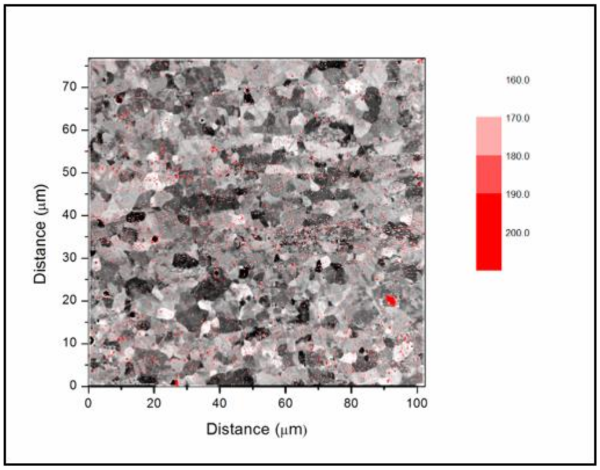

Figure 35 EDS map of Si and corresponding BSE Image for Alloy 7B (1.5Si0Mn)

In alloy 7B [1.5Si0Mn], the banding of Si is seen. The banding of Si is not as significant as that of Mn. The increase in concentration is 1.5 times. Moreover, the Si banding has not significantly affected the nucleation and growth of the grains. The recrystallized grains have grown everywhere. As the growth is not significantly affected in high Si regions, it can be said that the solute drag of Si alone is not very strong, which is supported by the data seen in Figure 21 and Figure 22.

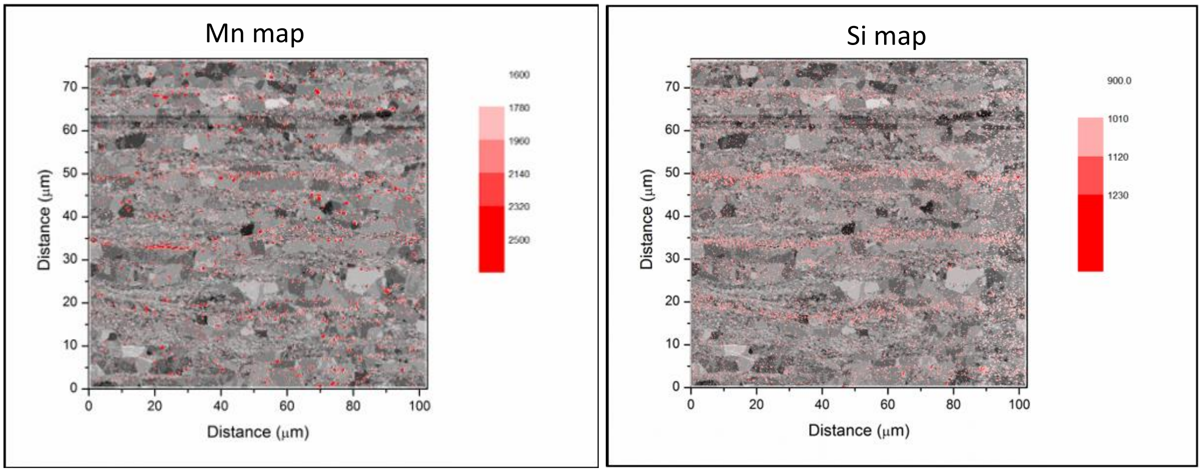

Figure 36 EDS map of Mn and corresponding BSE Image for Alloy 5A (1.5Si2Mn) at 50% RX.

Alloys with high Si and Mn, such as alloy 5A (1.5Si2Mn), show significant banding. In these alloys, the Si and Mn tend to segregate in similar regions. This is quite different from low Mn alloys, alloy 7B (1.5Si0Mn). In low Mn alloys, the Si banding is not very significant. But, in alloy 5A, it has become significant, which can be a consequence of presence of Mn. This could be attributed to co-segregation effect of Mn and Si [33]. As Si and Mn segregate in similar regions, there is a possibility of interactions between these solute atoms. These interactions might be dependent on the composition, leading to different and unpredictable behaviour, as seen in Figure 24 and Figure 25. It can be surmised that the Si and Mn segregate together in the pearlite. Again, in case of alloy 5A [1.5Si2Mn], many of the recrystallization nuclei are present at the deformed pearlite and ferrite boundaries, along with some of them between the ferrite boundaries.

4.4 GRAIN GROWTH

The grain growth parameter K, has been calculated by using the microscopy results as input parameters for the model described in Section 2.4.2. This parameter can give idea about the mobility of the grain boundary, which can help in understanding of solute drag effect.

The significant effect of Mn on the growth is evident (Figure 37). It is evident that Mn addition reduces the growth rate significantly in all cases. Addition of Si to low Mn alloys, is leading to a slight decrease in the growth parameter. Caution must be taken while interpreting these results, as they take into account the conditions before the impingement of the grains. Addition of small amount of Si (0 wt. % to 0.4 wt. %) to high Mn alloys doesn’t produce a major change in the growth rate. But at 1% Si, the growth rate dips. The concentration at 1 wt. % Si corresponds to 1:1 atomic fractions of Si and Mn. This indicates some special interaction between Si and Mn, leading to an enhanced solute drag. At higher Si contents (1.5 wt. %), the growth rate is higher. The changes in the growth rate, when Si deviates away from 1 wt. % Si in presence of 2 wt. % Mn, indicates that the special interaction mentioned above is dependent on relative concentrations of Si and Mn. The observation at 1% and 1.5% Si is consistent with the observation of recrystallization rates seen in Figure 18. The recrystallization rate is quite different at 0% and 0.4% Si in high Mn alloys. But here, the growth rates are nearly comparable. Moreover, the nucleation rate is not significantly different (Figure 30). Similar growth rates might be because, the Si might not be contributing to enhancing the solute drag at these concentrations. Si not contributing to solute drag might be because the fast moving grain boundaries are able to ‘breakaway’ from Si. The ability for ‘breakaway’ seems dependent on relative concentrations of Si and Mn. Similar growth and nucleation rates, along with a higher rate of recrystallization (Figure 18) is surprising. This could be possible because in alloy with 0.4 wt. % Si has RX_{start} at higher temperatures, leading to faster rate of recrystallization.

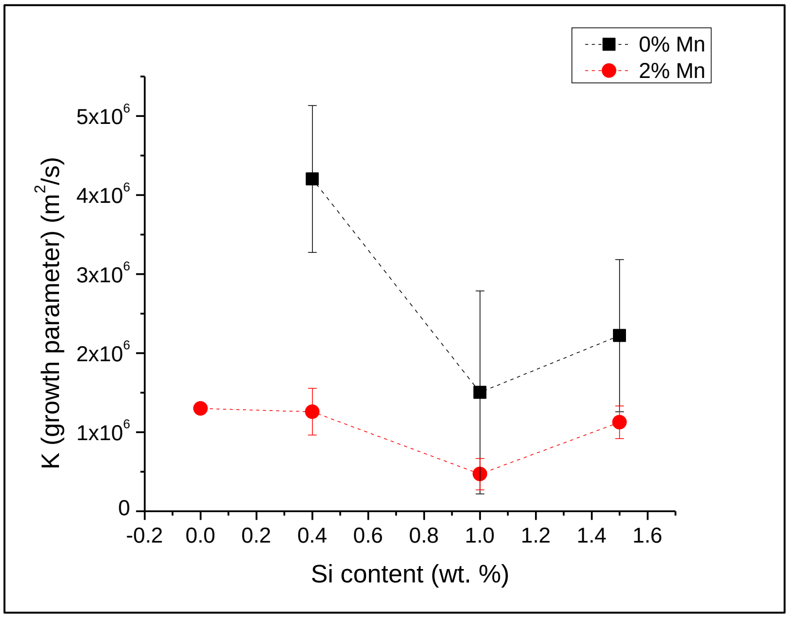

Figure 37 Parameter for growth (K)

4.4 MODEL FITTING

The modified JMAK model described in Section 2.4.1, was fit to the experimental XRD results. The results for the fits for case of 1 K/s are shown in Figure 38 and Figure 39. For all the curve fits, the Avrami exponent, (m+1) is bound between 2 and 3, because even with microscopy, the case of site-saturation is not explicitly clear. The recrystallization involves migration of high angle grain boundaries. Activation energy for this process is self-diffusion of atoms in the matrix. Therefore, activation energy values for self-diffusion of Fe in ferrite matrix are used. These values were derived from DICTRA. The activation energy value for each composition are given in Table 7.

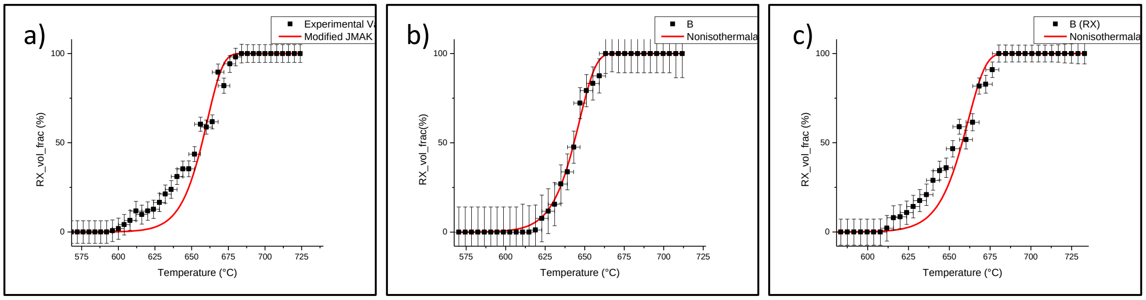

Figure 38 Curve fits for the experimental data of a) Alloy 2A (0Si2Mn) b) Alloy 2B (0.4Si2Mn) c) Alloy 4A (1Si2Mn) at 1 K/s

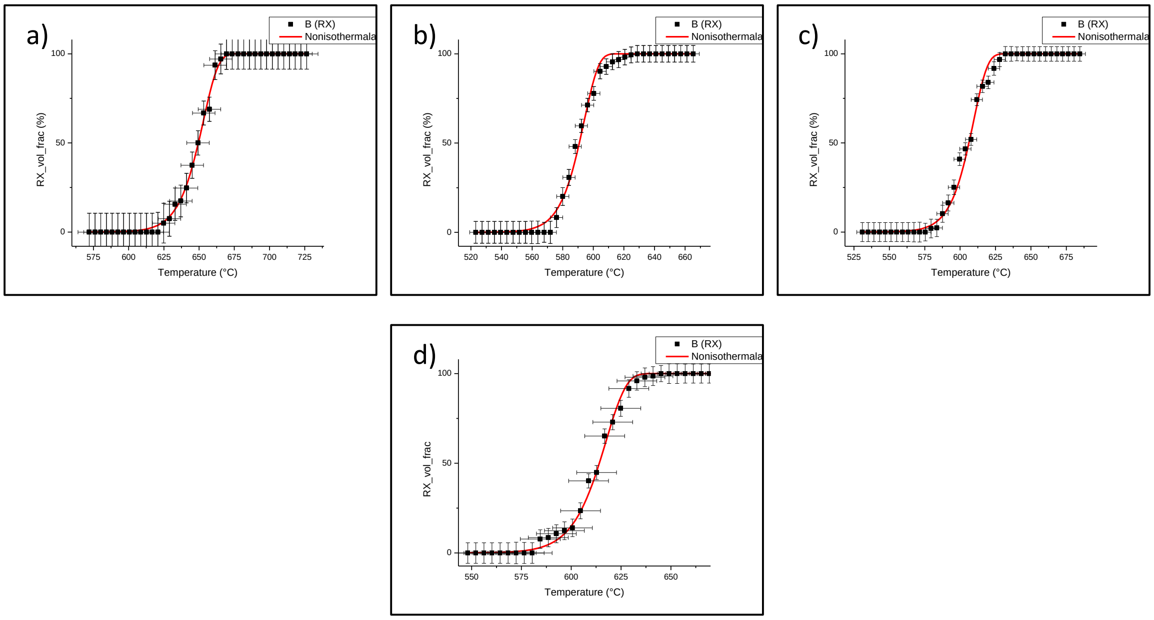

Figure 39 Curve fits for the experimental data of a) Alloy 5A (1.5Si2Mn) b) Alloy 6A (0.4Si0Mn) c) Alloy 7A (1Si0Mn) and d) Alloy 7B (1.5Si0Mn) at 1 K/s

The model fitting gives the information about parameter k_o (rate constant). The variation of this parameter with alloying is shown in Figure 40. Also, as the Avrami exponent is not completely fixed, the values of Avrami exponent are shown in Table 8. For Avrami exponent, it is seen for most of the alloys that the values are quite close to 2. This represents 2D growth with site-saturation. This supports the inference of site-saturation and 2D growth made from the microscopy results.

From the plot in Figure 40, it is clear that the low Mn alloys are having higher rate constant. In case of high Mn alloys, the rate constant is smaller. This points to the role of Mn in reducing the rate of recrystallization significantly. But, with increasing Si in high Mn alloys, trend is unpredictable as seen earlier in Figure 18. The addition of Si to low Mn alloys, is leading to a continuous decrease in the rate constant. This points to a clear role of Si in solute drag on a smaller scale when compared to Mn. Moreover, this decrease in rate constant is not dependent on nucleation, because nucleation is constant for low Mn alloys. When compared to the RX_{start} temperatures, the increase in Si from 0 wt.% to 0.4 wt.% in high Mn alloys has led to increase of RX_{start}, which can be attributed to solute drag effect. But, solute drag is not affecting the growth rate. It could be because, such a small amount of Si is not able to interact with the moving grain boundaries. But, similar growth and nucleation rates at higher temperatures have resulted in higher rate constant. At higher Si concentrations in high Mn alloys, the rate constant is much smaller. This could be due to higher solute drag effect because of higher solute concentrations. For alloy 4A (1Si2Mn), rate constant is smallest, reaffirming the enhanced interaction seen earlier. In alloy 5A (1.5Si2Mn), the rate constant has increased by a small amount. It can be because, the grain boundaries are able to 'breakaway' from Si again. Thus, it can be deduced that the 'enhanced' interaction between Si and moving boundaries is concentration dependent.

Table 7 Activation energy values of self-diffusion of Fe in ferrite from DICTRA

Alloy	Activation Energy (kJ/mol)
2A (0Si2Mn)	332.279
2B (0.4Si2Mn)	330.441
4A (1Si2Mn)	327.374
5A (1.5Si2Mn)	324.992
6A (0.4Si0Mn)	323.546
7A (1Si0Mn)	320.181
7B (1.5Si0Mn)	317.525

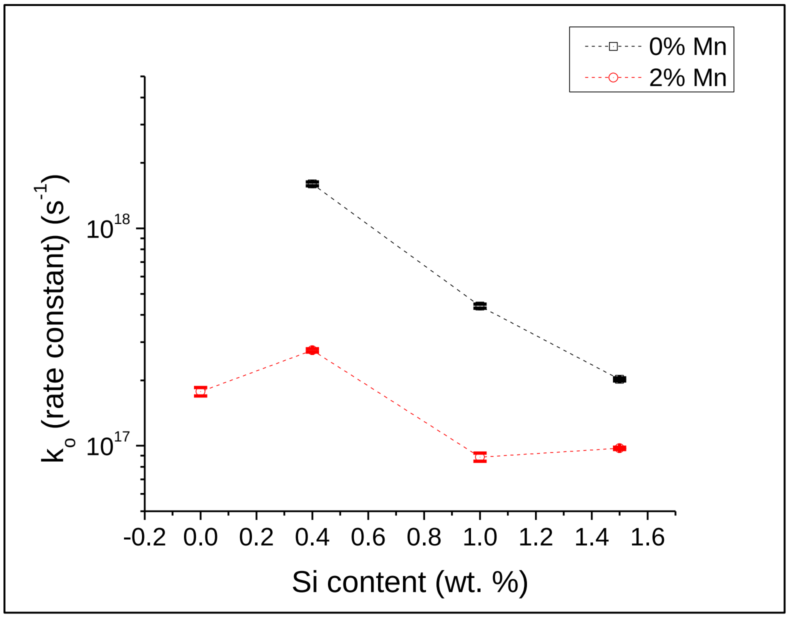

Figure 40 The variation of k_o values with alloying for annealing at 1 K/s

Table 8 Values of Avrami exponent from model fit

Alloy	Avrami exponent (m+1)	Error
2A (0Si2Mn)	2	0.22936
2B (0.4Si2Mn)	2	0.09511
4A (1Si2Mn)	2	0.21623
5A (1.5Si2Mn)	2.01575	0.07086
6A (0.4Si0Mn)	2	0.11146
7A (1Si0Mn)	2	0.11558
7B (1.5Si0Mn)	2	0.08514

EXPERIMENTAL RATE CONSTANT

In Figure 41, the experimental rate constant is calculated using the equation (10). When compared to Figure 40, the magnitude of the rate constant is different. This difference might be because of the fact that the nucleation rate is for 2-dimensional observation. For 3-dimensional case, nucleation rate would have a higher value. Thus, for experimental values and the model values, the trends are being studied. Even in the experimental values the effect of Mn in reducing the rate constant is evident. For high Mn alloys, the trends in the change of rate constant are same as for the values from the model. The only difference, being that at 1.5% Si, the experimental rate constant has increased. The rate constant from model fitting is not increasing at 1.5% Si. It can be possible that impingement is significant for alloy 5A (1.5Si2Mn). The impingement is not captured in the grain growth model. Therefore, the experimental rate constant shows increasing value. For low Mn alloys as well, the change from 1% Si to 1.5% Si is different from the one seen in model values. Again this could be due to the possibility of impingement of grains.

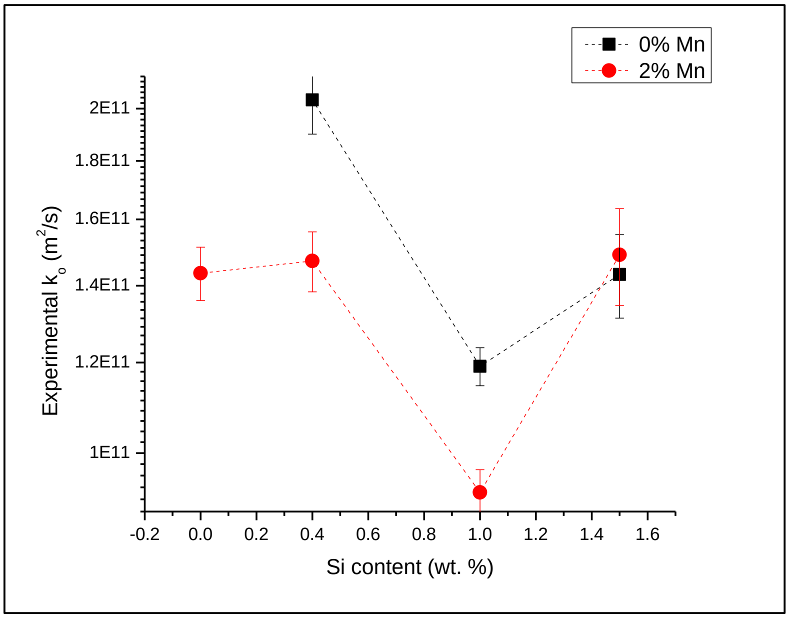

Figure 41 Experimental k_o with alloying from microstructure characterization of samples annealed at 1 K/s

Other than the cases of very high Si contents, the trends of experimental rate constant are consistent with the trends of the model values. This signifies that the rate constant from model fit is corresponding to actual microstructural evolution. Therefore, the parameters obtained from model fitting can be used to make predictions for other cases. This would be discussed next.

4.5 MODEL FITTING FOR OTHER CASES

It was seen in Section 4.4, that the experimental rate constant and the rate constant derived from model fitting have consistent trends when compared to each other. This means that the JMAK model is able to describe the microstructural evolution upto some extent at 1 K/s. To check the validity of JMAK model at other heating rates, the inputs that were used earlier have been used again to perform a model fitting of the experimental data at other heating rates. The model fits were done with the activation energy values (Table 7) and the Avrami exponent as input. The activation energy doesn't change with heating rates as it is based on an atomic process. It was seen in the microstructure analysis that, the reason for 2D growth is mainly because of the initial microstructure. Therefore, even the Avrami constant could be assumed constant. Moreover, the nucleation in recrystallization is mostly site-saturation [13]. Thus, using same input parameters seems reasonable. The curve fits can be seen in Appendix F.

The output parameter from these model fits is the rate constant. The rate constants for different heating rates and alloys are shown in Figure 42 and Figure 43. The alloys with low Mn show a continuous decrease in the rate constant for all heating rates. This is because of the small solute drag effect of Si as mentioned in Section 4.4. The rate constant for conditions of 0.1 K/s and 5 K/s is lower than that for the case of 1 K/s. For 0.1 K/s, the RX_{start} is at lower temperature. At lower temperatures, not all the potential nucleation sites would get activated. Therefore, the rate constant might be lower. The exact verification of this inference would require detailed microstructure characterization, as described in earlier sections. In case of higher heating rates, the RX_{start} is at higher temperatures. Thus, more potential nucleation sites are activated. This implies that the nucleation rates would be higher. Even so, the rate constant is lower. At higher temperatures, the large number of nuclei are formed and they initially grow very fast. As a consequence of high nucleation rate, grain impingement occurs very soon, leading to a slowdown in growth rate for a large part of the process. This could be a possible reason for reduction in the rate constant.

When compared with the rate constant of high Mn alloys, the rate constant of low Mn alloys is significantly higher. This points to a strong solute drag effect of Mn, which was seen earlier in the results of growth rates, and recrystallization temperatures. The trends of rate constant for high Mn alloys are not the same for all the heating rates. The trends of 1 K/s and 5 K/s, tend to be similar. The difference in trends of 5 K/s is that, the differences between the alloys with different Si content is not very high. Moreover, the trends of 5 K/s have a high resemblance with the trends of growth rate of high Mn alloys (Figure 37). This can point to a possibility that the nucleation rates are not much different at high heating rates. This is possible, because at higher temperatures most of the possible nucleation sites would get activated. Therefore, the only factor that would affect the trend of rate constant at high heating rates would be growth rate. This observation adds credence to the hypothesis that at higher heating rates, all the potential nucleation sites would get activated. At low heating rates (0.1 K/s), the trends don't match completely with the trends of 1 K/s. The observations made till now are not able to explain these deviations. These trends could either be true or might be so because JMAK is not able to capture the microstructure evolution effectively in this case. To verify this, a detailed microstructure characterization at slow heating rates is required. The possible reasons for these deviations in trends could be microstructure inhomogeneity and grain growth behaviour. At lower temperatures, the nuclei will be activated only in specific sites with very high stored energy of deformation. Moreover, as the heating rate is slow, it might not be able to compensate the reduction of growth rate as the recrystallization progresses. These two scenarios would make the actual microstructure evolution quite different from the assumptions of JMAK. Consequently, the JMAK would lead to some inaccurate values. Therefore, it could be surmised that the JMAK is able to describe the progress of recrystallization better at higher heating rates than for cases of low heating rates.

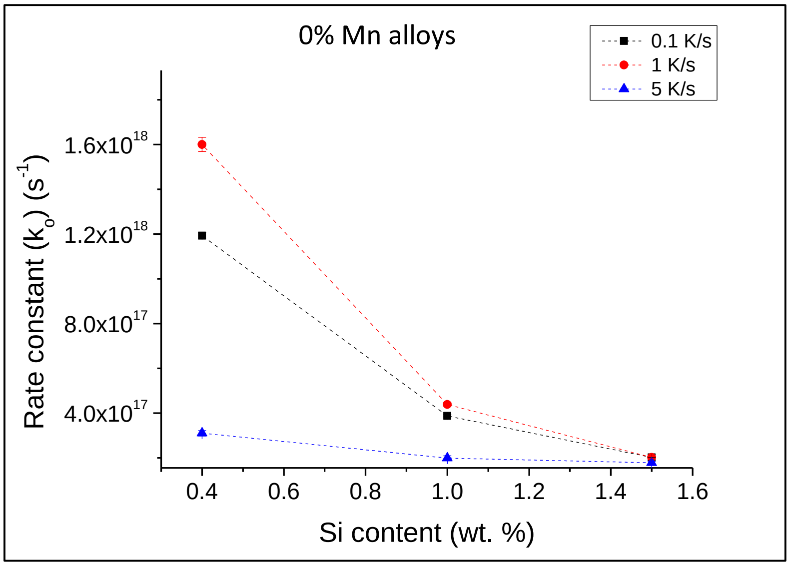

Figure 42 k_o values for different heating rates for alloys with 0% Mn

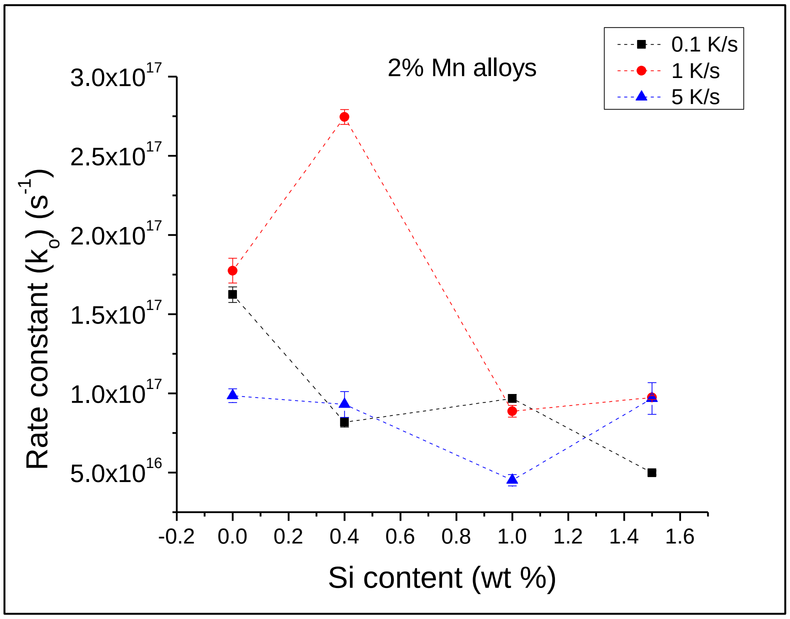

Figure 43 k_o values for different heating rates for alloys with 2% Mn

4.6 SUMMARY

Even with all the results, some additional explanation is required for the variations that exist between the different alloys. This section aims to build up a theory that would be able to explain the role of individual elements and also, role of these elements when they are together.

THEORY

From the results, it is evident that many factors are at play, which together influence the recrystallization. The most important factors are: nucleation rates, solute drag and its influence on grain growth. Moreover, behaviour of these factors depends ultimately on the alloying elements. The complex interaction between these factors leads to the observed changes in the recrystallization temperatures and the rates of recrystallization.

The number of nuclei or the density of nucleation sites certainly affects the recrystallization, but this effect is of a multiplicative nature. It cannot explain the complex interactions. The complex interactions and behaviour arises due to grain growth. The source of such complex behaviour of grain growth behaviour seems to be solute drag effect.

The theory in Section 2.4.3 can explain the influence of concentration of solute elements and interactions between them and interactions of solute atoms with the boundary. But the theory doesn't take into account, the influence of velocity of the grain boundary. This can be an important factor in deciding the solute drag, as seen in [42]. At higher velocities, the grain boundary 'breaks away' from the solute atmosphere, and thus, solute drag effect is reduced. For stationary grain boundaries, the effect of solute drag as envisioned from the theory is quite applicable. Therefore, the RX_{start} temperatures can be explained by using the theory in section 2.4.3, if nucleation is taken together into account. According to the theory, rise in concentration should lead to a rise in solute drag effect. Thus, maximum solute drag was seen for alloy 5A (1.5Si2Mn) and consequently, this alloy had the highest RX_start temperature. Alloy 4A (1Si2Mn) should also have higher RX_start temperature, but it has a higher nucleation rate, when compared to alloy 2B (0.4Si2Mn).

As the grain boundaries start moving, their velocities are high at the start of the recrystallization. At this stage, it is important to see which solute elements 'cling' to this fast moving boundary. Mn due to its strong solute drag capability, tends to 'cling' to the boundary, even at high velocities. But, Si has lower solute drag effect (because it can diffuse faster in the matrix than Mn), therefore, it might not cling to fast moving boundaries. This has been observed between alloys 2A (0Si2Mn) and 2B (0.4Si2Mn). Among these two alloys, the RX_{start} temperatures have increased, but the growth rates and nucleation rates have remained nearly the same. The increase in RX_{start} temperature can be explained by increased solute drag at the start due to increased solute concentrations. Even with higher solute concentrations, the grain growth is nearly the same. This is possible when, solute drag effect reduces as the grain boundary moves. This indicates that the solute concentrations at the boundary decreases as the boundary moves. As the growth rate is same as alloy with no Si, it can be inferred that the effect of Si on solute drag is eliminated. This supports the hypothesis that Si might not be able to cling to a 'fast moving' boundary. Moreover, as the growth rate of alloy 2B (0.4Si2Mn) remains same as that of alloy 2A (0Si2Mn), it can be surmised that the grain boundaries are not breaking away from Mn. The modest increase in the RX_{start} temperatures in low Mn alloys after addition of Si seems to be a possible consequence of this hypothesis. Even at high Si concentrations the solute drag effect is subdued because of breakaway of the boundaries from Si.

This phenomenon of 'breakaway' of boundary from solutes, seems to depend on the relative concentrations on Si and Mn. As the Si concentration in high Mn alloys increases (from 0.4 wt.% to 1 wt.%), the growth rate has decreased. This can mean that at 1 wt.% Si the breakaway was not effective. It can be inferred that presence of Mn influences the Si interaction with the moving grain boundaries. This might be possible due to the 'co-segregation' effect [45]. Co-segregation effect increases the solute drag effect when compared to individual scenarios [45]. It can be surmised that co-segregation is increasing the interaction of Si with the boundary. When the data of alloys 4A (1Si2Mn) and alloy 5A (1.5Si2Mn) is compared, it is seen that RX_start is higher for alloy 5A (1.5Si2Mn), which is expected. But, the growth rate of alloy 5A (1.5Si2Mn) is also higher. This means that the grain boundary is able to break away from Si in alloy 5A (1.5Si2Mn). Whereas, the alloy 4A (1Si2Mn) has the lowest growth rate, which would also mean that, in this alloy, the breakaway of the grain boundaries is not so feasible. These examples, point to a dependence of the strength of co-segregation on the relative concentration of the solute elements. For alloy 4A(1Si2Mn), the atomic percentages for Si and Mn are 2% each. Therefore, there is one Si atom for each Mn atom, which might be leading to an optimum and strong co-segregation effect

APPLICABILITY OF THE SOLUTE DRAG MODEL

The solute drag model explained in section 2.4.3 and appendix C, accounts for the interactions between the solute atoms in the grain boundaries. As seen in the previous section, in the high Mn alloys, the co-segregation behaviour depends on the relative concentrations on Si and Mn. This means that the interaction between Si and Mn changes with concentrations. There are two parameters which would account for interaction between the solute elements. One of the parameters is ε, the lower the value of this parameter, stronger is the interaction between the pair of solute elements. This parameter should be constant, as it is actually the heat of mixing. The other parameter, which can also account for interaction of elements in the grain boundary is β. As defined in equation (A.32), it is the ratio of changes in the chemical potentials when the solute elements move into the boundary from the bulk. It can be assumed that this parameter might be getting influenced by the concentration. This is plausible, because changes in the bulk composition would change the chemical potentials of the solute elements in the bulk and thus, cause changes in β. Currently, there is no information about this parameter for the combination of Si and Mn. This makes meaningful calculations difficult. Therefore, the model described in Section 2.4.3 is only used for qualitative explanations. Moreover, the values of these parameters would change with the velocity of the grain boundary. This also needs to be taken into account for accurate calculations.

5. CONCLUSIONS

The thesis has shed more light on the role of Si and Mn in ferrite recrystallization. These elements were not studied together earlier and therefore; a lot of new information has been found.

1. The modified JMAK model works better for the cases of higher heating rates than for cases of low heating rates. This could be due to the effect of microstructural inhomogeneity and non-constant growth rate.
2. On their own, Mn and Si retard recrystallization. The retardation effect of Mn is much stronger than that of Si.
3. Two potential nucleation sites are possible. One of these sites are the boundaries between the deformed pearlite and ferrite. The other nucleation site observed was in between the ferrite grains boundaries. These sites corresponded to micro-segregation of Mn. Therefore, the density of nucleation sites is dependent on the pearlite content and pearlite distribution. As the pearlite content increases, the density of nucleation sites increases. In some alloys with similar pearlite contents, the density of nucleation sites changed a bit. These small variations could be due to the differences in micro-segregation behaviour of Mn. The segregation of Si doesn't affect the nucleation much.
4. The nucleation is site-saturation in most of the cases. This corresponds to Avrami exponent of 2, for the condition of 2-dimensional growth. Most of the alloys have Avrami exponents very near to 2.
5. The growth of the grains is 2-dimensional. The amount of 2-dimensional growth is more in high Mn alloys, which could be because of higher pearlite banding in these alloys. The amount of pearlite banding is also proportional to the pearlite content.
6. The growth rate is lowest at the concentration, where atomic fractions of Si and Mn are 1:1. This points to an enhanced interaction between Si and Mn atoms. Strength of these interactions seems to be dependent on the relative concentrations of Si and Mn.

6. FUTURE RECOMMENDATIONS

1. Even more accurate description of the recrystallization kinetics curve can be obtained, if complete Debye rings could be captured by the 2D detectors. Also, the effect of noise in the XRD signal could be reduced by use of higher energy source for X-rays. Thus, it seems that the recrystallization could be studied with even more accuracy by use of Synchrotron radiation. Moreover, the synchrotron radiation can also give more information about the microstructural evolution. It can help in settling the question about site-saturated nucleation.
2. At higher heating rates the accuracy of the data is significantly reduced during in-situ 2D XRD analysis, due to limits of the detectors. If faster detectors become available, then the accuracy of measurements at higher heating rates would be higher.
3. Solute segregation to grain boundaries is quite important during recrystallization. Therefore, some studies by use of Atom Probe techniques are required to have a more thorough understanding. The studies should aim at studying the changes in grain boundary concentrations, with different Si and Mn contents. These studies can also be useful for ferrite to austenite transformations.
4. Some modelling or experimental measurements to calculate the parameter, β in the solute drag model can help in understanding the changes in interaction between Si and Mn with changes in their relative concentrations. This can help in calculating exact mobility of the boundaries as a function of alloying. This can be very helpful in predictions about recrystallization.
5. The texture effects would play a huge role in terms of nucleation and growth. The oriented nucleation and oriented growth is always present in recrystallization. This oriented nucleation and growth might change with the alloying.

APPENDIX

A. MODIFIED JMAK MODEL

The JMAK model is basically developed for isothermal conditions. But in the case being studied, the condition is not of isothermal annealing but of continuous heating. Thus, the JMAK equation has to be modified for the continuous heating case, as done by Farjas et al. [32].

Transformed fraction (or recrystallized fraction) can be given as –

$$\alpha = 1 - \exp[-\alpha_{ex}] \tag{A.1}$$

Where α_{ex} is the extended volume, i.e the transformed volume if the nuclei grow through each other and overlap.

$$\alpha_{ex} = \int_0^t N(\tau) \upsilon(\tau, t) d\tau \tag{A.2}$$

N is the nucleation rate at time τ and v is the volume transformed by a nucleus nucleated at time τ growing till time t.

$$\upsilon(\tau, t) = \sigma \left(\int_\tau^t G(z) dz \right)^m \tag{A.3}$$

Here σ is the geometrical shape factor, G is the growth rate and m is dependent on the type of growth (for example, m is 3 for 3-dimensional growth with constant nucleation and growth rates)

When these equations with general assumptions, we get the equation (A.4):

$$\alpha = 1 - exp[-(kt)^{m+1}] \tag{A.4}$$

the overall rate constant is given by –

$$k = \left(\frac{\sigma N G^m}{m+1} \right)^{\frac{1}{m+1}} \tag{A.5}$$

N and G can be described by the Arrhenius relationship,

$$N = N_o \exp\left(-\frac{E_N}{K_B T} \right) \tag{A.6}$$

$$G = G_o \exp\left(-\frac{E_G}{K_B T} \right) \tag{A.7}$$

Substituting equation (A.6) and (A.7) in equation (A.5),

$$k = \left(\frac{\sigma N_o {G_o}^m}{m+1} \right)^{\frac{1}{m+1}} \exp\left(-\frac{E}{K_B T} \right) = k_o exp\left(-\frac{E}{K_B T} \right) \tag{A.8}$$

The overall activation energy can be defined as

$$E \equiv \frac{E_N + mE_G}{m+1} \tag{A.9}$$

Under non-isothermal conditions of constant heating rate, the equations (A.1), (A.2), (A.3), (A.6), (A.7) are still valid. But, the integration is much more difficult. So, integrating equation (A.3) would involve substituting T as $T_o+\beta t$, where β is the heating rate and t is the time. The further equations require the definitions of exponential integrals to be used as seen in [32]. This gives the following equation –

$$\alpha_{ex} = \sigma {G_o}^m N_o \left(\frac{E_G}{K_B T}\right)^{m+1} \int_x^\infty \exp\left(-\frac{E_N}{E_G}u\right)\frac{1}{u^2}[p(x) - p(u)]^m du \tag{A.10}$$

Where $x = E_G/K_BT$ and p(x) is defined as –

$$p(x) \equiv \int_x^\infty \frac{\exp(-u)}{u^2} du \tag{A.11}$$

This function p(x) consists of exponential integral, which cannot be expressed in analytical form and thus, some approximations have to be used. The major differences in the many models developed for non-isothermal cases arise due to the usage of these approximations for p(x). In the models by Vasquez et al. [58] and by Woldt [59], the first order approximation for p(x) is substituted directly in the equation (A.10) and then the integration is carried out. Whereas, in the method by Farjas et al. [32], the integral in equation (A.10) is solved by integration parts continuously and then in the final step the approximation for p(x) is used. This results in difference in the equations for fraction transformed in terms of pre-exponential factors. The first order approximation used for p(x) is –

$$p(x) \approx \frac{\exp(-x)}{x^2} \tag{A.12}$$

The model of Farjas et al. [32] is more accurate than the results of Vasquez [58] and Woldt [59]. Therefore, the solution by Farjas et al. [32] would be used for fitting the experimental results. The solution is given by the following two cases – isokinetic case [equation (A.13)] and a general case [equation (A.14)].

$$\alpha = 1 - exp\left\{-\left[k_o \frac{E}{\beta K_B} p\left(\frac{E}{K_B T}\right)\right]^{m+1}\right\} \tag{A.13}$$

$$\alpha = 1 - exp\left\{-\left[k_o C \frac{E}{\beta K_B} p\left(\frac{E}{K_B T}\right)\right]^{m+1}\right\} \tag{A.14}$$

Where C is given by,

$$C = \left(\frac{(m+1)!\, E^{m+1}}{\prod_{i=0}^{m}(E_N + iE_G)}\right)^{\left(\frac{1}{m+1}\right)} \tag{A.15}$$

It has been mentioned by Farjas et al. [32] that the isokinetic case is applicable in the cases where the $E_N=E_G$ or in the case of site-saturation and the other condition being that the transformation rate is not dependent on thermal history (heating rate). For cases, where $E_N \neq E_G$, then the general case is applicable. But, it was found that, in the limiting cases of $E_N \gg E_G$ and $E_G \gg E_N$, the isokinetic description is more accurate. Based on these considerations and along with the assumption that the nucleation in recrystallization is of site-saturation type for most cases, equation (A.13) would be used for predictions for kinetics in our case.

B. GRAIN GROWTH MODEL

The driving force for the grain growth during recrystallization is a sum of contributions from the stored energy of deformation, curvature of the grains and the retarding force due to solutes. Even in such a scenario, the grain growth can be approximated by the grain growth equation based on curvature driven grain growth. The only difference in this case would be that the values for surface energy of the grain boundary would turn out to be higher. It wouldn't make a difference to the mobility values as shown in this section. Moreover, the theory might not be an accurate picture as it works for un-impinged grains.

The velocity of a grain boundary is described as,

$$v = MF \qquad (A.16)$$

Where M is the mobility of the grain boundary, F is the driving force for the grain boundary motion. F is actually a sum of contributions from the stored energy of deformation, curvature of the grains and the retarding force due to solutes.

$$F = Gb^2\rho + 2\frac{\gamma}{D} - F_{drag} \qquad (A.17)$$

Where G is the shear modulus, b is the burger's vector, ρ is the dislocation density, γ is the surface energy of the grain boundary and D is the diameter of the grain. This simplification will result in the equation of F as,

$$F = \frac{2\gamma_{app}}{D} \qquad (A.18)$$

where, γ_{app} is the apparent surface energy of the boundary, which is different because of the change in the expression of driving force.

The mobility is decided by the diffusion theory [17]. It is given by,

$$M = \frac{An\upsilon V_m}{RTN_a}\exp\left(\frac{\Delta S^a}{R}\right)\exp\left(\frac{-\Delta H^a}{RT}\right) = \frac{An\upsilon V_m}{RTN_a}\exp\left(\frac{-\Delta G^a}{RT}\right) \qquad (A.19)$$

Where, A is the probability that the atom from grain 1 will find a suitable place in grain 2, n is the number of atoms per unit area in favourable position to make a jump, ν is the vibration frequency of the atoms, V_m is the molar volume and N_a is the Avogadro's number. It can be seen that due to the assumption in equation (A.18), the velocity (growth rate) of a grain boundary is proportional to the diameter of the grains.

$$v = \alpha M\frac{2\gamma_{app}}{D} = \frac{dD}{dt} \qquad (A.20)$$

This equation is valid for the isothermal case. For non-isothermal cases, some changes have to be made. The condition for continuous heating is used. Therefore, T=βt. So, the equation (A.20) can be represented as,

$$\frac{2\alpha M\gamma_{app}}{\beta}dT = DdD \tag{A.21}$$

Integrating this equation and using $M = M_o\exp(-\frac{Q}{RT})$ and using the approximation of exponential integrals mentioned earlier, the following expression is found,

$$D^2 - D_o^2 = \frac{KR}{\beta E}\left\{\left(T_f^2\exp\left(-\frac{E}{RT_f}\right)\right) - \left(T_i^2\exp\left(-\frac{E}{RT_i}\right)\right)\right\} \tag{A.22}$$

$$K = 4\alpha\gamma_{app}M_o \tag{A.23}$$

By consideration of definition of growth rate of grain boundary and from equations (A.16),(A.7), G_o can be expressed as $G_o = M_oF$. Therefore, the equations (A.22) and (A.23) can be used to calculate pre-exponential factor of mobility. The parameter K (equation (23)) is also correlated to the pre-exponential factor K_o from JMAK analysis (equation (A.8)).

By comparing the equation (A.8) and equation (A.23), pre-exponential factor can be expressed as,

$$k_o = \left[\frac{\sigma N_o}{(m+1)}\left(\frac{KF}{4\alpha\gamma}\right)^m\right]^{\frac{1}{m+1}} \tag{A.24}$$

Using the equation (A.18) as the definition for F, k_o can be expressed as,

$$k_0 = \left[\frac{\sigma N_0}{m+1}\left(\frac{K}{2\alpha D}\right)^m\right]^{\frac{1}{m+1}} \tag{A.25}$$

Where, D can be assumed as D_o (D at 10%), because the theory works well when the grains are un-impinged.

C. RELATION FOR CHANGE IN ACTIVATION ENERGY WITH ALLOYING

The activation energy in case of recrystallization is the activation energy for grain boundary migration. But, when solute drag is present, then the drag force changes, which can be interpreted as a change in the activation energy of grain boundary migration.

In presence of solutes segregated to the boundary, the velocity of the grain boundary is equal to the velocity of the solutes. If the boundary moves under an action of a driving force F, it will impart same driving force on the solute atoms as well

$$v_b = m_bF = m_{im}\frac{F}{c_b - c} \tag{A.26}$$

Where, m_b is the mobility of the boundary, m_{im} is the mobility of the impurity atoms, c_b is the concentration of solutes at the boundary and c is the concentration in the solid solution.

From Nernst equation,

$$m_b = \frac{m_{im}}{c_b - c} = \frac{D}{(c_b - c)kT} \tag{A.27}$$

For dilute solutions, using the Henry's isotherm gives,

$$c_b = zB_o e^{\frac{H_i}{kT}} c \qquad (A.28)$$

Where, z is the number of adsorption sites in the boundary, $B_o = e^{\frac{-S_i}{kT}}$, H_i is the interaction enthalpy of the impurity atoms with the grain boundary.

This leads to,

$$m_b = \frac{D_o e^{\frac{-(H_D+H_i)}{kT}}}{zB_o kTc} \qquad (A.29)$$

According to Equation (A.29), the activation enthalpy for grain boundary migration is the sum of two activation enthalpies, impurity diffusion and impurity adsorption. The pre-exponential mobility factor changes inversely proportionally to the impurity concentration contrary to experimental results. It has been seen [18], that even at the lowest impurity content, the activation enthalpy rises with increasing impurity concentration, whereas the pre-exponential factor remains essentially at the same level. This points to the fact that the interaction between the adsorbed impurity atoms should also be taken into account.

A binary system is considered in the bulk as well as the boundary, with c_1 and c_2 are the concentrations of the first and the second component respectively. The concentrations would be represented in form of fractions. It is assumed that the chemical potentials of the components in the bulk and the boundary are the same.

$$\mu_1^b(\gamma_1, T, c_1^b) = \mu_1^v(p, T, c_1^v) \qquad (A.30)$$

$$\mu_2^b(\gamma_2, T, c_2^b) = \mu_2^v(p, T, c_2^v)$$

Where the μ_1^b, μ_2^b and μ_1^v, μ_2^v are the chemical potentials of the first and second component in the boundary and the bulk respectively. Similar notation for concentrations, c_1 and c_2. When the atoms go in the grain boundary, their activity changes, which is given as,

$$\frac{a_1^b}{a_1} = (\frac{a_2^b}{a_2})^{\frac{\omega_1}{\omega_2}} \exp\left(\frac{\omega_1(\gamma_2 - \gamma_1)}{kT}\right)$$

Where, γ_1, γ_2 are the surface tensions of the component 1 and component 2 in the grain boundary. The ω_1, ω_2 are the partial areas defined as,

$$\omega_1 = -\left(\frac{\partial \mu_1^b}{\partial \gamma_1}\right) \qquad (A.32)$$

which physically means as the change in the chemical potential of the atom as the surface tension for the atom changes. This would represent the tendency for the atom to segregate in the grain boundary.

Activity of a component in a regular solution is given by,

$$a_1 = c_1 exp\left[\frac{z\varepsilon c_2^2}{kT}\right] \qquad (A.33)$$

Where, z is the co-ordination number, ε is the heat of mixing ($\varepsilon = \varepsilon_{12} - \frac{\varepsilon_{11}+\varepsilon_{12}}{2}$). The equations (A.33) and (A.31) give a relation for concentrations,

$$\frac{c_1^b}{c_1} = \frac{\exp\left(\frac{z\varepsilon c_2^2}{kT}\right)}{\exp\left(\frac{z^b\varepsilon^b (c_2^b)^2}{kT}\right)} \left[\frac{c_2^b \exp\left(\frac{z^b\varepsilon^b \left(c_1^b\right)^2}{kT}\right)}{c_2 \exp\left(\frac{z\varepsilon c_1^2}{kT}\right)}\right]^{\frac{\omega_1}{\omega_2}} \exp\left(\frac{\omega_1(\gamma_1-\gamma_2)}{kT}\right) \qquad (A.34)$$

For the case of regular solution at the grain boundary and ideal solution in the bulk and the partial areas of the components are different, ε = 0, $\varepsilon^b \neq 0$, $\omega_1 \neq \omega_2$ and assuming $B = \exp\left(\frac{\omega_1(\gamma_1-\gamma_2)}{kT}\right) = B_o e^{\frac{H_i}{kT}}$, where H$_i$ is the enthalpy of interaction between the boundary and the impurity atom. This would lead to following expression,

$$c_1^b = c_1 \exp\left(\frac{-z^b\varepsilon^b \left(c_2^b\right)^2}{kT}\right) B \left\{\frac{c_2^b}{c_2} exp\left[\frac{z^b\varepsilon^b \left(c_1^b\right)^2}{kT}\right]\right\}^{\frac{\omega_1}{\omega_2}} \qquad (A.35)$$

Substituting this in equation for mobility of the boundary,

$$m_b = \frac{m_{im}}{c_b - c} \cong \frac{m_{im}}{c_b} = \frac{m_o}{B_o c} \frac{\exp\left[-\frac{H_D + H_i + (\beta-1)z\varepsilon(1-c_b)^2}{kT}\right]}{\left(\frac{1-c_b}{1-c}\right)^{\beta}} \qquad (A.36)$$

where, $\beta = {}^{\omega_2}/_{\omega_1}$. The choice of the first and second component is dependent on the user and thus, the definitions of the other parameters would change accordingly. From the definition of partial areas in equation (A.32), it can be deduced that in case of Si and Mn, the changes in chemical potentials when they move into the boundary would be different. For Mn, the change in chemical potential is negative. But, Si in presence of Mn can undergo co-segregation and therefore, change in chemical potential can be negative. Therefore, it can be seen that β > 0. This is the reason why β could be used as parameter to quantify the interaction between the solute atoms in the grain boundary. Moreover, if the two elements like to be together, then ε < 0. So, finally it can be seen that such a combination would depict a rise in the activation energy.

This equation shows that the activation energy is a function of the concentration of solute at the boundary and also that the pre-exponential factor of the mobility is also dependent on the concentration.

$$H = H_D + H_i + (\beta-1)z\varepsilon(1-c_b)^2 \qquad (A.37)$$

D. COMPARISONS WITH THE EBSD DATA

The microstructural data from the SEM imaging is compared with EBSD to judge whether detecting recrystallized grains from SEM images is accurate enough or not. For this purposes, two aspects were compared – grain size distributions in terms of histograms and the recrystallized volume fraction.

Table 9 Comparing the recrystallized volume fractions obtained from the EBSD and SEM analysis

Alloy	RX_vol_frac (EBSD) (%)	RX_vol_frac (SEM) (%)
4A (1Si2Mn)	57.5 ± 3.225	49.20 ± 2.95
	61.53 ± 3.80	58.69 ± 2.96
5A (1.5Si2Mn)	19.66 ± 3.92	18.88 ± 2.99
	53.56 ± 3.29	63.14 ± 3.20

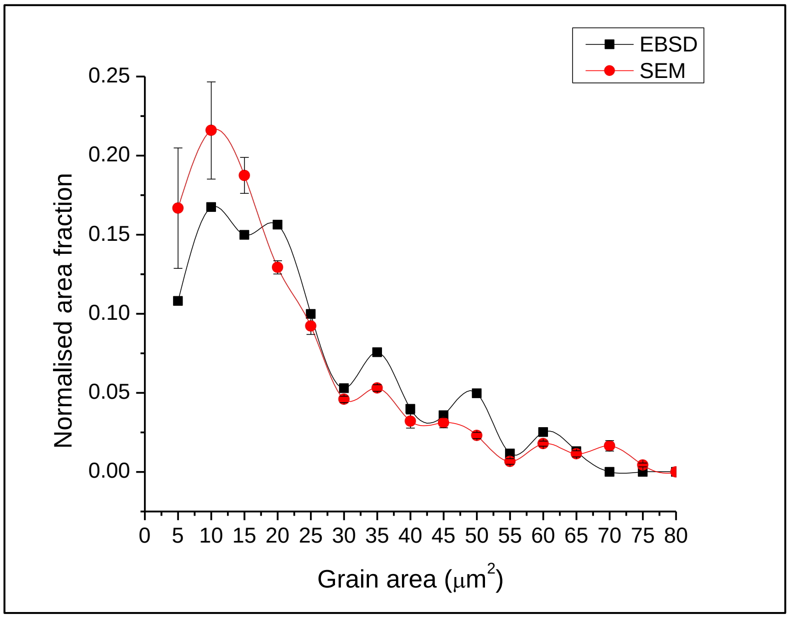

Figure 44 Comparison of Histograms for alloy 4A (1Si2Mn) at approximately 50% RX stage

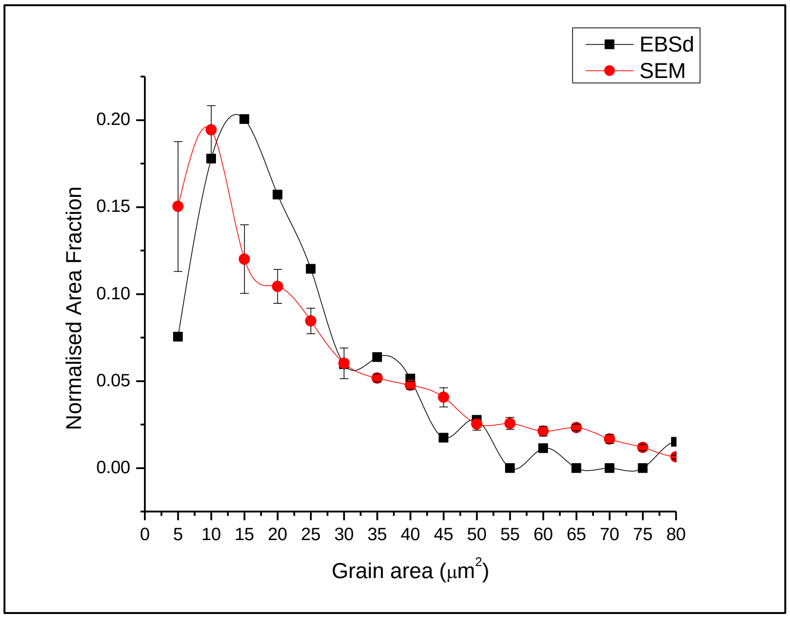

Figure 45 Comparison of Histograms for alloy 4A (1Si2Mn) for approximately 60% RX condition

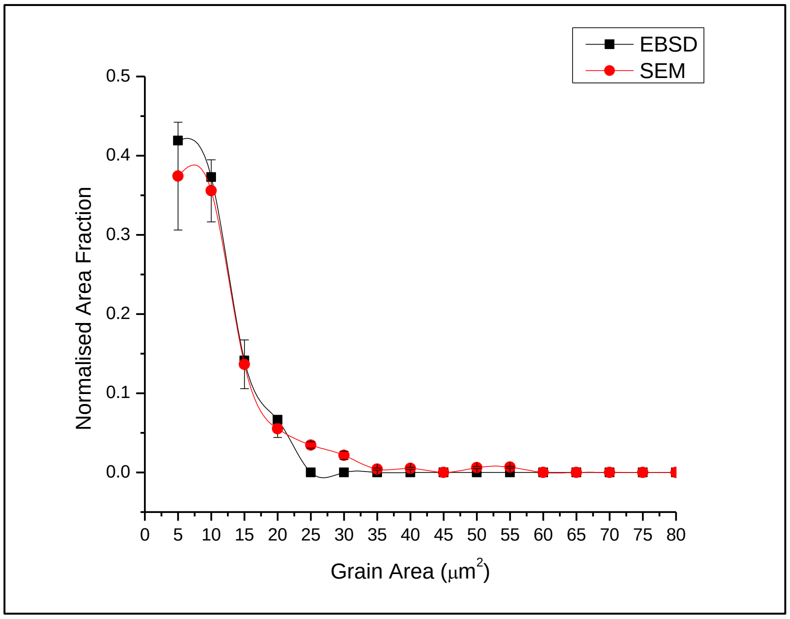

Figure 46 Comparison of histograms for alloy 5A (1.5Si2Mn) at approximately 20% RX stage

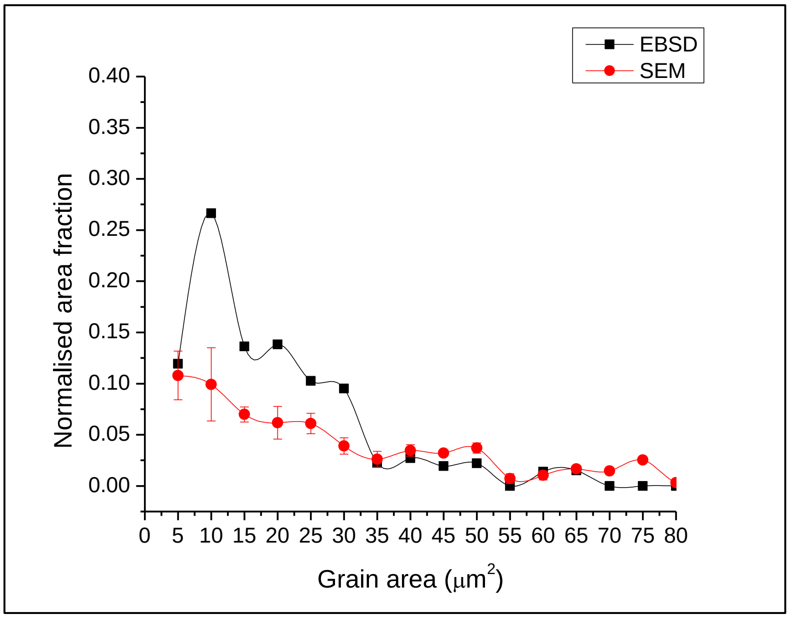

Figure 47 Comparison of histograms for alloy 5A (1.5Si2Mn) at approximately 50% RX stage

E. GRAIN SIZE DISTRIBUTIONS

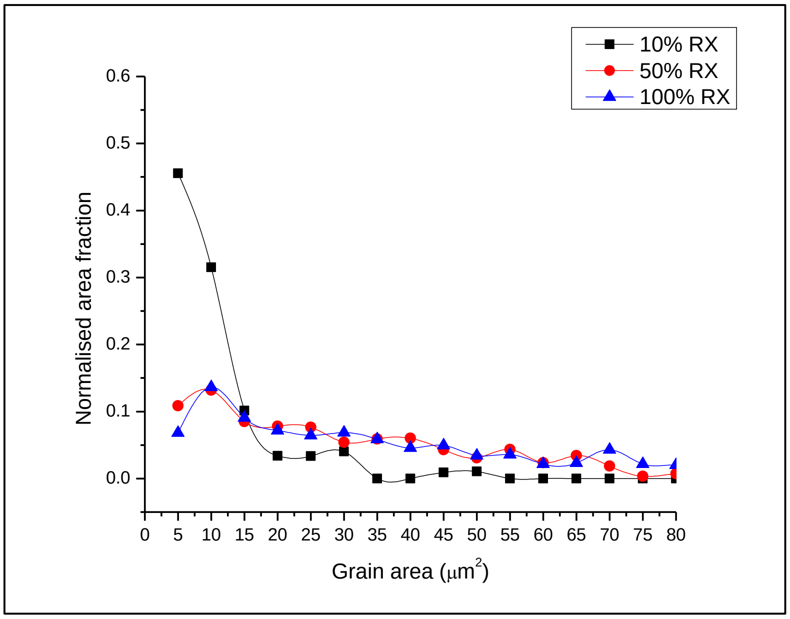

Figure 48 Grain size distributions of alloy 2A (0Si2Mn) annealed at 1 K/s

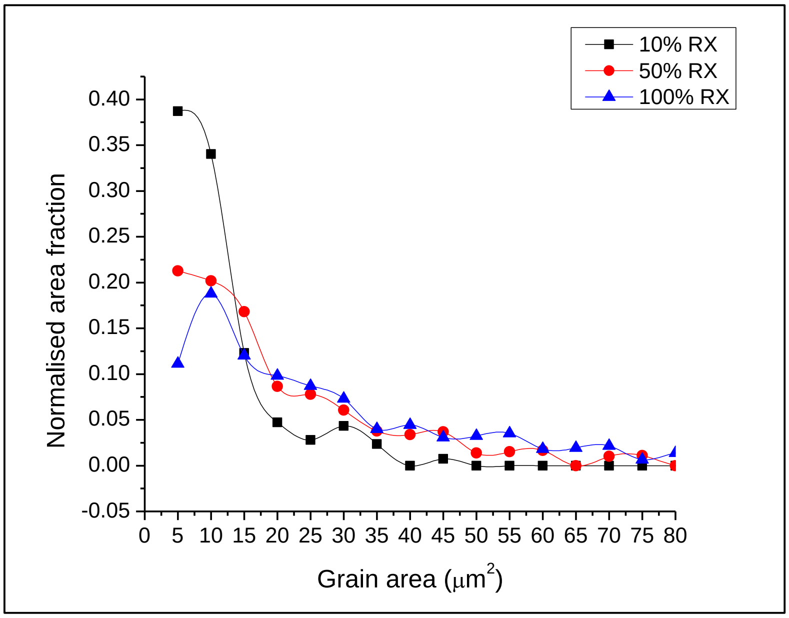

Figure 49 Grain size distribution for alloy 2B (0.4Si2Mn) annealed at 1 K/s.

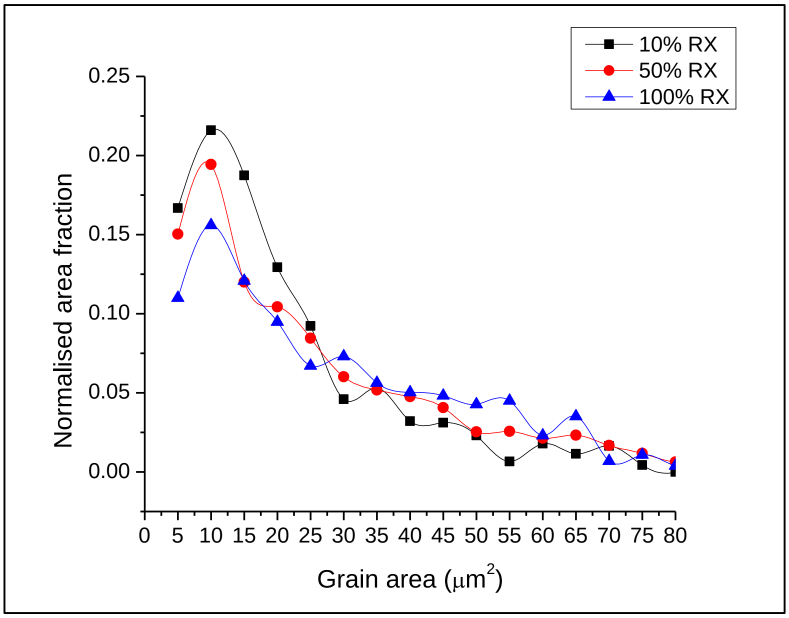

Figure 50 Grain size distribution of alloy 4A (1Si2Mn) annealed at 1 K/s

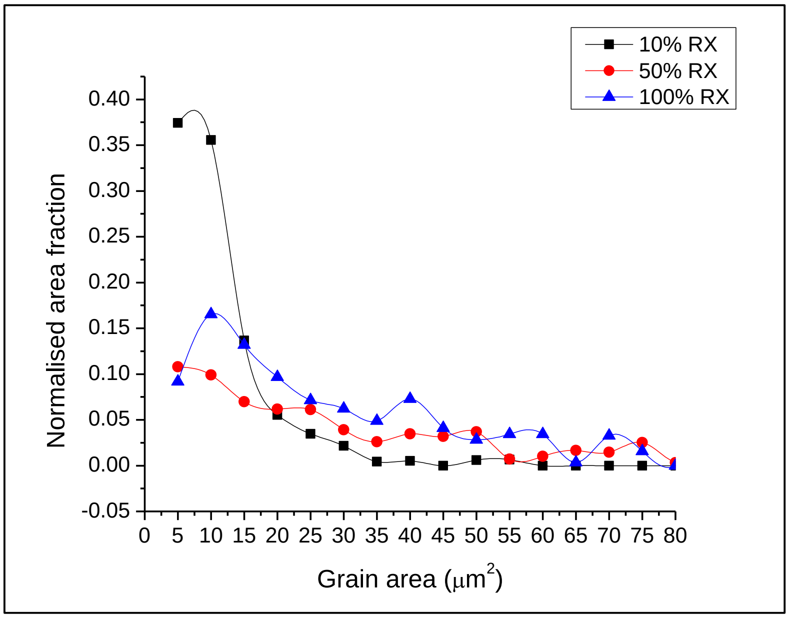

Figure 51 Grain size distribution of alloy 5A (1.5Si2Mn) annealed at 1 K/s

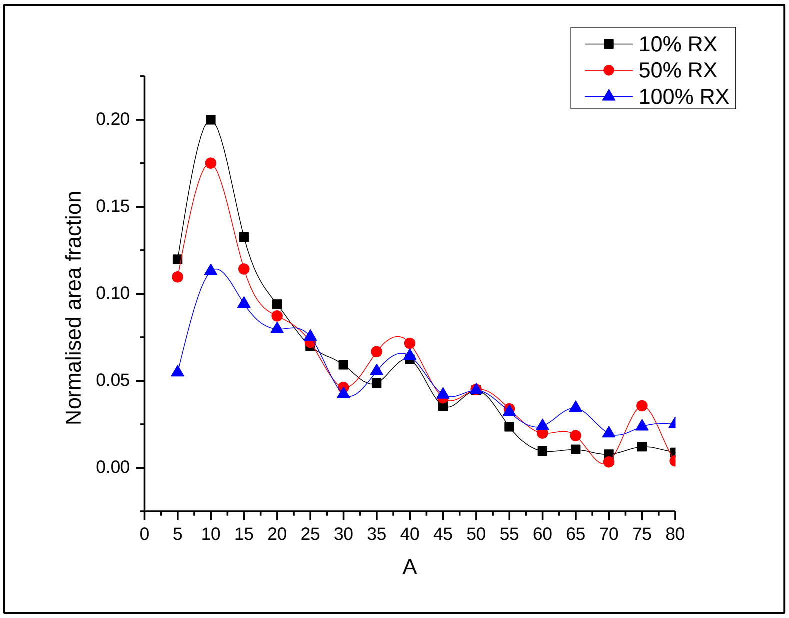

Figure 52 Grain size distributions of alloy 6A (0.4Si0Mn) annealed at 1 K/s

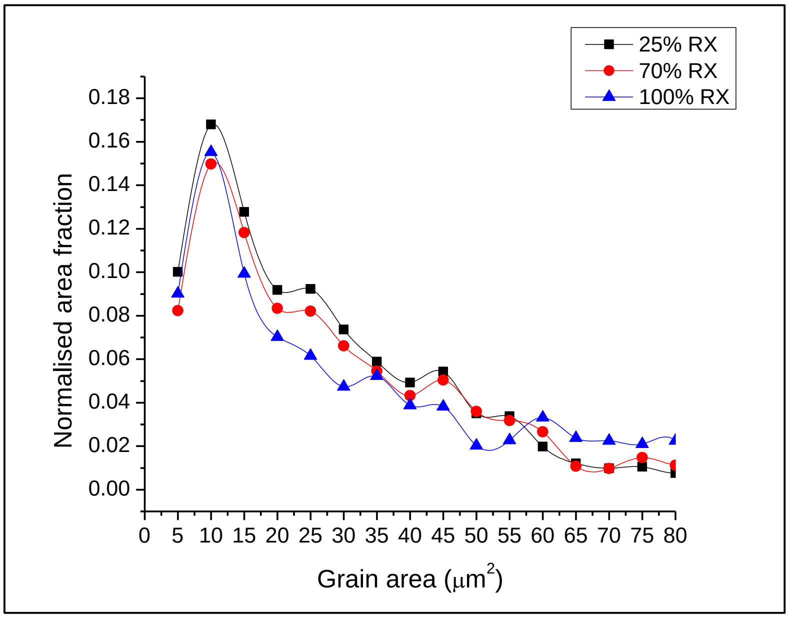

Figure 53 Grain size distribution of alloy 7A (1Si2Mn) annealed at 1 K/s

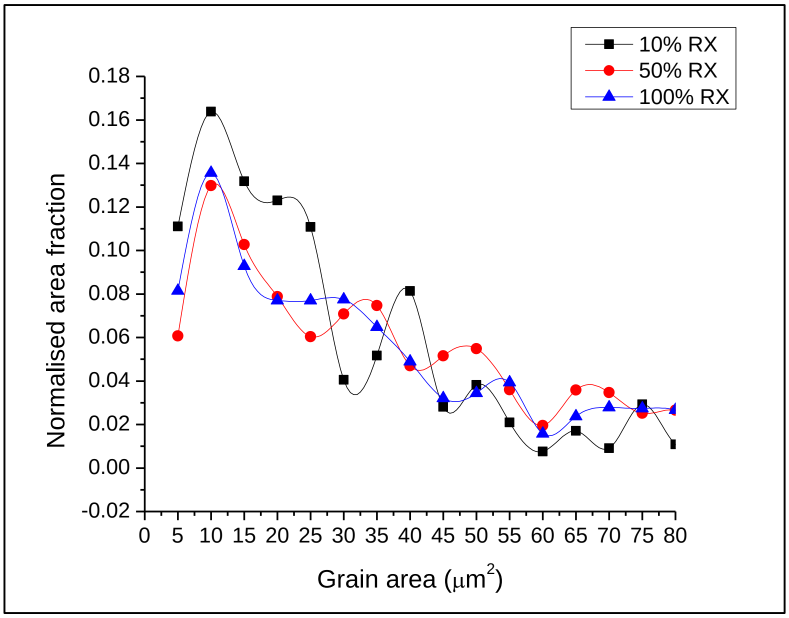

Figure 54 Grain size distribution of alloy 7B (1.5Si0Mn) annealed at 1 K/s

F. MODEL FITTING FOR OTHER CASES

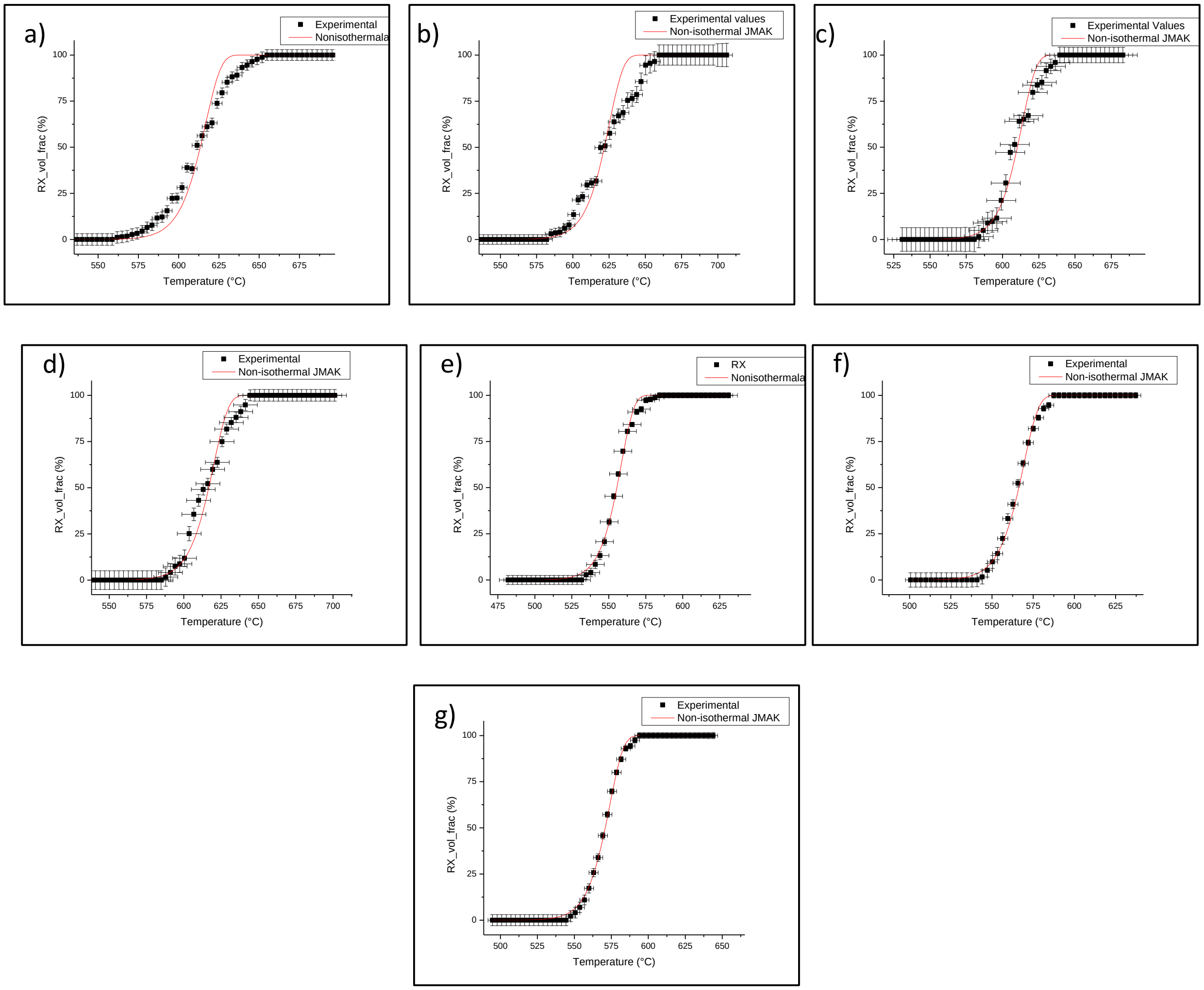

Figure 55 Curve fits for a) Alloy 2A (0.4Si2Mn) b) Alloy 2B (0.4Si2Mn) c) Alloy 4A (1Si2Mn) d) Alloy 5A (1.5Si2Mn) e) Alloy 6A (0.4Si0Mn) f) Alloy 7A (1Si0Mn) g) Alloy 7B (1.5Si0Mn) for the case of 0.1 K/s.

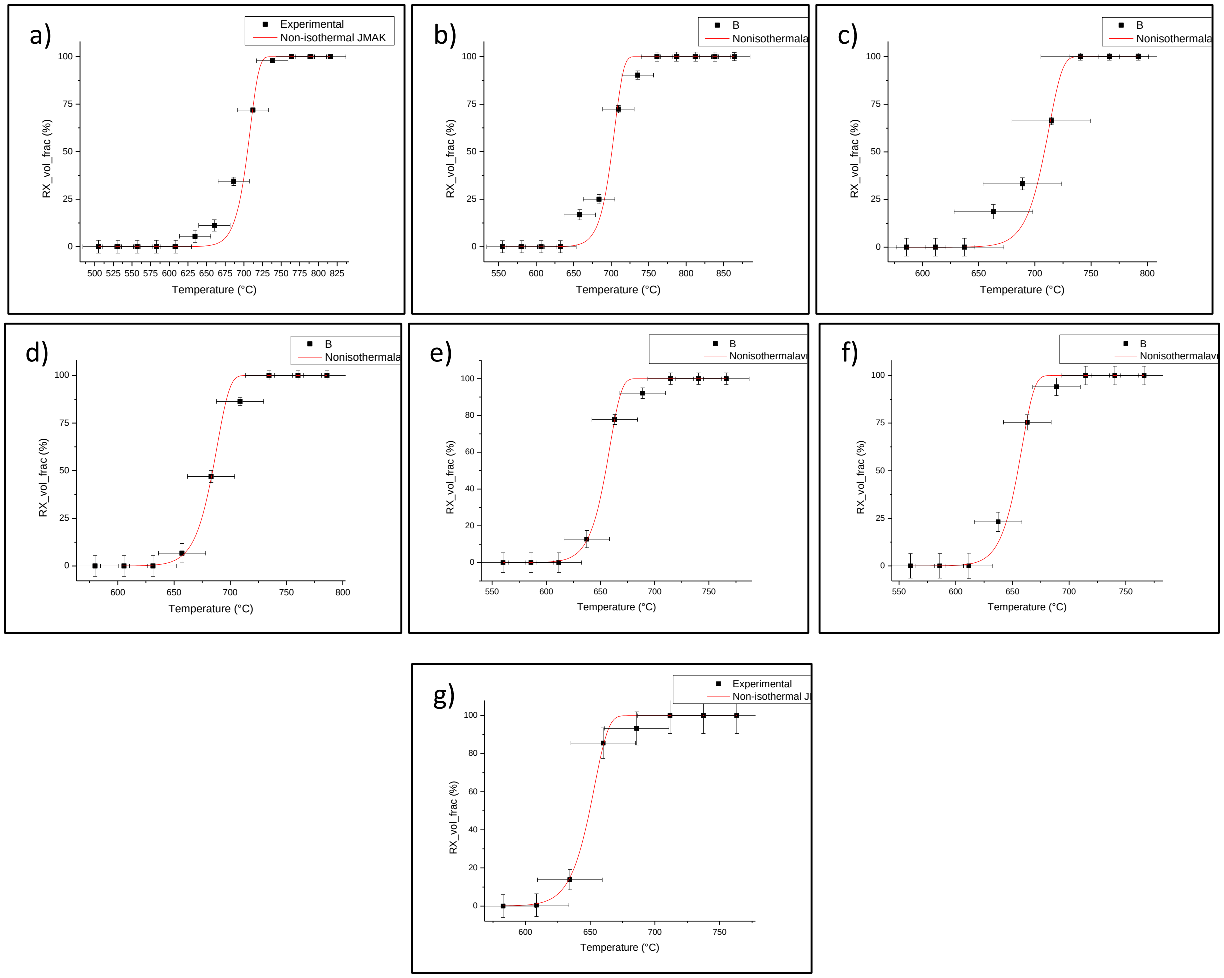

Figure 56 Curve fits for a) Alloy 2A (0.4Si2Mn) b) Alloy 2B (0.4Si2Mn) c) Alloy 4A (1Si2Mn) d) Alloy 5A (1.5Si2Mn) e) Alloy 6A (0.4Si0Mn) f) Alloy 7A (1Si0Mn) g) Alloy 7B (1.5Si0Mn) for the case of 5 K/s.

G. MICROSTRUCTURES

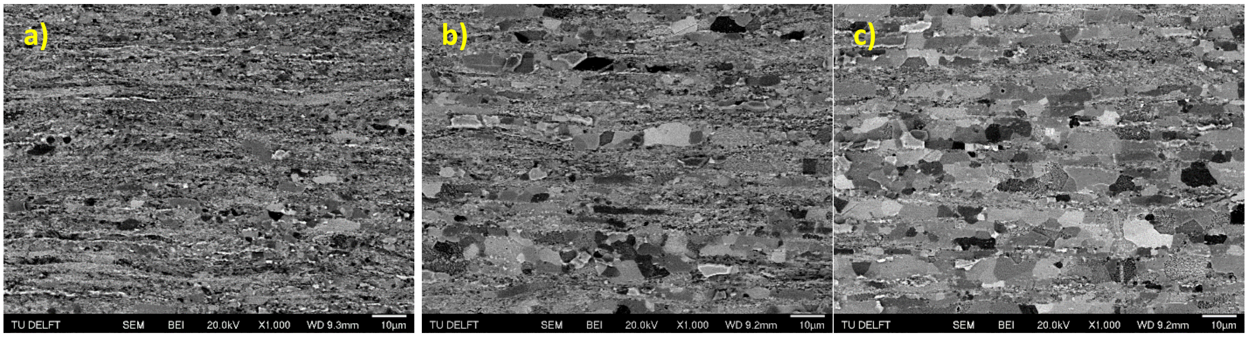

Figure 57 The microstructure evolution of Alloy 2B [0.4Si2Mn] a)10% RX b) 50%RX c) 100% RX

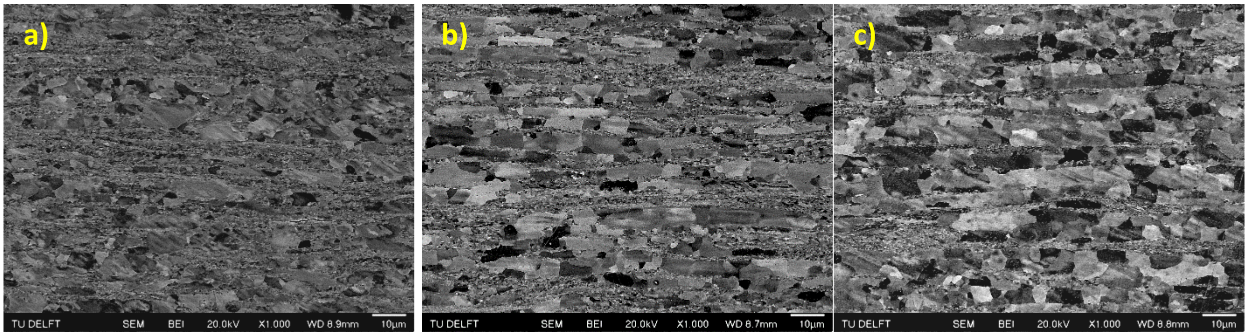

Figure 58 The microstructure evolution of Alloy 4A [1Si2Mn] a)36% RX b) 60%RX c) 100% RX

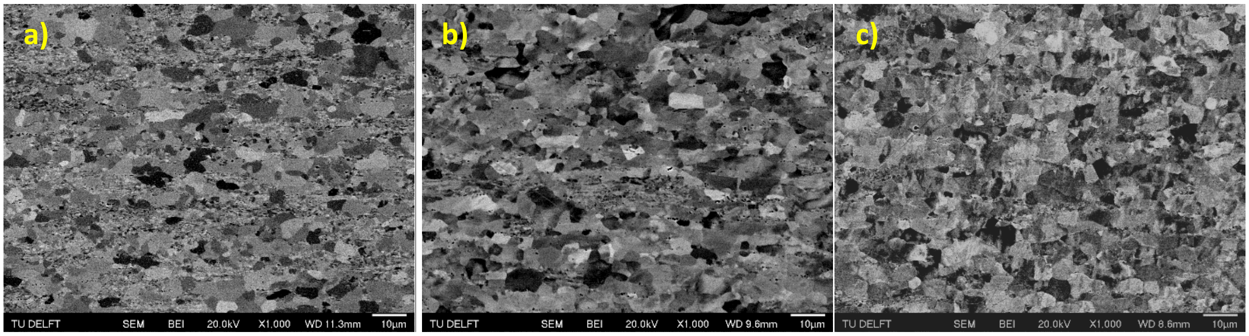

Figure 59 The microstructure evolution of Alloy 6A [0.4Si0Mn] a)20% RX b) 60%RX c) 100% RX

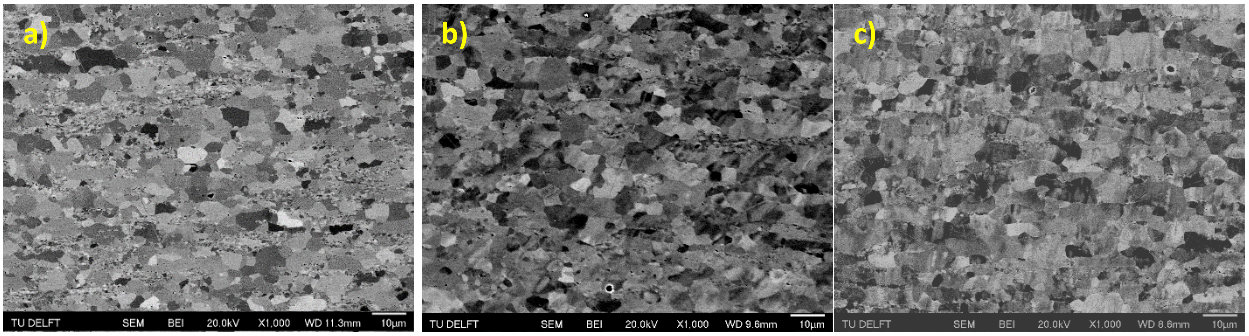

Figure 60 The microstructure evolution of Alloy 7A [1Si0Mn] a)25% RX b) 50%RX c) 100% R

BIBLIOGRAPHY

[1] W. Bleck, “Cold-Rolled, High-Strength Sheet Steels for Auto Applications,” *J. Miner. Met. Mater. Soc.*, no. July, pp. 26–30, 1996.

[2] N. Fonstein, *Advanced High Strength Sheet Steels*. 2015.

[3] A. Chbihi, D. Barbier, L. Germain, A. Hazotte, and M. Gouné, “Interactions between ferrite recrystallization and austenite formation in high-strength steels,” *J. Mater. Sci.*, vol. 49, no. 10, pp. 3608–3621, 2014.

[4] J. Huang, W. J. Poole, and M. Militzer, “Austenite formation during intercritical annealing,” *Metall. Mater. Trans. A*, vol. 35, no. 11, pp. 3363–3375, 2004.

[5] R. R. Mohanty, O. A. Girina, and N. M. Fonstein, “Effect of heating rate on the austenite formation in low-carbon high-strength steels annealed in the intercritical region,” *Metall. Mater. Trans. A Phys. Metall. Mater. Sci.*, vol. 42, no. 12, pp. 3680–3690, 2011.

[6] P. Li, J. Li, Q. Meng, W. Hu, and D. Xu, “Effect of heating rate on ferrite recrystallization and austenite formation of cold-roll dual phase steel,” *J. Alloys Compd.*, vol. 578, pp. 320–327, 2013.

[7] G. E. Dieter, *Mechanical Metallurgy*. 1990.

[8] A. T. Davenport, “Formable HSLA and Dual Phase Steels,” *Metall. Soc. AIME*, 1979.

[9] R. A. Kot, “Structure and properties of dual-phase steels,” *TMS/AIME*, 1979.

[10] T. Ogawa, “Ferrite recrystallization and austenite formation at the early stage of annealing in cold-rolled low-carbon steels,” *Int. J. Mech. Mater. Eng.*, 2015.

[11] G. Liu, J. Li, S. Zhang, J. Wang, and Q. Meng, “Dilatometric study on the recrystallization and austenization behavior of cold-rolled steel with different heating rates,” *J. Alloys Compd.*, vol. 666, pp. 309–316, 2016.

[12] P. R. Rios, Jr, Fulvio Siciliano, Hugo Ricardo Zschommler Sandim, Ronald Lesley Plaut, and Angelo Fernando Padilha, “Nucleation and Growth During Recrystallization,” *Mater. Res.*, vol. 8, no. 3, pp. 225–238, 2005.

[13] F. J. Humphreys, “Nucleation in Recrystallization,” *Mater. Sci. Forum*, vol. 467–470, pp. 107–116, 2004.

[14] F. . Humphreys and M. Hatherly, *Recrystallization and related annealing phenomena*, Second Edi., vol. 1. 2004.

[15] D. Z. Yang, E. L. Brown, D. K. Matlock, and G. Krauss, “Ferrite recrystallization and austenite formation in cold-rolled intercritically annealed steel,” *Metall. Trans. A*, vol. 16, no. 8, pp. 1385–1392, 1985.

[16] C. Zheng and D. Raabe, “Interaction between recrystallization and phase transformation during intercritical annealing in a cold-rolled dual-phase steel: A cellular automaton model,” *Acta Mater.*, vol. 61, no. 14, pp. 5504–5517, 2013.

[17] D. Porter, K. Easterling, and M. Sherif, *Phase Transformations in Metals and Alloys*, 3rd Editio. CRC Press.

[18] G. Gottstein and L. Shvindlerman, *Grain Boundary Migration in Metals*, Second Edi. CRC Press, 2010.

[19] M. Avrami, “Kinetics of Phase Change. I General Theory,” *J. Chem. Phys.*, vol. 7, p. 1103, 1939.

[20] M. Avrami, “Kinetics of Phase Change. II Transformation- Time Relations for Random Distribution of Nuclei,” *J. Chem. Phys.*, vol. 8, p. 212, 1940.

[21] M. Avrami, “Granulation, Phase Change and Microstructure Kinetics of Phase Change. III,” *J. Chem. Physics1*, vol. 9, p. 177, 1941.

[22] W. A. Johnson and R. F. Mehl, “Reaction kinetics in processes of nucleation and growth,” *Trans. Am. Inst. Min., Met. Pet. Eng.*, 1939.

[23] A. N. Kolmogorov, “On the statistical theory of the crystallization of metals,” *Bull. Acad. Sci. USSR, Math. Ser 1*, pp. 355–359, 1937.

[24] F. . Humphreys and M. Hatherly, *Recrystallization and Related Annealing Phenomenon*, Second Edi. Elsevier B.V, 2004.

[25] J. W. Cahn, “The kinetics of grain boundary nucleated reactions,” *Acta Metall.*, vol. 4, no. 5, pp. 449–459, 1956.

[26] T. Furu, K. Marthinsen, and E. Nes, “Modelling recrystallisation,” *Mater. Sci. Technol.*, vol. 6, no. 11, 1990.

[27] R. A. Vandermeer and B. B. Rath, “Modeling recystallization kinetics in a deformed iron single crystal,” *Metall. Trans. A*, vol. 20, no. 3, pp. 391–401, 1989.

[28] R. D. Doherty, K. Kashyap, and S. Panchanadeeswaran, “Direct observation of the development of recrystallization texture in commercial purity aluminum,” *Acta Metall. Mater.*, vol. 41, no. 10, pp. 3029–3053, 1993.

[29] B. Radhakrishnan, G. B. Sarma, and T. Zacharia, “Modeling the kinetics and microstructural evolution during static recrystallization—Monte Carlo simulation of recrystallization,” *Acta Mater.*, vol. 46, no. 12, pp. 4415–4433, 1998.

[30] F. J. Humphreys, “A unified theory of recovery, recrystallization and grain growth, based on the stability and growth of cellular microstructures—II. The effect of second-phase particles,” *Acta Mater.*, vol. 45, no. 12, pp. 5031–5039, 1997.

[31] F. J. Humphreys, “A unified theory of recovery, recrystallization and grain growth, based on the stability and growth of cellular microstructures—I. The basic model,” *Acta Mater.*, vol. 45, no. 10, pp. 4231–4240, 1997.

[32] J. Farjas and P. Roura, “Modification of the Kolmogorov-Johnson-Mehl-Avrami rate equation for non-isothermal experiments and its analytical solution,” *Acta Mater.*, vol. 54, no. 20, pp. 5573–5579, 2006.

[33] H. Guo, G. R. Purdy, M. Enomoto, and H. I. Aaronson, “Kinetic transitions and substititional solute (Mn) fields associated with later stages of ferrite growth in Fe-C-Mn-Si,” *Metall. Mater. Trans. A*, vol. 37, no. 6, pp. 1721–1729, 2006.

[34] N. Peranio, Y. J. Li, F. Roters, and D. Raabe, “Microstructure and texture evolution in dual-phase

steels: Competition between recovery, recrystallization, and phase transformation," *Mater. Sci. Eng. A*, vol. 527, no. 16–17, pp. 4161–4168, 2010.

[35] D. Muljono, M. Ferry, and D. P. Dunne, "Influence of heating rate on anisothermal recrystallization in low and ultra-low carbon steels," *Mater. Sci. Eng. A*, vol. 303, no. 1–2, pp. 90–99, 2001.

[36] S. S. Sahay and K. B. Joshi, "Heating Rate Effects During Non-Isothermal Annealing of AlK Steel," *J. Mater. Eng. Perform.*, vol. 12, no. April, pp. 157–164, 2003.

[37] J. Drumond, O. Girina, J. F. da Silva Filho, N. Fonstein, and C. A. S. de Oliveira, "Effect of Silicon Content on the Microstructure and Mechanical Properties of Dual-Phase Steels," *Metallogr. Microstruct. Anal.*, vol. 1, no. 5, pp. 217–223, 2012.

[38] T. F. Majka, D. K. Matlock, and G. Krauss, "Development of microstructural banding in low-alloy steel with simulated Mn segregation," *Metall. Mater. Trans. A*, vol. 33, no. June, pp. 1627–1637, 2002.

[39] J. S. Byun, J. H. Shim, and Y. W. Cho, "Influence of Mn on microstructural evolution in Ti-killed C-Mn steel," *Scr. Mater.*, vol. 48, no. 4, pp. 449–454, 2003.

[40] M. Calcagnotto, D. Ponge, and D. Raabe, "On the effect of manganese on grain size stability and hardenability in ultrafine-grained ferrite/martensite dual-phase steels," *Metall. Mater. Trans. A Phys. Metall. Mater. Sci.*, vol. 43, no. 1, pp. 37–46, 2012.

[41] K. Lücke and K. Detert, "A quantitative theory of grain-boundary motion and recrystallization in metals in the presence of impurities," *Acta Metall.*, vol. 5, no. 11, pp. 628–637, 1957.

[42] M. Hillert and B. O. Sundman, "A Treatment of the Solute Drag on Moving Grain Boundaries and Phase Interfaces in Binary Alloys," *Acta Metall.*, vol. 24, no. 1, pp. 731–743, 1976.

[43] Y. Huang and F. J. Humphreys, "The effect of solutes on grain boundary mobility during recrystallization and grain growth in some single-phase aluminium alloys," *Mater. Chem. Phys.*, vol. 132, no. 1, pp. 166–174, 2012.

[44] R. D. Doherty *et al.*, "Current issues in recrystallization: a review," *Mater. Sci. Eng. A*, vol. 238, no. 2, pp. 219–274, 1997.

[45] H. Guo and M. Enomoto, "Effects of substitutional solute accumulation at α/γ boundaries on the growth of ferrite in low carbon steels," *Metall. Mater. Trans. A Phys. Metall. Mater. Sci.*, vol. 38, no. 6, pp. 1152–1161, 2007.

[46] S. Schmidt, "Watching the Growth of Bulk Grains During Recrystallization of Deformed Metals," *Science (80-.).*, vol. 305, no. 5681, pp. 229–232, 2004.

[47] H. Hu and S. R. Goodman, "Effect of manganese on the annealing texture and strain ratio of low-carbon steels," *Metall. Trans.*, vol. 1, no. 11, pp. 3057–3064, 1970.

[48] E. M. Lauridsen, H. F. Poulsen, S. F. Nielsen, and D. Juul Jensen, "Recrystallization kinetics of individual bulk grains in 90% cold-rolled aluminium," *Acta Mater.*, vol. 51, no. 15, pp. 4423–4435, 2003.

[49] G. G. E. Seward, S. Celotto, D. J. Prior, J. Wheeler, and R. C. Pond, "In situ SEM-EBSD observations of the hcp to bcc phase transformation in commercially pure titanium," *Acta Mater.*, vol. 52, no.

4, pp. 821–832, 2004.

[50] V. Chakravarthy, K. Rechendorff, Z. Imre, T. Kasama, and R. Ambat, “In-situ TEM investigation of microstructural evolution in magnetron sputtered Al – Zr and Al – Zr – Si coatings during heat treatment,” *Mater. Des.*, vol. 89, pp. 1071–1078, 2016.

[51] M. B. Dickerson *et al.*, “Applications of 2D detectors in X-ray Analysis,” *Adv. X-ray Anal.*, vol. 45, no. 1, pp. 338–344, 2002.

[52] B. B. He, U. Preckwinkel, and K. L. Smith, “Fundamentals of Two-Dimensional X-ray Diffraction (XRD2),” *Adv. X-ray Anal.*, vol. 43, no. c, pp. 273–280, 1999.

[53] R. A. Young, *The Rietveld Method*. 1993.

[54] H. Inagaki, “Fundamental Aspects of Texture Formation in Low Carbon Steel,” *ISIJ Int.*, vol. 34, no. 4, pp. 313–321, 1994.

[55] B. D. Cullity, *Elements of X-ray Diffraction*. 1956.

[56] D. C. Joy, D. E. Newbury, and D. L. Davidson, “Electron channeling patterns in the scanning electron microscope,” *J. Appl. Phys.*, vol. 53, no. 8, 1982.

[57] K. Davut and S. Zaefferer, “Statistical reliability of phase fraction determination based on electron backscatter diffraction (EBSD) investigations on the example of an Al-trip steel,” *Metall. Mater. Trans. A Phys. Metall. Mater. Sci.*, vol. 41, no. 9, pp. 2187–2196, 2010.

[58] J. Vázquez, C. Wagner, P. Villares, and R. Jiménez-Garay, “A theoretical method for determining the crystallized fraction and kinetic parameters by DSC, using non-isothermal techniques,” *Acta Mater.*, vol. 44, no. 12, pp. 4807–4813, 1996.

[59] E. Woldt, “The relationship between isothermal and non-isothermal description of Johnson-Mehl-Avrami-Kolmogorov kinetics,” *J. Phys. Chem. Solids*, vol. 53, no. 4, pp. 521–527, 1992.